Investigations of RC-Loaded Bow-tie Antennas for Impulse Ground Penetrating Radar Applications

A thesis presented

to the Faculty of Graduate Studies

By

Hong Su

In Partial Fulfillment

of the Requirement for the Degree of

Master of Science in Electrical Engineering

University of Manitoba

Winnipeg, Manitoba, Canada

August 2006

Abstract

This thesis reports on the investigations of resistive-capacitive (RC) loaded bow-tie antennas with special emphasis on impulse ground penetrating radar applications. Impulse radiation for ground penetrating radar is a challenging research topic because of the unique problem arising from impulse radiation: late-time ringing, which usually masks the important echo signals from the targets. While resistive loading is a common solution for eliminating late-time ringing, use of resistive loading typically sacrifices the radiation efficiency. In this thesis, a resistive-capacitive loading technique is investigated for a circular bow-tie antenna in the attempt to reduce/suppress the late-time ringing as well as to maintain a relatively high radiation efficiency. To implement the system, a microstrip differentiator, which converts a monopulse into a Gaussian-like monocycle to be used as input impulse, is presented. Further, specially designed coplanar waveguide/coplanar strip (CPW/CPS) baluns embedded with Chebyshev transformers of characteristic impedance up to 120Ω have been constructed and tested. To evaluate the system, instead of using the conventional peak voltage value of the radiated waveform, average radiated energy, average ringing energy, relative radiation efficiency and relative ringing efficiency are utilized and these metrics are easily established using low-cost low-sensitivity probes. Measurement results show that the RC-loading scheme is functioning as expected and the impulse system as a whole is capable of reducing the late-time ringing energy to 50% while maintaining average radiation energy as 83% when compared with capacitive loading cases.

Acknowledgements

The author would like to thank his research advisor Dr. Joe LoVetri for his encouragement, guidance, support and patience during the author's graduate study. Without his suggestions and continuous support, this research would not have been possible.

Thanks to Dr. Greg Bridges for lending the impulse generator in the research and his suggestions. Many thanks to Ian Jeffrey for his help in manuscript formatting and his time for reviewing the thesis. Thanks go to Colin Gilmore for reviewing the thesis and his suggestions. Thanks also go to Michael Phelan and other members of GPR research group at the University of Manitoba for their help.

Table of Contents

List of Figures

List of Tables

Chapter 1 Introduction and Motivation

1.1 Introduction

1.1.1 GPR Resolution

Ground Penetrating Radar (GPR) is one of the most promising and widely used techniques for close-range detection and identification for buried targets [1][2]. GPR functions by sending electromagnetic waves into the ground and by sampling the back-scattered electromagnetic echoes which are affected by the permittivity ε, permeability μ and conductivity σ of the material beneath the ground. By utilizing appropriate signal processing techniques, we can image the electrical properties of sub-surface under test [2][3]. Therefore, GPR has the ability to detect buried objects, including both metallic and non-metallic materials. In recent years, GPR has increasingly been applied to the problems of locating pipes and cables, ice mapping, geographical surveying and landmine detection. Fig. 1.1 shows a block diagram of a GPR system.

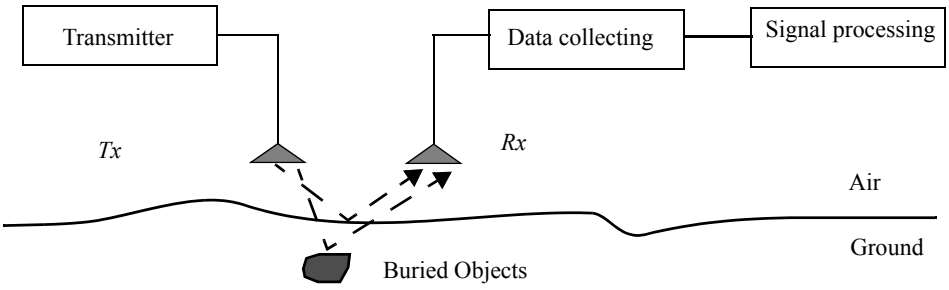

Figure 1.1 GPR block diagram

One important consideration for developing a GPR system is the range resolution. The range resolution of a radar system is defined as "the ability to distinguish between two targets solely by the measurement of their ranges (distance from the radar); usually expressed in terms of the minimum distance by which two targets of equal strength at the same azimuth and elevation angles must be spaced to be separately distinguishable" [4]. The range resolution ΔR, *i.e.*, the depth resolution for the GPR case, is related to the bandwidth B of the system and the propagation velocity v in the media. The relationship is given as [5]

$$\Delta R = \frac{v}{2B}. \tag{1.1}$$

From the above definition, for a GPR with bandwidth of 1 GHz, the depth resolution is 10.6 *cm* for dry sand ($\varepsilon_r = 2$) and 3.4 *cm* for very wet soil ($\varepsilon_r = 20$). It seems that one can just simply increase the bandwidth B of the GPR system from 1 GHz to 2 GHz to double the depth resolution. Unfortunately, this is not practically feasible for real cases. When expanding the bandwidth, the propagation attenuation in the soil for the high frequency components of the wave will increase dramatically, corresponding to a sharp decreases of the penetrating depth. The result: very little back-scattered signal for high frequency waves is collected by the receiving antenna. Therefore, by increasing the bandwidth, one cannot guarantee sufficient interrogation energy.

Since low frequency electromagnetic waves can penetrate into the soil much further than high frequency waves, a GPR system with good resolution and penetrating ability should have a wide bandwidth starting from a frequency as low as possible. Ideally, the best candidate would be a

time-domain unit impulse, $\delta(t)$, defined as

$$\delta(t) = 0 \text{ for } t \neq 0 \text{ and } \int_{-\infty}^{\infty} \delta(t)dt = 1. \tag{1.2}$$

The Fourier Transform of such a pulse is

$$\Im(\delta(t)) = 1, \tag{1.3}$$

which indicates constant energy over an infinite bandwidth. Therefore, a unit pulse GPR will theoretically have an infinitely small depth resolution. Thus, the practical goal is to transmit the shortest pulse possible to gain satisfactory resolution and penetration depth.

1.1.2 Frequency- and Time-Domain GPR

Basically, GPR systems can be classified into two categories: frequency-domain GPR and time-domain GPR. One can process the collected data in either domain by forward/inverse Fourier Transform accordingly.

The stepped-frequency continuous-wave (SFCW) GPR is a good example of using GPR directly in the frequency-domain. Such a system uses a frequency synthesizer to scan through a frequency range equally spaced by a frequency interval Δf. At each frequency step, a continuous wave is radiated into the ground through the *Tx* antenna and the reflected signal is collected by the *Rx* antenna. The received signal contains the combination of reflections from the air-ground interface

and any buried objects. Details of SFCW GPR research at the University of Manitoba can be found in [3][6][7].

Time-domain GPR functions by sending a transient pulse into the ground and then analyzing the received echoes which contain the information of the subsurface electrical properties. As explained previously, duration of the pulse sent by the GPR should be as short as possible for enough bandwidth (good depth resolution). Commonly used pulse shapes are: a Gaussian pulse, a Gaussian monocycle [1] or a Ricker wavelet [2]. It is important that there is no DC component in the transmitted pulse, otherwise, the antenna would be charged at every pulse cycle, causing ringing and the radiation efficiency to degrade. Typically, a Gaussian monocycle, which is the derivative of a Gaussian pulse, is used. The Gaussian monocycle is mathematically expressed as

$$V(t) = -\frac{t}{\tau}\exp(-t^2/\tau^2) \quad , \tag{1.4}$$

where τ is the time decay constant.

An example of a Gaussian monocycle with $\tau = 0.2$ *nanosecond* and its spectrum are plotted in Fig. 1.2(a) to show the symmetry between the negative half cycle and the positive half cycle. Zero DC component can also be observed in its spectrum Fig. 1.2(b).

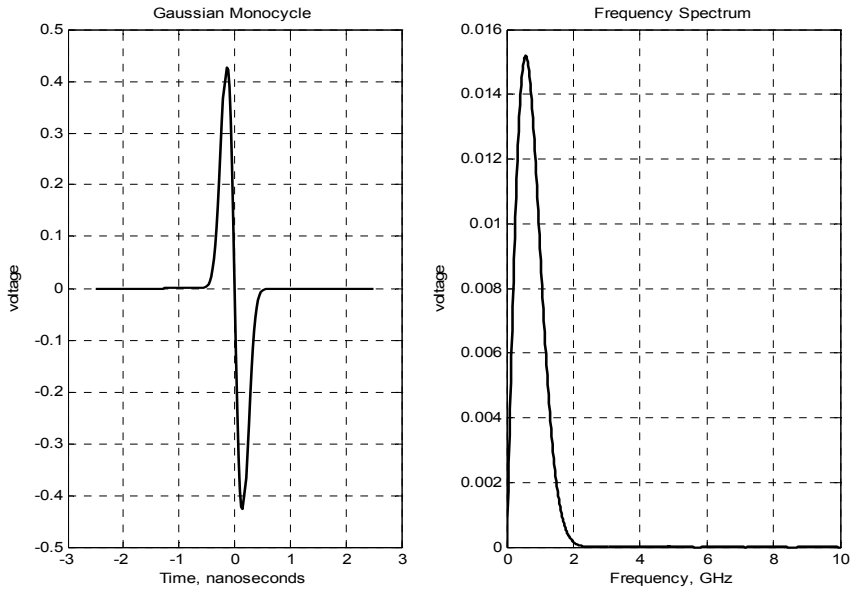

(a) (b)

Figure 1.2 A Gaussian monocycle (a) and its spectrum (b)

For such an impulse GPR, the received signal will be a more complicated, and delayed, wave shape. Generally, the first large echo comes from the air-ground interface and the remaining echoes, which are later in time, are the reflections from subsurface objects. Fig. 1.3 shows the amplitude of an idealized representation for a time-domain Gaussian monocycle incidence on a single object buried in a homogeneous ground. Obviously, the second echo is much more important for GPR applications and it will be discussed in the next section.

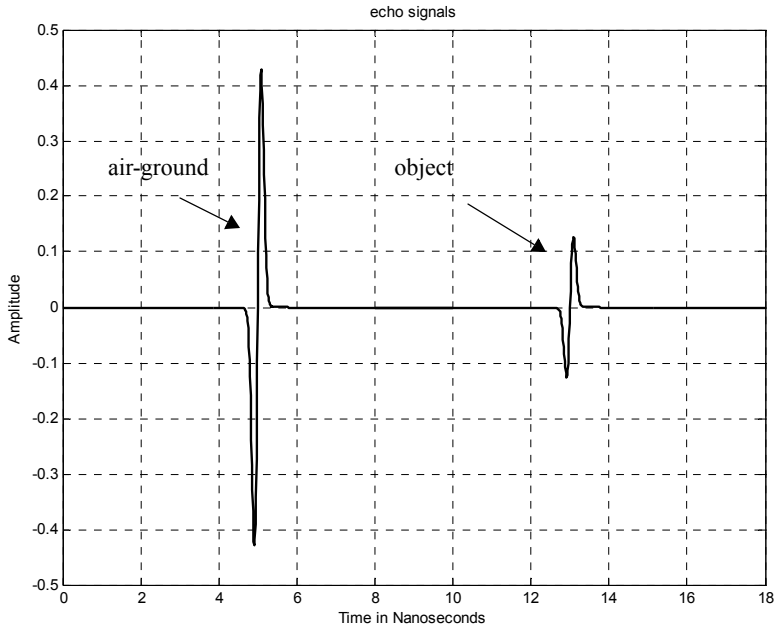

Figure 1.3 Ideal amplitude representation of an impulse GPR

In recent years, it has become practical to accurately generate very narrow pulses with duration times on the order of 100s picoseconds [8]. Such short duration time pulses can easily reach the ultra-wideband (UWB) category for high resolution GPR with a fractional bandwidth much larger than 100%. One advantage of time-domain impulse GPR is that the received signals can be directly processed in the time-domain [1], avoiding Fourier Transform procedure required by SFCW GPR. This is important when postprocessing time is critical for the system. This is one of the factors that has led to intensive studies of impulse GPR [9]-[14].

1.2 Motivation

As discussed in the previous section, one of the main benefits of time-domain GPR systems is that

the impulse can be very short, resulting in good depth resolution for detecting electrically small targets. The problem then becomes how to efficiently transmit electromagnetic energy of such a short impulse into the ground using antennas and how to guarantee that any information in the reflected signal can be distinguished from the ringing effects associated with non-ideal systems. For an impulse GPR, three closely related concerns are: 1) Late-time ringing; 2) Antenna efficiency and input impedance; 3) UWB antenna matching networks.

Late-time ringing is a common nuisance in the response of pulse antenna radiation. It is caused by reflections at the antenna open end, the internal discontinuities, and is related to the antenna's limited bandwidth [53]. Large unexpected late-time ringing can mask the back-scattered echoes and make it very difficult to pick up the necessary signals for target detection. Fig. 1.4(a) shows the S_{11} parameter of a wideband horn antenna used in a SFCW GPR application [3][6][7], Fig. 1.4(b) shows the input pulse signal and Fig. 1.4(c) shows the waveform sensed 10 *cm* away in front of the horn in free space. The late-time ringing is significant and lasts a long time. Due to this strong ringing effect, this horn antenna is inadequate for impulse radiation even though it has very good S_{11} characteristics over a wide bandwidth.

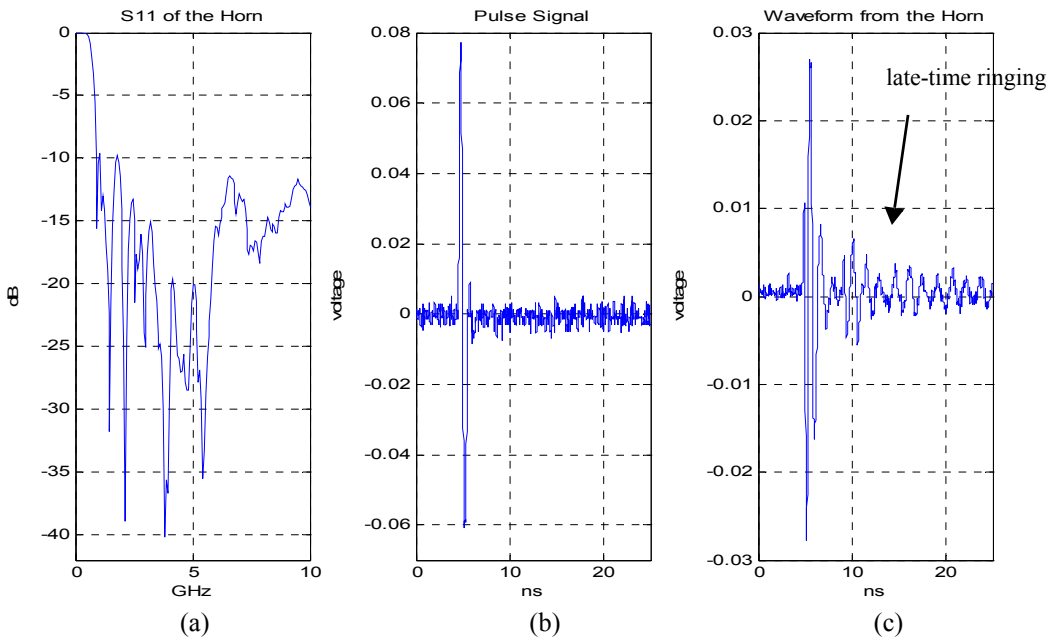

Figure 1.4 S_{11} of a horn antenna (a), the input pulse signal (b) and the late-time ringing (c)

One method used to solve the late-time ringing problem is to apply resistive loading techniques [16]. By adding resistive loading along, or at the end, of the antennas, the antenna working bandwidth is expanded and the reflections are attenuated. The drawback of this traditional resistive loading is low radiation efficiency. How to achieve a low level of late-time ringing and a relatively high radiation efficiency is a current topic for impulse GPR applications [15]-[21][28].

Our research group is in the early stages of time-domain GPR investigations at the University of Manitoba, and the purpose of this thesis is to design wideband antennas for very short impulse radiation with low ringing by using RC-loading, determine an effective matching scheme and to investigate/solve some inherent difficulties for impulse GPR at a laboratory level.

1.3 Thesis Outline

The main focus of this thesis is to come up with a feasible radiator that suppresses late-time ringing. As will be shown, to make such a system usable, a differentiator and a balun were designed and fabricated. These two components are discussed before the antenna design is introduced so that a clear picture of the entire system can be presented. Since numerical simulations and measurements of the system components were made, these results are shown and discussed at the end of the corresponding chapters. The outline of the thesis is as follows:

Chapter 2 gives an overview of current research in impulse GPR. Some reported impedance loading techniques are reviewed and the resistive-capacitive loading method adopted in the thesis is briefly introduced.

In Chapter 3, a differentiator is designed to take the derivatives of the Gaussian-like monopulse and transform it into a Gaussian-like monocycle for feeding the antennas. Simulations and measurement results for the differentiator are included.

Chapter 4 discusses a coplanar waveguide/coplanar strip (CPW/CPS) balun with a Chebyshev transformer embedded in the design. Three baluns were designed due to the difficulties of predicting the antenna input impedance. The baluns' performances were tested and the results are reported.

Chapter 5 is the main part of the thesis where the details for designing and implementing a resis-

tive-capacitive loading (RC-loading) technique for a circular-end bow-tie antenna are discussed. Frequency-domain simulations using HFSS and measurement results for different cases are presented.

In Chapter 6, the experimental system and testing procedure are described. Radiated waveform measurements taken in time-domain are plotted or tabulated by introducing metrics used for evaluating the late-time ringing energy and radiation efficiency. Comparisons are made based on experimental results.

Finally, Chapter 7 concludes, summarizes and discusses the developed impulse system. Problems arising from the thesis are discussed, and suggestions are made for future research directions.

Chapter 2 Impulse GPR Techniques Review

The purpose of this chapter is to give an overview of the basic impulse GPR principles. Maxwell's equations are reviewed as a theoretical background for GPR physics. Difficulties in developing impulse GPR and impedance loading techniques for minimizing late-time ringing are described.

2.1 Maxwell's Equations

Maxwell's equations are the mathematical description of electromagnetic waves. In vector notation, the wave propagation in a conductive dielectric can be described by Maxwell's equations in their differential representation as

$$\nabla\times\boldsymbol{E}(\boldsymbol{r},t) = -\frac{\partial}{\partial t}\boldsymbol{B}(\boldsymbol{r},t), \tag{2.1}$$

$$\nabla\times\boldsymbol{H}(\boldsymbol{r},t) = \frac{\partial}{\partial t}\boldsymbol{D}(\boldsymbol{r},t)+\boldsymbol{J}(\boldsymbol{r},t), \tag{2.2}$$

$$\nabla\cdot\boldsymbol{B}(\boldsymbol{r},t) = 0, \tag{2.3}$$

$$\nabla\cdot\boldsymbol{D}(\boldsymbol{r},t) = \rho(\boldsymbol{r},t), \tag{2.4}$$

and the conservation law for charge as

$$\nabla \cdot \boldsymbol{J}(\boldsymbol{r}, t) = -\frac{\partial}{\partial t}\rho(\boldsymbol{r}, t), \tag{2.5}$$

where **E** is electrical field intensity [*V/m*], **H** magnetic field intensity [*A/m*], **D** electrical flux density [C/m^2], **B** magnetic flux density [Wb/m^2], **J** electrical current density [A/m^2] and ρ charge density [C/m^3].

In linear, source free media, these parameters are related by the constitutive relationships:

$$\boldsymbol{D} = \varepsilon \boldsymbol{E}, \tag{2.6}$$

$$\boldsymbol{B} = \mu \boldsymbol{H}, \tag{2.7}$$

$$\boldsymbol{J} = \sigma \boldsymbol{E}, \tag{2.8}$$

where ε is electric permittivity [*F/m*], μ magnetic permeability [*H/m*] and σ conductivity [*mho/m*].

For time harmonic fields, assuming time dependence $j\omega t$, equations (2.1) and (2.2) can be written as

$$\nabla \times \boldsymbol{E}(\boldsymbol{r}, \omega) = -j\omega\mu \boldsymbol{H}(\boldsymbol{r}, \omega), \tag{2.9}$$

$$\nabla \times \boldsymbol{H}(\boldsymbol{r}, \omega) = (\sigma + j\omega\varepsilon)\boldsymbol{E}(\boldsymbol{r}, \omega) . \tag{2.10}$$

For a lossy dielectric material like soil, the complex conductivity and the complex permittivity are defined as

$$\sigma = \sigma' - j\sigma'', \tag{2.11}$$

$$\varepsilon = \varepsilon' - j\varepsilon'', \tag{2.12}$$

where the imaginary parts of the above definitions describe the loss of the medium as a function of frequency. In most cases, we are dealing with non-ferrous materials and we assume that the permeability is

$$\mu \approx \mu_0 = 4\pi \times 10^{-7} [H/m]. \tag{2.13}$$

Rewriting the combination $\sigma + j\omega\varepsilon$ in (2.10) gives,

$$\sigma + j\omega\varepsilon = (\sigma' + \omega\varepsilon'') + j\omega(\varepsilon' - \sigma''/\omega) = \sigma_e + j\omega\varepsilon_e, \tag{2.14}$$

where σ_e is defined as the real effective conductivity and ε_e as the real effective permittivity.

It is also convenient to define the complex apparent permittivity ε^* as

$$j\omega\varepsilon^* = \sigma_e + j\omega\varepsilon_e \tag{2.15}$$

and the loss tangent $\tan\delta$ as

$$\tan\delta = \frac{\sigma_e}{\omega\varepsilon_e}. \tag{2.16}$$

Now equation (2.10) can simply be written as

$$\nabla\times\boldsymbol{H}(\boldsymbol{r},\omega) = j\omega\varepsilon^*\boldsymbol{E}(\boldsymbol{r},\omega). \tag{2.17}$$

Substituting (2.17) into (2.9), we see that the electric field in a lossy and source free medium satisfies the wave equation:

$$\nabla^2\boldsymbol{E}(\boldsymbol{r},\omega) + k^2\boldsymbol{E}(\boldsymbol{r},\omega) = 0, \tag{2.18}$$

where k is the wave number

$$k = \omega\sqrt{\varepsilon^*\mu}\ . \tag{2.19}$$

One solution of (2.18) is a harmonic plane wave, propagating in the direction of $\boldsymbol{k} = Re[k]\boldsymbol{a}_k$, where $\boldsymbol{a}_k$ is the unit vector along the propagating direction,

$$\boldsymbol{E}(\boldsymbol{r},\omega) = \boldsymbol{E}_0 e^{-j\boldsymbol{k}\cdot\boldsymbol{r}}. \tag{2.20}$$

For lossy material, k is complex and

$$jk = \alpha + j\beta, \tag{2.21}$$

where α is the attenuation constant and is given by

$$\alpha = \omega\sqrt{\frac{\mu\varepsilon_e}{2}(\sqrt{1+tan^2\delta}-1)} \tag{2.22}$$

and β is the phase constant given by

$$\beta = \omega\sqrt{\frac{\mu\varepsilon_e}{2}(\sqrt{1+tan^2\delta}+1)} \tag{2.23}$$

For time-domain waves, $\boldsymbol{E}$ and $\boldsymbol{E}_0$ are functions of time, and the far field in (2.20) can be written as

$$\boldsymbol{E}(\boldsymbol{r}, t) = Re[\boldsymbol{E}_0(t)e^{-j\boldsymbol{k}\cdot\boldsymbol{r}}e^{j\omega t}] . \tag{2.24}$$

When the wave hits a target located at distance R, for generality and simplification, if we assume the reflected wave is also a plane wave, the reflected wave can be approximated as

$$\boldsymbol{E}_{reflected}(\boldsymbol{r}, t) = Re[\Gamma\boldsymbol{E}_{R0}e^{jkr}e^{j\omega t}] , \tag{2.25}$$

where Γ is the complex reflection coefficient of the target, $\boldsymbol{E}_{R0}$ is the incident field at the target. It can be seen that the reflected wave contains all the information of the medium (*k,* which is a function of ε, μ and δ) and the target characteristics (which decide Γ).

2.2 A Review of Impulse GPR Techniques

Impulse GPR systems need special design considerations for reducing late-time ringing due to the antenna geometry. The most common solution is the resistive or impedance loading of antenna, where the principle is that by carefully deploying a smooth impedance variation along the antenna, small reflections can be obtained when the pulse is traveling through the antennas. Though many antennas seem to fulfill some requirements for impulse radiation such as wide bandwidth and good directivity, it is usually hard to realize an easy impedance loading for antennas because of the complexity of the antenna geometry. Various designs such as the tapered loading method [18][23], different kinds of resistive loading [14][24][25][27], the dielectric horn wedge [28] and resistive-capacitive loading [22] have been suggested.

The first impedance loading method was probably proposed by Wu and King [16]. This well-known method suggests that when the material forming the antenna is resistive, a traveling wave will be transmitted and radiated without reflection. An obvious disadvantage of this design is the signal loss due to the resistive distribution along the antenna and the resulting reduction in radiation efficiency [56]. However, the Wu-King profile has been regarded as a guiding principle for antenna impedance loading.

A Partial Dielectric-loaded TEM (PDTEM) horn antenna was suggested by Turk for GPR use [14]. In his design shown in Fig. 2.1, a partial dielectric material is put in the antenna aperture and a resistive sheet is added at the antenna end. In addition, an absorbing coating is introduced at the antenna input plane to reduce multiple reflections in the antenna. It is reported that a voltage

standing wave ratio (VSWR) less than 2 over a 20:1 frequency band (350 MHz to 7 GHz) was achieved [14]. The drawback of this plan is the low radiation efficiency because of the resistive loads. In addition, the design was made in the frequency-domain and the radiation performances were transformed into the time-domain using an inverse Fourier Transform. And there was no actual pulse applied to this proposal.

.

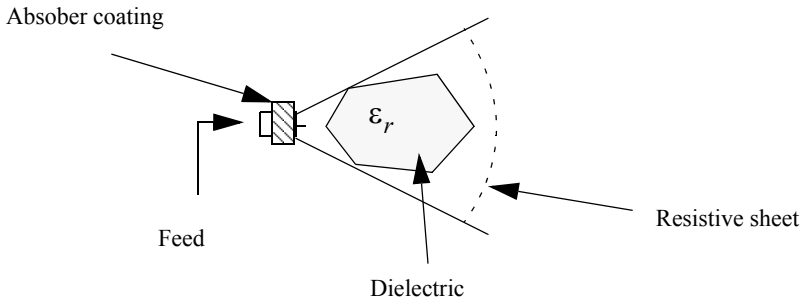

Figure 2.1 PDTEM horn design (side view)

Nishioka *et al.* [25] reported a broadband pulse GPR system for detecting buried metallic pipes. A bow-tie configuration is taken for the *Tx*/*Rx* antennas and lumped resistors are used for antenna loading. Investigations are made for (a) isolated antennas when the resistors are not connected with a ferrite-coated cavity and (b) connected-type antennas when connecting the resistors to the cavity. These two configurations are shown in Fig. 2.2. The problems with this design are the expense of the ferrite coating and the radiation efficiency is low and therefore it cannot be used for non-metallic target cases.

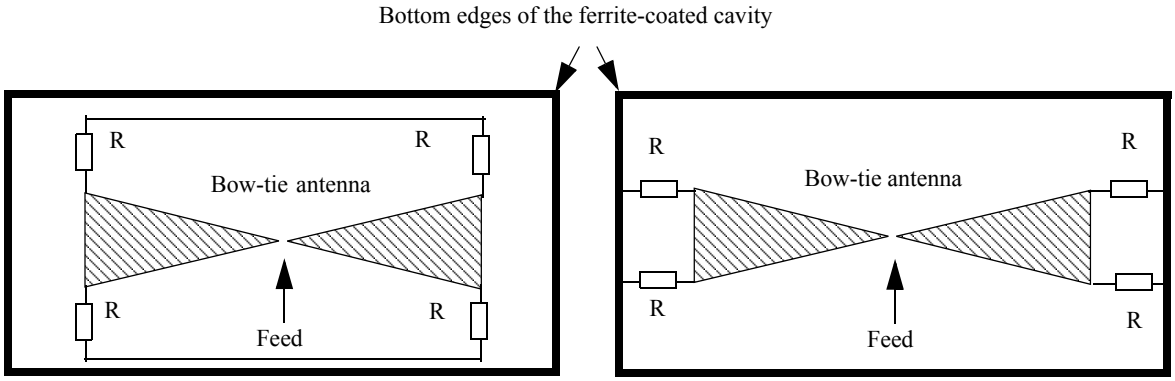

(a) isolated antenna (b) connected-type antenna

Figure 2.2 Lumped resistor loading with cavity for triangular bow-tie GPR

Another bow-tie antenna application is reported by Liu *et al.* in [27]. In this paper, a bow-tie antenna loaded with exponential discrete resistors was studied, as shown in Fig. 2.3. Radiated waveforms and input impedances of a bow-tie antenna were investigated through the finite-difference time-domain (FDTD) method. Though the results showed that the antenna with an exponential discrete resistor-load was able to terminate the reflections at the end of antennas, the radiation efficiency was not considered in this paper and no practical antennas and measurements were made based on its FDTD simulation results.

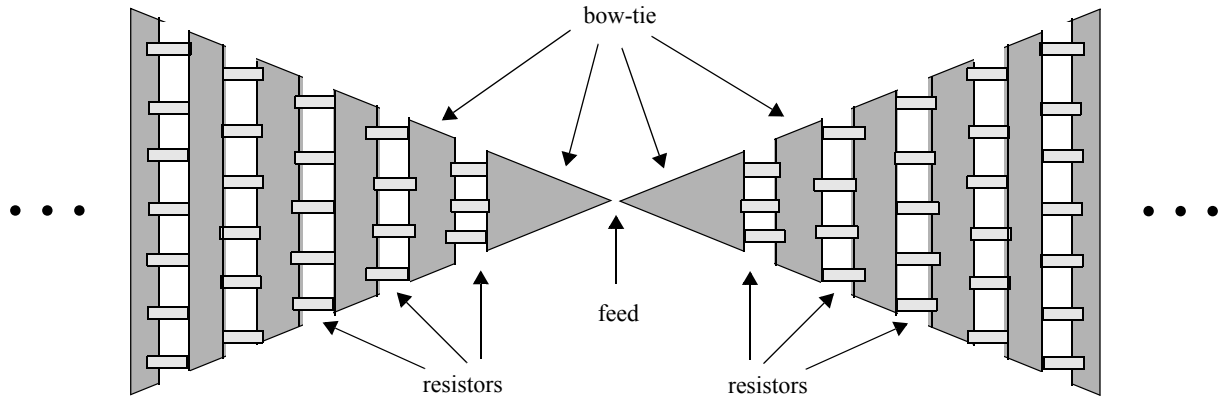

Figure 2.3 Discrete resistor loaded bow-tie

Because resistive loading always degrades the radiation efficiency and capacitive loading alone cannot suppress late-time ringing [22], a promising resistive-capacitive loading technique is proposed by Lestari *et al.* [22][29]. They used a circular bow-tie antenna with slots and strips covered with a microwave absober to realize the RC-loading. Reported results show that this RC-loading is able to reduce the late-time ringing up to -40 dB and the peak voltage value of the transmitted pulse is 54% higher than the same antenna without loading. Because of its promising application to GPR systems, this thesis will consider Lestari *et al.*'s design. Implementation to their design is discussed in Chapter 5.

Chapter 3 The Impulse Signal and Differentiator

This chapter introduces the source section of the system. The impulse generator, the impulse signal and a differentiator, which converts a monopulse into a monocycle for excitation of antennas, are discussed. Measurements showed good agreement with simulation results and the fabricated differentiator can successfully change the monopulse from the impulse generator into a Gaussian-like monocycle.

3.1 The Impulse Signal and Generator

For impulse GPR, it is important to know how much power the impulse generator should have. The larger the impulse signal amplitude, the further the penetrating depth, but with higher power, the system becomes very costly. Thus, the power of the generator should be carefully chosen. It should be considered together with the depth of targets, the attenuation of the soil/sand, the radiation efficiency and the sensitivity of A/D converter for signal processing, *etc*. According to [13], a monocycle with an amplitude of 40 V has been successfully used in an impulse ground penetrating radar system to detect shallow-buried targets. Fortunately, a Picosecond UHF Impulse Generator 1000A which generates a 45 V peak-value impulse with 350 picosecond rise time [8] was available from the Department of Electrical and Computer Engineering at the University of Manitoba and it is very suitable for our initial impulse GPR research. The impulse signal and its spec-

trum are shown in Fig. 3.1.

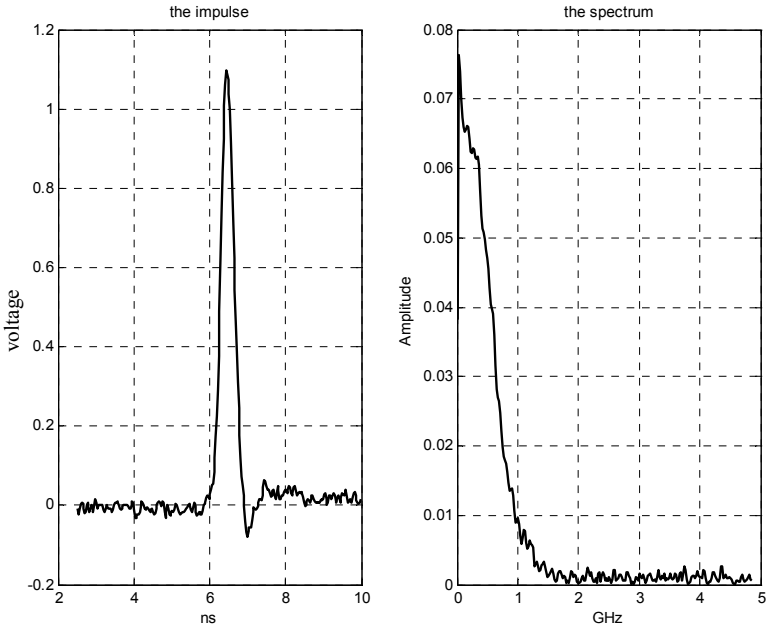

Figure 3.1 The impulse from the generator and its spectrum

As stated in Section 1.1.2 on page 3, the best input signal for antenna excitation would have no DC component. But in Fig. 3.1, we see that there exists some DC component from the Gaussian-like impulse. This signal was directly used for excitating a bow-tie antenna to investigate the late-time ringing effect due to its non-zero DC component, the radiated waveform is shown in Fig. 3.2.

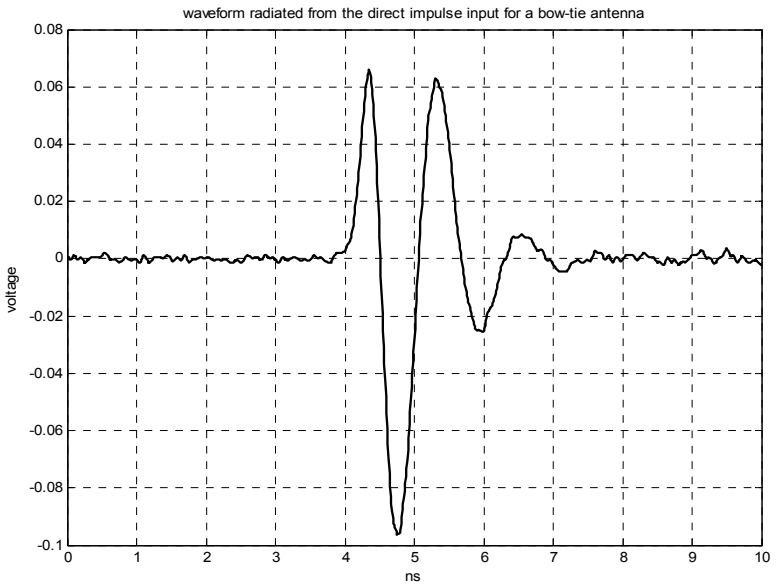

Figure 3.2 Late-time ringing effect for the impulse with non-zero DC component

As can be seen from Fig. 3.1, the duration of the impulse itself is about 1.2 *nanosecond*. Though the bow-tie antenna radiates out the first derivative of the excitation pulse [22], which lasts the same amount of time as the impulse itself, it is observed that the ringing after the derivative signal duration is so strong that this impulse with non-zero DC component cannot be directly used for impulse radiation. To suppress the late-time ringing and eliminate this DC component, a practical method is to convert the monopulse into a monocycle by taking the derivative of the signal. Therefore, a differentiator to transform the monopulse into a Gaussian-like monocycle has been constructed and placed between the impulse generator and the antennas.

3.2 Microstrip Differentiator

Although many methods are available to develop differentiator [45]-[48], most of them are for low frequency applications [49]. However, a low-cost, small size microstrip differentiator is reported with a bandwidth from DC to 6 GHz in [49] and it is quite suitable for our use.

A schematic diagram of this differentiator is shown in Fig. 3.3. The differentiator was made on a Duroid substrate with simple microstrip structure. As shown in Fig. 3.3(a), it consists of a 50Ω transmission line shunted with a two-section shorted line, where β_1, β_2 are the phase constants and l_1, l_2 the physical lengths of the two shunted lines. Details of the theory and derivation can be found in [49] and the physical principle of the differentiator is stated bellow.

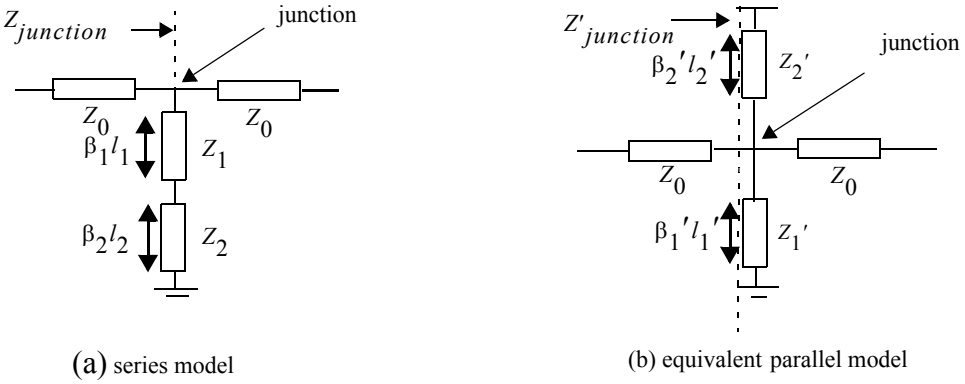

(a) series model (b) equivalent parallel model

Figure 3.3 The transmission line models of the differentiator

When a signal, for example, a monopulse, is transmitted into the differentiator's input port, part of the signal goes through the junction to the output port direction, which is still a monopulse. In the

same time, another part of the signal goes into the shunted transmission line and is reflected back from the ground end. Due to the specially designed electrical length $\beta_1 l_1 + \beta_2 l_2 = \frac{\pi}{2}$ of the shunted line for specific frequency, this reflected signal, which has 180^o phase difference from the first part signal, joins the first pass-through signal at the junction, forming the negative half of a monocycle. The key parameter for this design is the electrical length of each transmission line section so that a monocycle with continuous waveform can be obtained at the output port. Based on this model, an equivalent parallel configuration of two finite transmission lines, which are put symmetrically on both sides of the 50Ω transmission line with via-holes for grounding at the ends, were proposed, as shown in Fig. 3.3(b). Though the reported results look very promising, the only known parameters from [49] are the characteristic impedances of the two-section transmission lines for the model in Fig. 3.3(a), given as $Z_1 = 21.65\Omega$ and $Z_2 = 7.21\Omega$. We need to determine the characteristic impedances of the shunted lines, their lengths, the number of vias, size and positions.

3.3 Design and Simulation

To define the two parallel transmission line impedances Z_1' and Z_2' in Fig. 3.3(b), we write the characteristic impedance at the junction of the series model in Fig. 3.3(a) as

$$Z_{junction} = \frac{Z_0(Z_1 + Z_2)}{Z_0 + Z_1 + Z_2} \ , \tag{3.1}$$

and the characteristic impedance at the junction of the parallel model in Fig. 3.3 (b) as

$$Z'_{junction} = \frac{Z_0 Z_1' Z_2'}{Z_0 Z_1' + Z_0 Z_2' + Z_1' Z_2'} . \tag{3.2}$$

By letting

$$Z'_{junction} = Z_{junction} , \tag{3.3}$$

Z_1' and Z_2' can then be determined. Though there are many choices for Z_1' and Z_2' to satisfy the above relationship (3.3), the equivalent characteristic impedances of the two equivalent finite microstrips were chosen as $Z_1' = 55\Omega$ and $Z_2' = 65\Omega$ for our design.

Based on Z_1' and Z_2' values, the widths of each transmission line were calculated [40] for a Diclad 527 substrate with thickness 1.58 *mm* and relative dielectric constant $\varepsilon_r = 2.5$. As suggested in [49], the lengths of the shunted lines were chosen around quarter wavelength of maximum working frequency of 10 GHz (4.7 *mm* for $\varepsilon_r = 2.5$ substrate) as to be 4.4 *mm* and 4.3 *mm* respectively so that the final propagation delay time of each finite line may not be exactly 25 picoseconds [50] and the maximum working frequency signal will not be fully shorted. HFSS 9.2 software was used to simulate and predict the scattering parameters of the differentiator. By trial and error, nine via-holes were added along the edge to realize the ground termination of the shunted lines. The diameter of the vias was chosen as 1 *mm* and the size of grounding patch was decided as $18mm \times 8mm$. The simulated results for S_{11} and S_{21} are plotted in Fig. 3.4. The

HFSS model is shown in Fig. 3.5(a) and a picture of the fabricated differentiator is shown in Fig. 3.3(b), where the size of the differentiator is $5cm \times 5cm$.

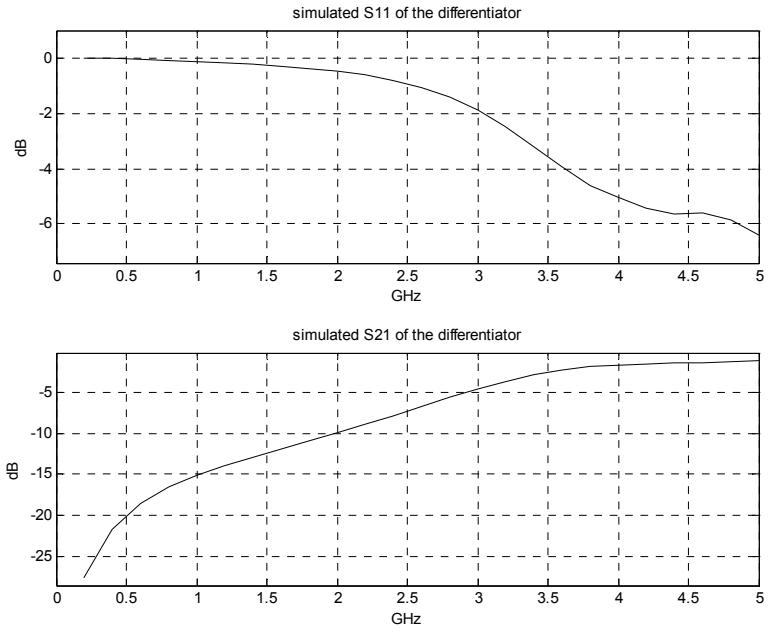

Figure 3.4 *S* parameter simulation results of designed differentiator

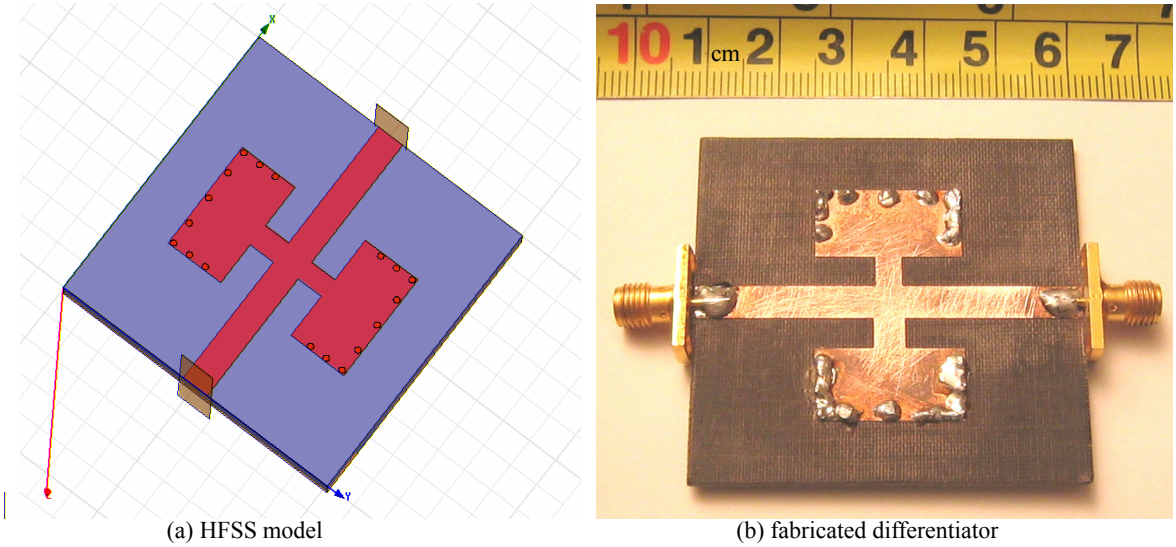

(a) HFSS model (b) fabricated differentiator

Figure 3.5 HFSS model and the differentiator

3.4 Tested Results

An Anritsu 360B network analyzer was used to measure S_{11} and S_{21} parameters of the differentiator and the results are shown in Fig. 3.6. In this figure, linear scale of simulation and measurement results is chosen for convenient comparison with the results in [49], where the magnitude responses of S_{21} increase linearly as the frequencies increase. Good agreements are observed up to 3.7 GHz, which is sufficient for the impulse signal under consideration. Fig. 3.7 shows the result for the phases of the S parameters of the differentiator.

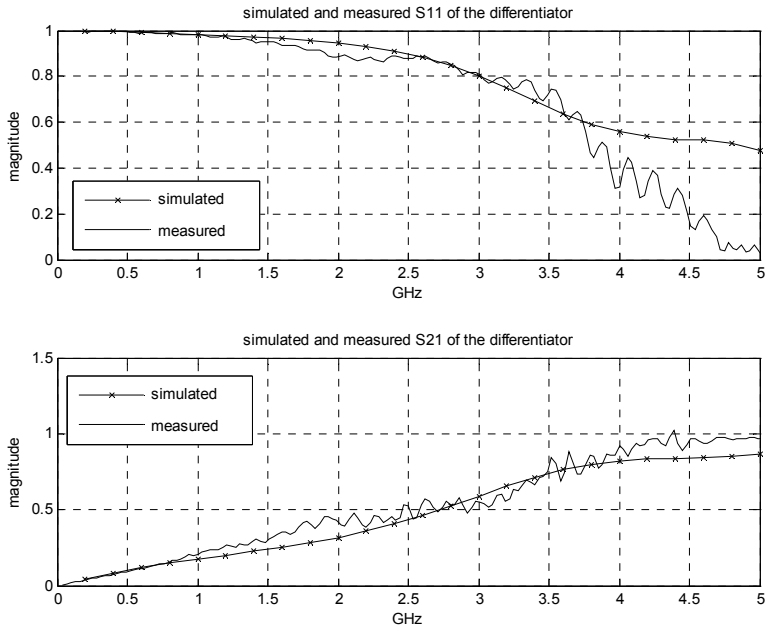

Figure 3.6 Simulated and tested *S* parameters of the differentiator

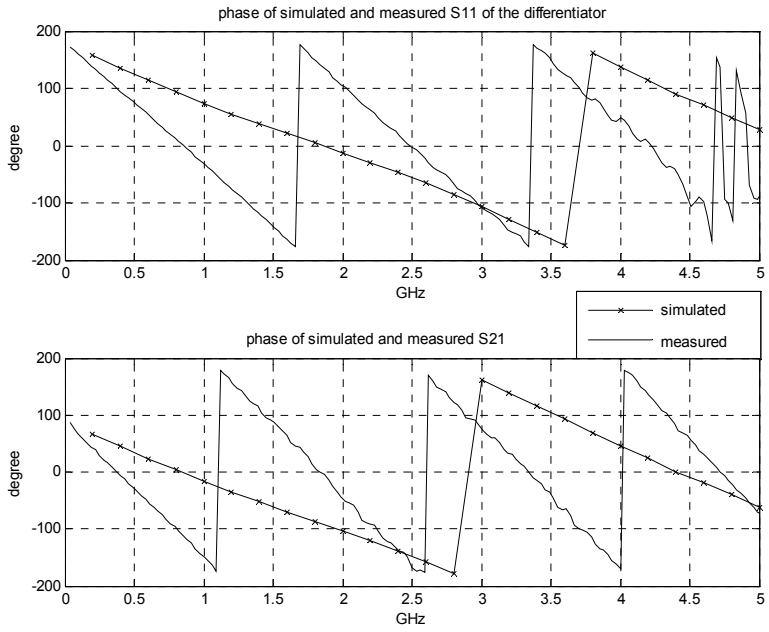

Figure 3.7 Simulated and tested phases of the S parameters of the differentiator

The differentiator was connected to the impulse generator and the derivative of the impulse signal was obtained. Fig. 3.8 shows this Gaussian-like monocycle signal and its spectrum. It is seen that the DC component has been reduced to almost zero and the performance of this differentiator are regarded as satisfactory. It is seen that the peak-value frequency f_c of this Gaussian-like monocycle is at 1.1 GHz.

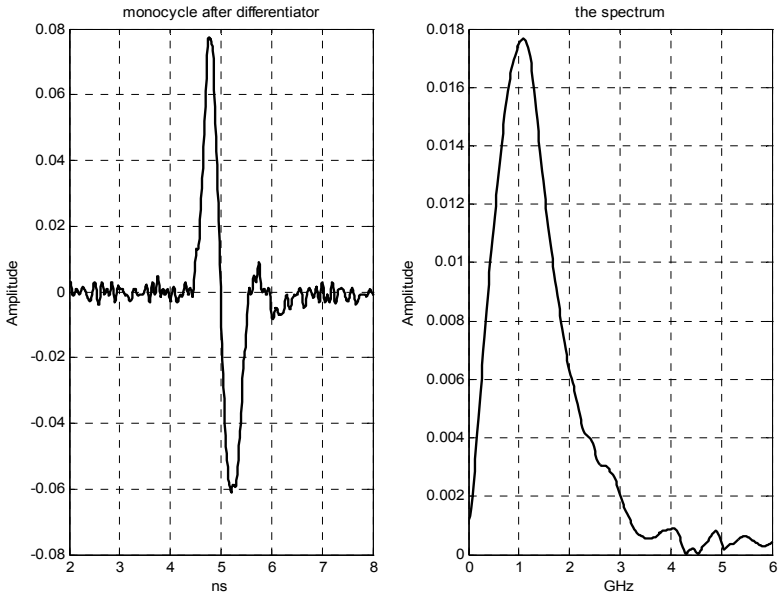

Figure 3.8 The differentiated monocycle and its spectrum

Chapter 4 Coplanar Waveguide and Coplanar Strip Balun

This chapter introduces a wideband balun design for feeding the GPR antennas. To feed the two arms of a bow-tie antenna, two symmetrical transmission lines are needed that are balanced. But for a coaxial cable, if it is connected to the two arms of a bow-tie antenna, the inner conductor and the outer conductor of the coax are not coupled to the antenna in the same way. They provide the unbalance. Thus, we need a *balun* (*bal*ance to *un*balance) to convert the unbalanced current flow of a coaxial cable to the balanced current flow of two symmetrical transmission lines for bow-tie antenna excitation [52]. Though low-cost commercial ferrite baluns [51] are commonly used [59], their bandwidths are not enough and special designs are required for a balun used in UWB system for our application. The presented design can realize not only the unbalanced-to-balanced adaptation, but also the desired impedance transform. Three baluns with different characteristic impedances are discussed and the baluns' performances are tested.

4.1 CPW and CPS

Coplanar waveguide (CPW) and coplanar strip (CPS) are two representatives of coplanar lines, *i.e.*, all their conductors are in the same plane. Some advantages of these two kinds of lines are that mounting lumped components is easy and vias are not required [30]. Due to the symmetry of CPS's two same width lines, it is ideal for providing antenna excitation when a balanced feeding is required. As coaxial cable is widely used for microwave systems, the transition between the

coaxial cable (unbalanced) and the CPS (balanced) is needed. Usually, CPW structure is used between coaxial cable and CPS for balun design due to the convenient transition between CPW and CPS and applications of CPW and CPS balun for feeding printed antennas have been widely studied [31]-[37][41]-[43]. The formulas for calculating the impedances of CPW and CPS are described below for the balun/transformer design.

4.1.1 CPW

The configuration of a CPW with finite width ground plane is shown in Fig. 4.1.

.

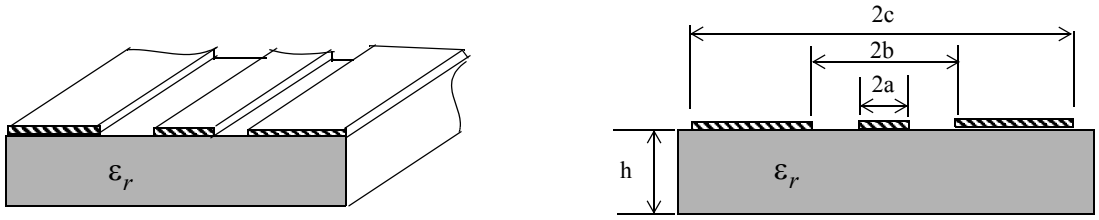

Figure 4.1 CPW with finite width ground plane

To characterize the CPW transmission lines, the quasi-static and full-wave analysis approaches are suggested [30][38]. The analytical expressions of the characteristic impedance of a finite-ground CPW is [30]

$$Z_{0CPW} = \frac{30\pi}{\sqrt{\varepsilon_{re}}} \frac{K'(k_3)}{K(k_3)}, \tag{4.1}$$

where ε_{re} is the effective dielectric constant,

$$\varepsilon_{re} = 1 + \frac{\varepsilon_r - 1}{2} \frac{K(k_4)}{K'(k_4)} \frac{K'(k_3)}{K(k_3)}, \tag{4.2}$$

and where

$$k_3 = \frac{a}{b} \sqrt{\frac{1 - b^2/c^2}{1 - a^2/c^2}} \quad , \tag{4.3}$$

$$k_4 = \frac{\sinh(\pi a/2h)}{\sinh(\pi b/2h)} \sqrt{\frac{1 - (\sinh(\pi b/2h))^2/(\sinh(\pi c/2h))^2}{1 - (\sinh(\pi a/2h))^2/(\sinh(\pi c/2h))^2}} \quad . \tag{4.4}$$

$K(k)$ and $K'(k)$ are the complete elliptic integrals of the first kind and its complement respectively. The complete elliptic integral of the first kind is [39]

$$K(k) = \int_0^1 [(1 - t^2)(1 - kt^2)]^{-\frac{1}{2}} dt. \tag{4.5}$$

$K(k)$ and $K'(k)$ are related to each other by

$$K'(k) = K(k') \text{ with } k' = \sqrt{1 - k^2} \ . \tag{4.6}$$

4.1.2 CPS

Fig. 4.2 shows the structure of the CPS used in this thesis. It is made of two strips of equal width on a dielectric substrate.

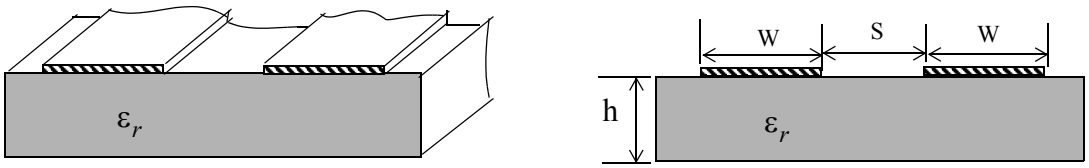

Figure 4.2 CPS with equal strip width

Analyzing the CPS, by the quasi-static method, gives the characteristic impedance as

$$Z_{0CPS} = \frac{120\pi}{\sqrt{\varepsilon_{re}}} \frac{K(k_1)}{K'(k_1)}, \tag{4.7}$$

with the effective dielectric constant

$$\varepsilon_{re} = 1 + \frac{\varepsilon_r - 1}{2} \frac{K(k_2)}{K'(k_2)} \frac{K'(k_1)}{K(k_1)}, \tag{4.8}$$

where

$$k_1 = \frac{S}{S + 2W}, \tag{4.9}$$

$$k_2 = \frac{\sinh(\pi S/4h)}{\sinh(\pi(S + 2W)/4h)}. \tag{4.10}$$

4.2 Chebyshev Transformer

A transformer is used when there is mismatch between the characteristic impedance of a transmission line and the load impedance. It helps to reduce the mismatch reflection, giving a better VSWR. For narrow working bandwith, a single-section quarter-wave transformer will satisfy the impedance match requirement. When more bandwidth is required, one option is to use a multi-section Chebyshev transformer. The formulations for designing the transformer are discussed next.

4.2.1 Single-section Transformer

For a single-section transformer as shown in Fig. 4.3(a), we assume the load impedance Z_L and the feedline characteristic impedance Z_1 are known. They are connected with a lossless transmission line with an unknown characteristic impedance Z_2 and electrical length $\theta = \beta l$. The input impedance Z_{in} is [40]

$$Z_{in} = Z_2 \frac{Z_L + jZ_2 \tan\beta l}{Z_2 + jZ_L \tan\beta l}. \tag{4.11}$$

For the special case when the electrical length is $\lambda/4$, we have $\theta = \beta l = \frac{2\pi}{\lambda}\frac{\lambda}{4} = \frac{\pi}{2}$ and

$$Z_{in} = Z_2 \frac{Z_L / \lim\limits_{\beta l \to \pi/2}(\tan\beta l) + jZ_2}{Z_2 / \lim\limits_{\beta l \to \pi/2}(\tan\beta l) + jZ_L} = \frac{Z_2^2}{Z_L} \quad . \tag{4.12}$$

In order to have no reflection from the load, *i.e.*, $\Gamma = 0$, we must have $Z_{in} = Z_1$. Then the formula for Z_2 is

$$Z_2 = \sqrt{Z_1 Z_L}. \tag{4.13}$$

This shows that a perfect match can be achieved by applying a single-section quarter-wave transformer at the working frequency. Obviously, this is a narrowband match.

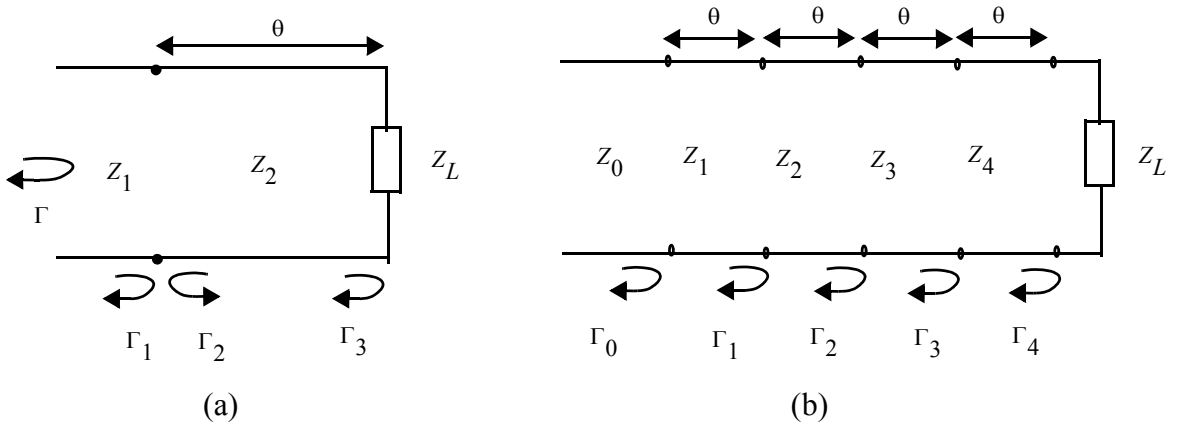

(a) (b)

Figure 4.3 (a) Single section transformer and (b) four-section transformer

For generality and next section's discussion, we consider the case when the electrical length is not at quarter-wave length, *i.e.*, $\theta \neq \pi/2$. The total reflection coefficient is [40]

$$\Gamma = \frac{\Gamma_1 + \Gamma_3 e^{-j2\theta}}{1 + \Gamma_1 \Gamma_3 e^{-j2\theta}}. \tag{4.14}$$

Assuming discontinuities between the impedances Z_1, Z_2 and Z_2, Z_L are small, then $|\Gamma_1 \Gamma_3| \ll 1$, and (4.14) can be approximated as

$$\Gamma \cong \Gamma_1 + \Gamma_3 e^{-j2\theta}. \tag{4.15}$$

where

$$\Gamma_1 = \frac{Z_2 - Z_1}{Z_2 + Z_1}, \quad \Gamma_3 = \frac{Z_L - Z_2}{Z_L + Z_2} \quad . \tag{4.16}$$

It will be shown next that equations (4.15) and (4.16) are very useful for multi-section transformer design.

4.2.2 Four-section Chebyshev Transformer

Fig. 4.3(b) shows the model of a four-section Chebyshev transformer. Assuming Z_0 and Z_L are known, the design goal is to determine the impedance values of Z_1, Z_2, Z_3 and Z_4 for a smooth impedance transform.

From (4.16), the reflection coefficients at each junction are written as

$$\Gamma_0 = \frac{Z_1 - Z_0}{Z_1 + Z_0}, \Gamma_n = \frac{Z_{n+1} - Z_n}{Z_{n+1} + Z_n}, \text{ for n = 1,2,3 and } \Gamma_4 = \frac{Z_L - Z_4}{Z_L + Z_4}. \tag{4.17}$$

Assuming the characteristic impedances increase across the transformer $Z_0 < Z_1 < Z_2 < Z_3 < Z_4 < Z_L$ and Z_L is real, then by using (4.15), the overall reflection coefficient is approximated as

$$\Gamma(\theta) = \Gamma_0 + \Gamma_1 e^{-j2\theta} + \Gamma_2 e^{-j4\theta} + \Gamma_3 e^{-j6\theta} + \Gamma_4 e^{-j8\theta} . \tag{4.18}$$

Further assuming the transformer can be made symmetrical, so that $\Gamma_0 = \Gamma_4, \Gamma_1 = \Gamma_3$, (4.18) can be written as

$$\Gamma(\theta) = e^{-j4\theta}[\Gamma_0(e^{j4\theta} + e^{-j4\theta}) + \Gamma_1(e^{j2\theta} + e^{-j2\theta}) + \Gamma_2]$$

$$= 2e^{-j4\theta}\left(\Gamma_0 \cos 4\theta + \Gamma_1 \cos 2\theta + \frac{1}{2}\Gamma_2\right) \quad . \tag{4.19}$$

The Chebyshev transformer is designed by equating $\Gamma(\theta)$ to a Chebyshev polynomial, which has the characteristics needed for optimizing bandwidth at the expense of bandpass ripple. The first four Chebyshev polynomials are

$$T_1(x) = x,\ T_2(x) = 2x^2 - 1,\ T_3(x) = 4x^3 - 3x,\ T_4(x) = 8x^4 - 8x^2 + 1 . \tag{4.20}$$

Let $x = \cos\theta$ for $|x| < 1$. It can be shown that the Chebyshev polynomials can be expressed as

$$T_n(x) = \cos n\theta, \textit{ i.e. } T_n(\cos\theta) = \cos(n\theta) . \tag{4.21}$$

Since equal ripple is desired in the bandpass of the transformer, it is necessary to map θ_m to $x = 1$ and $\pi - \theta_m$ to $x = -1$, where θ_m and $\pi - \theta_m$ are the lower and upper edges of the pass-band. By replacing $\cos\theta$ with $\cos\theta / \cos\theta_m$ in (4.21), the Chebyshev polynomials are

$$T_n\left(\frac{\cos\theta}{\cos\theta_m}\right) = T_n(\sec\theta_m\cos\theta) = \cos\left[n\sec\left(\frac{\cos\theta}{\cos\theta_m}\right)\right]. \quad (4.22)$$

Since $|\sec\theta_m\cos\theta| \le 1$ from $\theta_m < \theta < \pi - \theta$, the Chebyshev polynomials are $T_n(\sec\theta_m\cos\theta) \le 1$ over the same range.

The fourth polynomial can also be written in the following form if further expanding $(\cos\theta)^n$ [40]

$$T_4(\sec\theta_m\cos\theta) = (\sec\theta_m)^4(\cos 4\theta + 4\cos 2\theta + 3) - 4(\sec\theta_m)^2(\cos 2\theta + 1) + 1. \quad (4.23)$$

Now by making the reflection coefficient $\Gamma(\theta)$ proportional to the fourth Chebyshev polynomial $T_4(\sec\theta_m\cos\theta)$, the Chebyshev equal-ripple passband transformer can be decided by equating (4.19) and (4.23),

$$\Gamma(\theta) = 2e^{-j4\theta}\left(\Gamma_0\cos 4\theta + \Gamma_1\cos 2\theta + \frac{1}{2}\Gamma_2\right) = Ae^{-j4\theta}T_4(\sec\theta_m\cos\theta) \ . \quad (4.24)$$

The constant A can be found by letting $\theta = 0$, corresponding to zero frequency. That gives

$$\Gamma(0) = \frac{Z_L - Z_0}{Z_L + Z_0} = AT_4(\sec\theta_m), \quad (4.25)$$

$$A = \frac{Z_L - Z_0}{T_4(\sec\theta_m)(Z_L + Z_0)}. \quad (4.26)$$

Actually, if the maximum allowable reflection coefficient magnitude in the passband is set as Γ_m,

one gets $\Gamma_m = |A|$ because the maximum value of $T_n(\sec\theta_m \cos\theta)$ is unity in the passband. Thus

$$\sec\theta_m = \cosh\left[\frac{1}{N}\left(\cosh\left(\frac{1}{\Gamma_m}\left|\frac{Z_L - Z_0}{Z_L + Z_0}\right|\right)\right)^{-1}\right] \approx \cosh\left[\frac{1}{N}\left(\cosh\left(\left|\frac{\ln(Z_L/Z_0)}{2\Gamma_m}\right|\right)\right)^{-1}\right], \qquad (4.27)$$

where N is the section number of the transformer.

The fractional bandwith for a tolerated reflection coefficient magnitude Γ_m, is calculated by [40]

$$\frac{\Delta f}{f_c} = 2 - \frac{4\theta_m}{\pi}, \qquad (4.28)$$

where f_c is the center frequency and Δf is the bandwidth.

Substituting $\sec\theta_m$ into (4.23) and (4.24), by equating the similar terms, one finally gets the reflection coefficients

$$\Gamma_0 = \frac{\Gamma_m}{2}(\sec\theta_m)^4, \qquad (4.29)$$

$$\Gamma_1 = 2\Gamma_m(\sec\theta_m)^4 - 2\Gamma_m(\sec\theta_m)^2, \qquad (4.30)$$

$$\Gamma_2 = 3\Gamma_m(\sec\theta_m)^4 - 4\Gamma_m(\sec\theta_m)^2 + \Gamma_m, \qquad (4.31)$$

and the characteristic impedance values of the Chebyshev transformer for all the four sections

$$Z_1 = e^{(\ln Z_0 + 2\Gamma_0)}, \tag{4.32}$$

$$Z_2 = e^{(\ln Z_1 + 2\Gamma_1)}, \tag{4.33}$$

$$Z_3 = e^{(\ln Z_2 + 2\Gamma_2)}, \tag{4.34}$$

$$Z_4 = e^{(\ln Z_3 + 2\Gamma_1)}. \tag{4.35}$$

Based on the above equations, Table 4.1 shows the design parameters for three Chebyshev transformers which transform 50Ω characteristic impedance to 80Ω, 100Ω and 120Ω for the maximum reflection coefficient $\Gamma_m = 0.05$. It is noted that the fractional bandwidth $\frac{\Delta f}{f_c}$ decreases as the impedance increases.

Table 4.1: Three four-section Chebyshev transformers design

	80Ω	100Ω	120Ω
Z_0	50	50	50
Z_1	54.73	55.92	56.87
Z_2	60.03	64.86	69.03
Z_3	66.63	77.09	86.92
Z_4	73.09	89.42	105.51
Z_L	80	100	120
θ_m(degree)	30.40	35.15	37.86
$\Delta f / f_c$	1.325	1.219	1.159

4.3 Wideband Balun

A wideband CPW/CPS balun, which has S_{11} characteristics better than -10 dB in the frequency range from 0.1 GHz to 3.85 GHz, has been reported and it has been used for feeding a logarithmic spiral antenna for GPR [41]-[43]. The balun was designed not only to meet the unbalanced-to-balanced transformation requirement, but also to satisfy the impedance match over a wide bandwidth by using a Chebyshev transformer to convert the 50Ω impedance of a coax cable to 80Ω of the antenna input impedance. Its design is explained below.

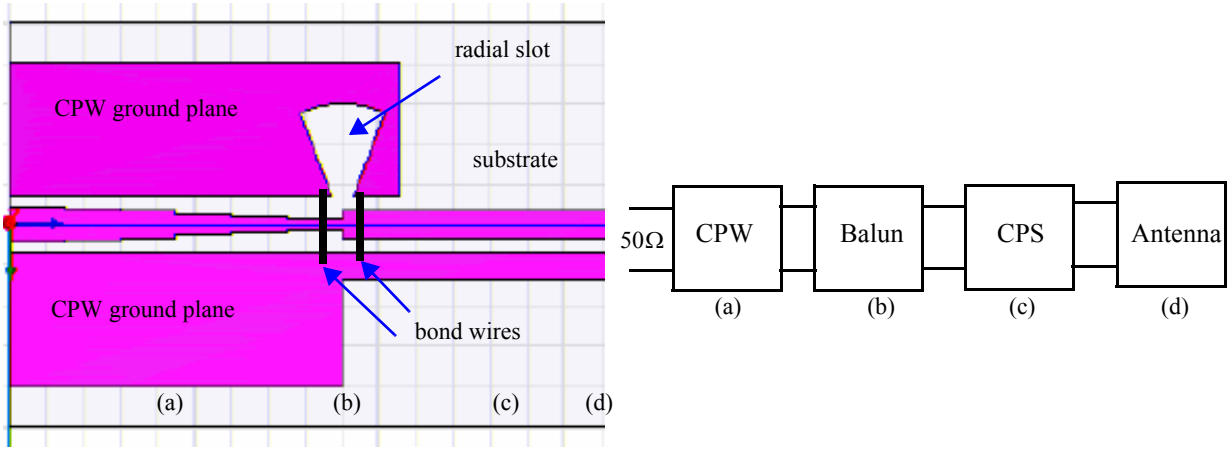

I. CPS-CPW balun top view II.Balun block diagram

Figure 4.4 CPW/CPS balun structure

The wideband balun model is made of four parts as shown in Fig. 4.4. In this figure, part (a) is the CPW section with the four-section Chebyshev impedance transformer which transforms the 50 Ω impedance to the antenna input impedance. The actual unbalanced-to-balanced transformation is realized at (b) where the CPS configuration is used and the characteristic impedance of the CPS is

designed to be the same as the antenna input impedance. Part (c) is just an extension of the CPS and the two balanced CPS lines are directly connected to the antenna at part (d). To make the balun widebanded, a 45^{o} radial slot and two bond wires with a diameter of 0.15 *mm* near the CPW-CPS transition plane are used. The radial slot represents a very wideband open circuit, which forces the electrical field to be between the two conductors of the CPS. The two bond wires ensure that the potential on the two ground planes is equal. The exact details are in [41].

It was decided to design such a balun for feeding our antenna. Since 100Ω was the antenna input impedance reported in [22] which provides the prototype of the bow-tie antenna in the thesis and because of the uncertainty and difficulty of deciding our antenna's actual input impedance, three baluns with impedances at 80Ω, 100Ω and 120Ω were designed and fabricated on Rogers RT/ Duroid 6010LM substrate with thickness 0.635 *mm* and $\varepsilon_r = 10.2$. The ground plane widths of the CPW part are chosen to be 2.5 times the distance between the two ground planes as suggested in [41]. Because of the difficulty of excitation model in HFSS 9.2 and Ansoft Designer, it was decided to choose 3 *mm* as each CPW section's length [41]. Though the reported resonant frequency is 1.9 GHz, the reflection coefficient (S_{11}) was better than –10 dB for a frequency band from DC to 3.85 GHz and this is sufficient for our monocycle.

4.3.1 80Ω balun

To make the 80Ω balun, the conductor widths are calculated based on the desired impedance values in Table 4.1 on page 40 and the calculated CPW/CPS impedance are shown in Fig. 4.5. The spacing between the two ground planes of the CPW section was chosen as 2.9 *mm* and the ground

plane width was decided to be 7.25 *mm.* The gabs, which are the distances from the outer edges of the center conductors to the ground plane, are then decided accordingly as shown in Table 4.2.

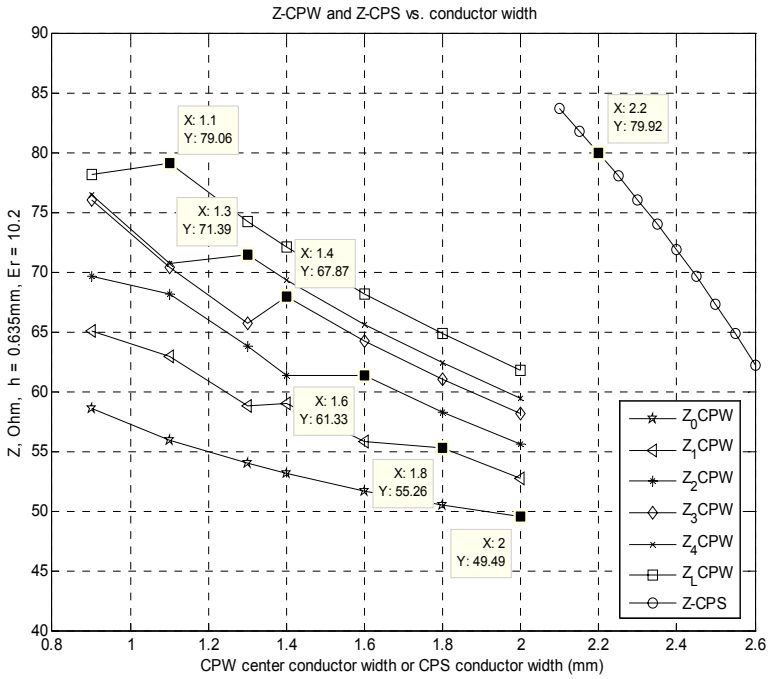

Figure 4.5 Calculated CPW/CPS Z_0 and conductor widths for 80Ω balun

Table 4.2: 80Ω balun parameters

80 Ω Balun	CPW Chebyshev transformer section						CPS
Desired impedance (Ω)	50	54.7	60.3	66.6	73.1	80	80
Designed impedance (Ω)	49.49	55.26	61.33	67.87	71.39	79.06	79.92
Conductor width (*mm*)	2	1.8	1.6	1.4	1.3	1.1	2.2
Gab between center conductor and ground plane (*mm*)	0.45	0.55	0.65	0.75	0.8	0.9	--
Spacing between CPW ground planes or CPS conductors (*mm*)	2.9						0.35
Ground plane width (*mm*)	7.25						--

After soldering a 80Ω surface-mounted resistor to the CPS lines, S_{11} of the balun was tested by using an Anritsu 360B network analyzer as shown in Fig. 4.6. It is seen that good S_{11} with amplitude bellow -10 dB is obtained over a bandwidth of 0.04-3 GHz and at the resonant frequency about 1.8 GHz, S_{11} can reach as low as -40 dB. A picture of the balun is shown in Fig. 4.7.

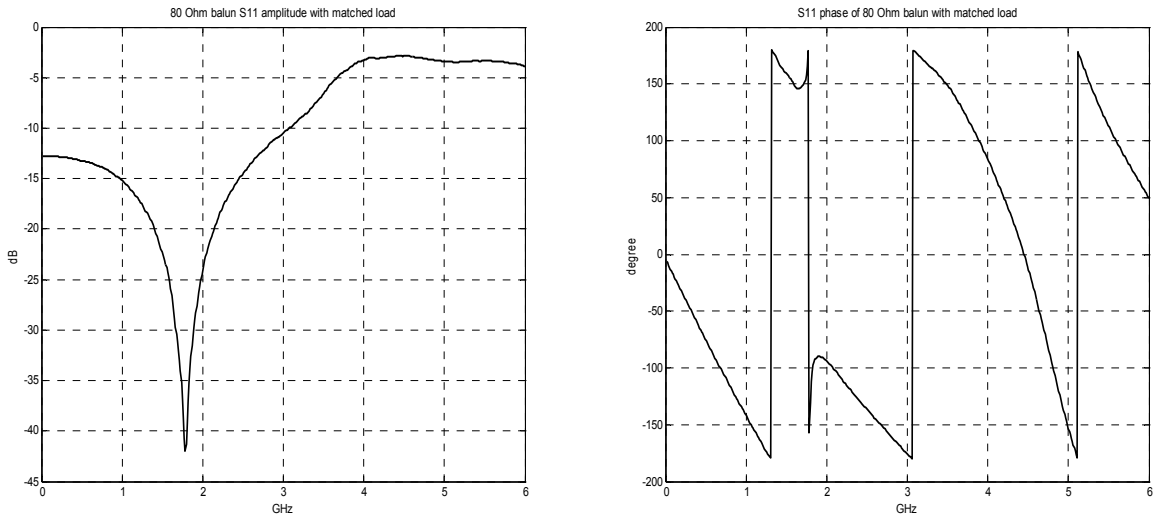

(a) (b)

Figure 4.6 Measured S_{11} of the 80Ω balun: (a) amplitude; (b) phase

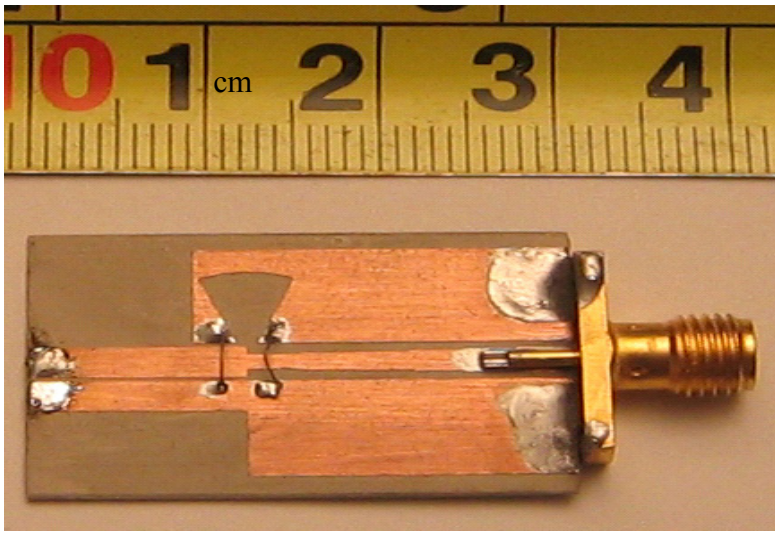

Figure 4.7 80Ω balun picture

4.3.2 100Ω Balun

Similarly, a 100Ω balun was designed and fabricated. For this balun, the spacing between the CPW grounds was carefully chosen as 2.7 *mm*. Fig. 4.8 shows the calculated impedance values and the conductor widths. Conductor dimensions of this balun are listed in Table 4.3 on page 46.

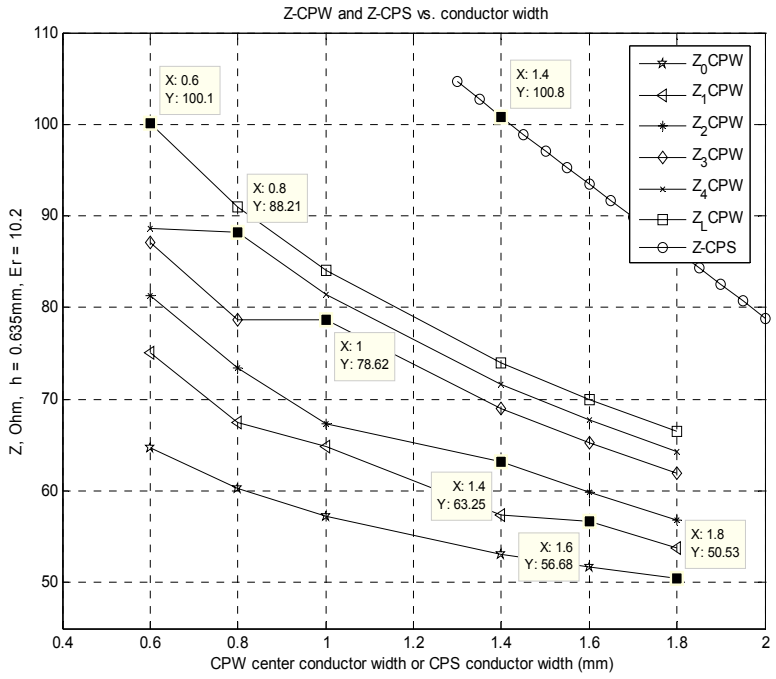

Figure 4.8 Calculated CPW/CPS Z_0 and conductor widths for 100Ω balun

Table 4.3: 100Ω balun parameters

100 Ω Balun	CPW Chebyshev transformer section						CPS
Desired impedance (Ω)	50	55.9	64.9	77.1	89.4	100	100
Designed impedance (Ω)	50.53	56.68	63.24	78.62	88.21	100.07	100.8
Conductor width (*mm*)	1.8	1.6	1.4	1	0.8	0.6	1.4
Gab between center conductor and ground plane (*mm*)	0.45	0.55	0.65	0.85	0.95	1.05	--
Spacing between CPW ground planes or CPS conductors (*mm*)	2.7						0.65
Ground plane width (*mm*)	6.75						--

Again, a matched resistor is connected to the CPS end and S_{11} was tested as shown in Fig. 4.9. It is seen that the best S_{11} of -27 dB is achieved at about 2 GHz.

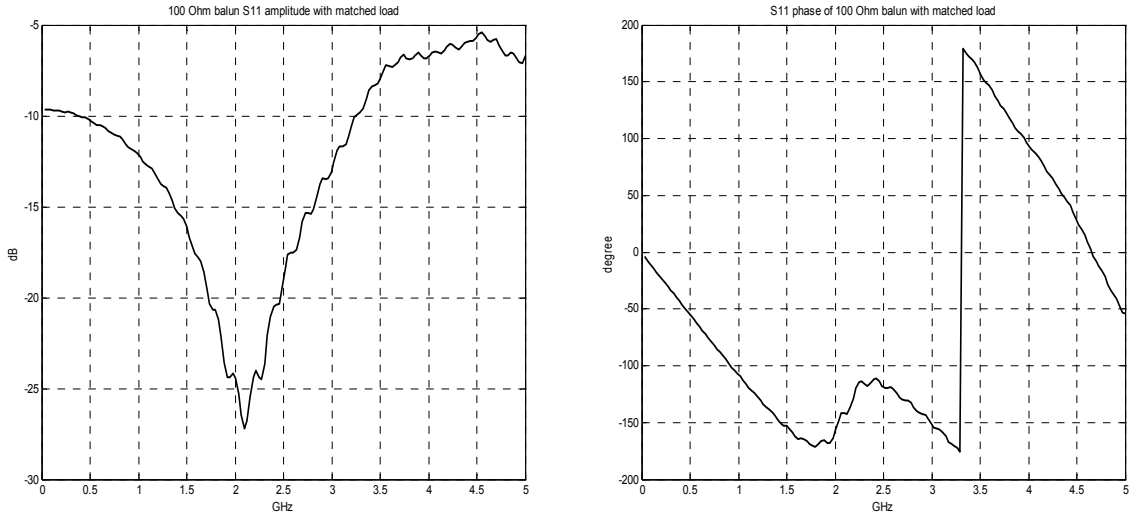

(a) (b)

Figure 4.9 Measured S_{11} of the 100Ω Balun: (a) amplitude; (b) phase

4.3.3 120Ω Balun

A 120Ω balun was made by the same method. It was found that with the increase of the CPW characteristic impedance, the impedance value becomes very sensitive against the conductor width. After calculating the designing parameters of a 150Ω balun, it became extremely difficult to satisfy both the conductor dimensions and impedance requirements. The attempt to make balun with impedance higher than 120Ω was abandoned. It is noted that though the theoretical principles for this Chebyshev-transformer-balun are not difficult, the 80Ω balun in [41] seems the only reported application. The 120Ω balun design procedure is shown in Fig. 4.10 and the design parameters in Table 4.4. It is seen that for small conductor width and large value impedance, the impedance value increases very sharply.

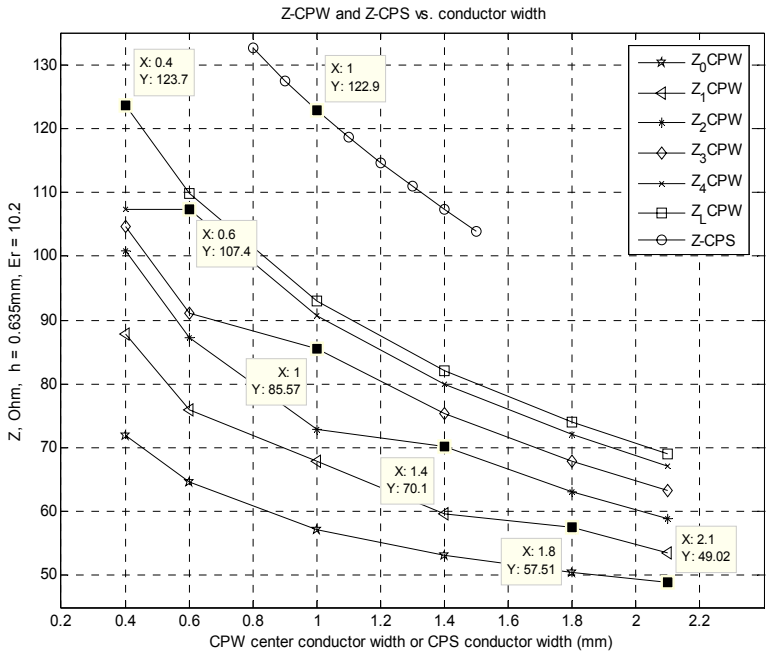

Figure 4.10 Calculated CPW/CPS Z_0 and conductor widths for 120Ω Balun

Table 4.4: 120Ω balun parameters

120 Ω Balun	CPW Chebyshev transformer section						CPS
Desired impedance (Ω)	50	56.9	69	86.9	105.5	120	120
Designed impedance (Ω)	49.02	57.51	70.1	85.57	107.4	123.7	122.9
Conductor width (*mm*)	2.1	1.8	1.4	1	0.6	0.4	1
Gab between center conductor and ground plane (*mm*)	0.45	0.6	0.8	1	1.2	1.3	--
Spacing between CPW ground planes or CPS conductors (*mm*)	3						1
Ground plane width (*mm*)	7.5						--

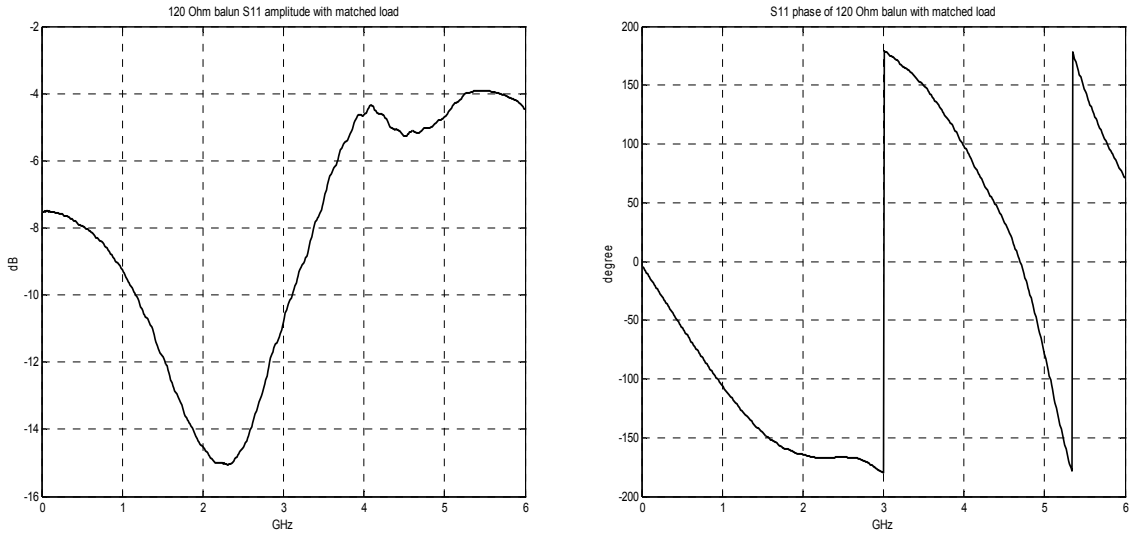

(a) (b)

Figure 4.11 Measured S_{11} of the 120Ω Balun: (a) amplitude; (b) phase

The measured S_{11} with a 120Ω matched load is shown in Fig. 4.11. The bandwidth of -10 dB S_{11} is not good as the previous two and the lowest S_{11} is only at about -15 dB. The reasons are discussed in the following for this highest-impedance-value balun:

1) Based on the design procedure of the Chebyshev transformer in Section 4.2, it is predicted that for higher value impedance transformers with same input impedance, $\Delta f/f_c$ will decreases. Calculated results show $\Delta f/f_c$ is 1.325, 1.219 and 1.159 for 80Ω, 100 Ω and 120 Ω balun respectively. This trend can be further verified if we design a 50-150 Ω and a 50-180 Ω transformers. The fractional bandwidths for these two transformers are 1.102 and 1.066 separately. It is probably not practical to make a high ratio four-section Chebyshev transformer (for example, 50Ω-200 Ω with the ratio of 4:1) for a wideband balun application. This might be a reason that no CPW/CPS balun with impedance above 80Ω have been reported.

2) From Table 4.2 on page 43, Table 4.3 on page 46 and Table 4.4 on page 48, if we summarize the impedance values at the CPW/CPS transition plane, we get the following table:

Table 4.5: Impedance comparison at the CPW/CPS transition

	80 Ω Balun		100 Ω Balun		120 Ω Balun	
	Z-CPW	Z-CPS	Z-CPW	Z-CPS	Z-CPW	Z-CPS
Desired (Ω)	80	80	100	100	120	120
Designed (Ω)	79.06	79.92	100.07	100.8	123.7	122.9

From this table, we see that the largest impedance difference between the desired value and designed value occurs for the 120Ω balun case because there is not much choice when deciding the CPW and CPS conductor widths.

3) For the 120Ω balun, precise fabrication plays a more important role than for the other two baluns because large-impedance-value CPW/CPS is more sensitive to the conductor width. Since the precision limit of the milling fabrication process can reach is 0.2 *mm*, one obvious problem is the un-avoidable difficulty for fabricating 90^o corners. Taking into account that, in total, there are twelve such corners for making such a balun, this fabrication error will certainly affect the balun's desired functionality. The illustration of this systematic error at each CPW/CPS stage is shown in Fig. 4.12.

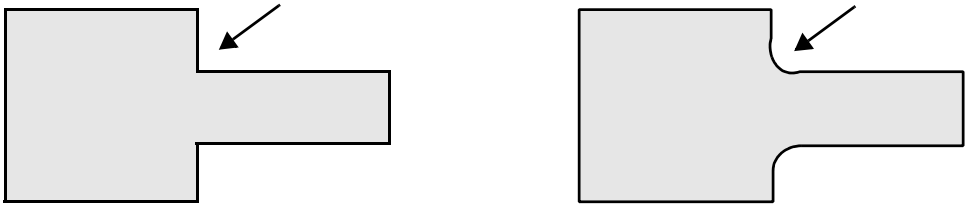

(a) designed (b) fabricated

Figure 4.12 The systematic error during fabrication

Chapter 5 RC-Loaded Circular Bow-tie Antenna

Due to the advantages of wide bandwidth characteristics, easy fabrication and low-cost, bow-tie antenna has been one of the commonly used antennas for GPR [21]-[27]. Because of its planar geometry, the impedance loading for bow-tie antenna is relatively easy to realize impulse radiation [21]-[27]. These reasons have decided that the bow-tie antenna is a very promising candidate for our impulse GPR research. This chapter reviews and introduces the details of the RC-loaded bow-tie antennas built for pulse radiation. Simulation results are presented and the antenna input impedances are computed from frequency-domain measurements.

5.1 Circular Bow-tie Antennas

Based on the geometrical approximations of biconical antennas, bow-tie antennas are a variation on broadband biconical antennas. They are often used because the solid or shell biconical structure is usually too massive for practical use [52]. Since the metal sheet needed for bow-tie antennas is hard to support, bow-tie antennas are usually made on dielectric substrates. Because of the advantages mentioned above, bow-tie antennas have been widely studied for impulse radiation and impulse GPR [15][22]-[27][29][31][32]. The first slotted, circular bow-tie antenna with a combination of a resistive and a tapered capacitive loading for GPR was presented in [53], where the antenna was studied and the current distribution on the surface of the antenna was discussed. It

showed that for a conventional bow-tie antenna without slots, the currents are concentrated at the feed point and along the two edges of the antenna. But for a circular bow-tie antenna with tapered capacitive loading, which was realized by constructing an array of slots with increasing slot width on the antenna surface, the currents are concentrated not only at the feed point, but also on the slotted surface of the bow-tie antenna. This means that each slot is acting as a secondary radiation source. The paper further suggests that applying resistive loading on the slot surface can effectively reduce the late-time ringing without affecting the main radiation from the feed point. Reported progress on this design can be found in [22][23][54].

5.2 RC-Loaded Bow-tie Antenna

Impedance loading techniques are commonly used to minimize the late-time ringing effect. Although the Wu-King profile [16] can be used for determining the resistive load distribution along the antenna in order to expand the antenna bandwidth, the disadvantage of resistive loading is that it drops the radiation efficiency down to as low as 23% [56]. To deal with this problem, the applications of capacitive and resistive-capacitive (RC) loading with linear/non-linear profiles have been proposed [17][18]. As capacitive loading alone cannot suppress late-time ringing [22][58], in recent years, a combined RC-loading with linear capacitive and constant resistive loading profile has been suggested [29][22][23]. The bow-tie antenna bandwidth is improved by rapidly decreasing antenna current distribution almost linearly towards the antenna ends. Thus, resonances are not set up.

From [29], where a linear capacitive and constant resistive profile of an RC loading is investigated, the loading is expressed as an impedance per unit length as

$$Z(z) = R - jX = R - jR_X z \tag{5.1}$$

where R is the constant resistance per unit length, $X = R_x z$ is the reactance per unit length and z is the position along the antenna.

Assuming antenna capacitance profile $C(z)$ at position z, the lumped capacitance from z_n to z_{n+1}, where z_n is the starting position and z_{n+1} is the stopping position of the nth slot, can be written as

$$C_n = \left[\int_{z_n}^{z_{n+1}} \frac{1}{C(z)} dz \right]^{-1}, \tag{5.2}$$

and the reactance is

$$X_n = \frac{1}{\omega C_n} = \frac{1}{\omega} \int_{z_n}^{z_{n+1}} \frac{1}{C(z)} dz, \tag{5.3}$$

where ω is the working frequency and $C(z)$ is the capacitance at position z. Though the above equation (5.3) for X_n is an inverse linear relationship with $C(z)$, a nearly linear current distribution decrease was achieved from the feeding point towards the antenna ends by linearly decreasing the capacitances in the same direction [29]. To apply this linear/constant capacitive-resistive

loading scheme, the slotted bow-tie antenna was suggested and it is explained in the following [22]:

1) Linear capacitive loading profile

The proposed RC loading method is shown in Fig. 5.1, where slots are cut along the antenna and microwave absorber material is added at the antenna surface. Since the capacitance across the slot decreases inversely with the slot width [22][44], this loading technique can realize approximate linear reactance increase, by linearly increasing the slot width towards the antenna ends.

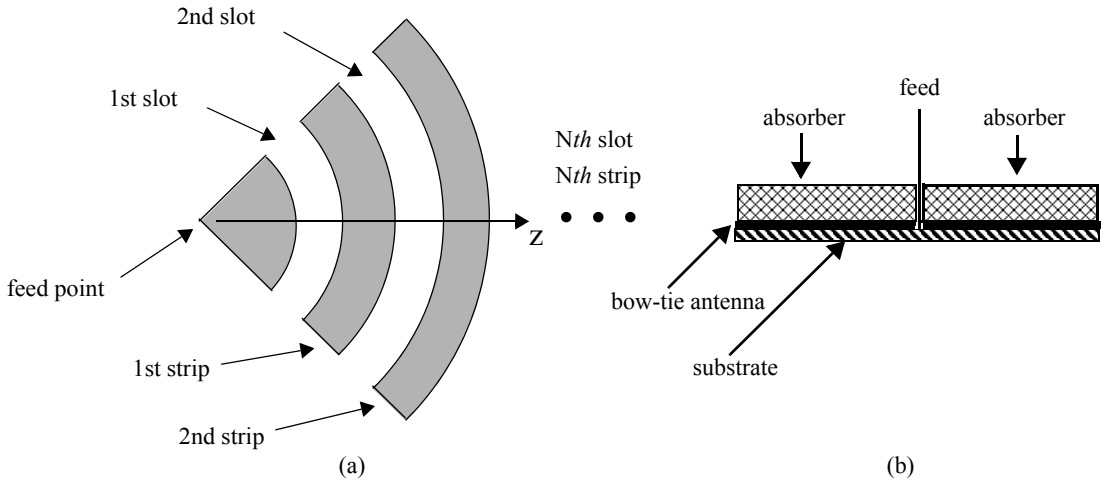

Figure 5.1 (a) Slots and strips of antenna's one arm; (b) absorbers to realize RC loading

2) Constant resistive loading profile

Using volumetric microwave absorbers to realize the resistive loading, the equivalent resistance along the antenna is determined by the slot areas which are covered by absorbers. Though the resistance across a slot is proportional to the slot width, the resistive profile per unit length across

the slots along the antenna's radius direction is a constant, because the resistance of the absorber per unite length across the slots is not changing along the radius direction. Another advantage of using absorbers is that the absorber reduces the radiation from antenna's metal side alone while the radiation at the other side, which is facing the ground, is only slightly affected [22]. To attenuate the current distribution along the antenna, the slot widths can be linearly increased so that the total equivalent resistance across the slots R_n, are linearly increasing, resulting in rapid current distribution decrease and no waveform reflection at the antenna ends.

5.3 Antenna Design Parameters

The design of our antenna was based on that of [22] and [29]. The theoretical analysis of RC loading in [29] suggested that the reactance profile at the antenna end be set to 25 $jk\Omega/m$. In [22], the circular bow-tie antenna radius was chosen as 25 *cm* so that, to achieve 25 $jk\Omega/m$ at the end of the antenna, the reactance profile was set to increase 1 $jk\Omega/m$ per *cm* along the antenna. It was further assumed that the first slot width $d_1 = 0.2mm$, as shown in Fig. 5.2, corresponds to a reactance profile of 1 $jk\Omega/m$, then the last linearly increasing slot width $d_N = 25 \times d_1 = 5$ *mm* corresponds to a reactance profile value of 25 $jk\Omega/m$ at the antenna end. To have a smooth reactance variation towards the antenna end, slot size increase $d_{n+1} - d_n$ was chosen as 0.1 *mm*. The strip width was determined to vary in a similar way but in the opposite direction while keeping the relationship $d_n + w_n = 5mm$. The last strip width was also chosen as 0.2 *mm*, the smallest value that photo-etching technology can realize. The reported results in [22] show that the peak

value of the transmitted pulse is 54% higher than the same circular bow-tie antenna without loading.We decided to utilize the above RC-loading scheme as in [22] and [29] in the thesis. The following sections discuss the implemented antenna design.

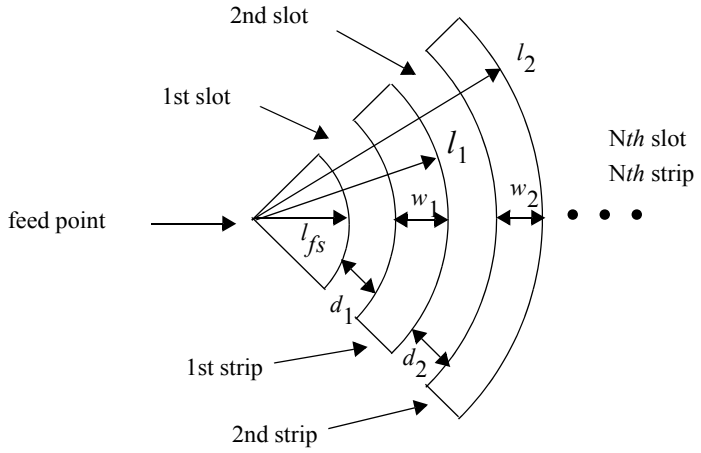

Figure 5.2 Slots and strips sizes

a) Antenna radius and flare angle

The radius of the circular bow-tie antenna should be as large as possible for good low frequency radiation. As such, the radius of the circular bow-tie was selected as 27.5 *cm,* based on the maximum available substrate plate size. The total length of the antenna was therefore 55 *cm*. In this case, the substrate used is Arlon-AD300 material with $\varepsilon_r = 3$ [55]. The flare angle was taken as 90^o, the same as suggested in [22].

b) First slot distance l_{fs}

To transmit the most electromagnetic energy into the ground in the broadside direction, the first slot distance l_{fs} from the feeding point, as shown in Fig. 5.2, has to be calculated based on the peak-value frequency f_c of the monocycle's spectrum. From the knowledge that the length of a dipole antenna should be a quarter wavelength to obtain the maximum transmitted signal, one gets

$$l_{fs} = \frac{c_{substrate}}{4f_c}, \tag{5.4}$$

where $c_{substrate}$ is the wave velocity in the substrate.

From Chapter 3 (Fig. 3.8 on page 29), we know that the peak-value frequency of the monocycle is $f_c = 1.1$ GHz. Therefore $l_{fs} = 39.3$ *mm* from the above equation (5.4). To more easily fit the slot increase along the radius direction, this value was chosen as 40 *mm*.

c) Slot and strip sizes

In [22], a reactance profile with an increase of $1jk\Omega/m$ per *cm* along the antenna was assumed so that the $25jk\Omega/m$ reactance profile at the antenna end could be achieved for the 25 *cm* antenna. Since the same $\varepsilon_r = 3$ material is used for the antenna reported in this thesis, we have also assumed the same reactance profile increase along the antenna. But because our antenna length is longer, at the end of the antenna, we get the reactance profile as $27.5jk\Omega/m$, close to $25jk\Omega/m$,

which is the assumed reactance profile at the end of the 25 *cm* bow-tie antenna in [22]. Because of the resistive loading, the current distribution will decrease sharply to zero at the position close to the antenna end. Using the fact that the minimum resolution of the milling machine we had access is 0.2 *mm*, we can then design the slot and strip size. The increase in slot width is thus chosen to be 0.1 *mm* to ensure a smooth variation of capacitance. The strip width increase is also chosen as 0.1 *mm,* but starting from the antenna end. According to the size of our substrate, $d_n + w_n = 5mm$ is chosen as the step for l_n, same as in [22]. Fig. 5.3 shows a picture of the fabricated antenna soldered with a balun and Table 5.1 lists the slot and strip widths for our antenna design.

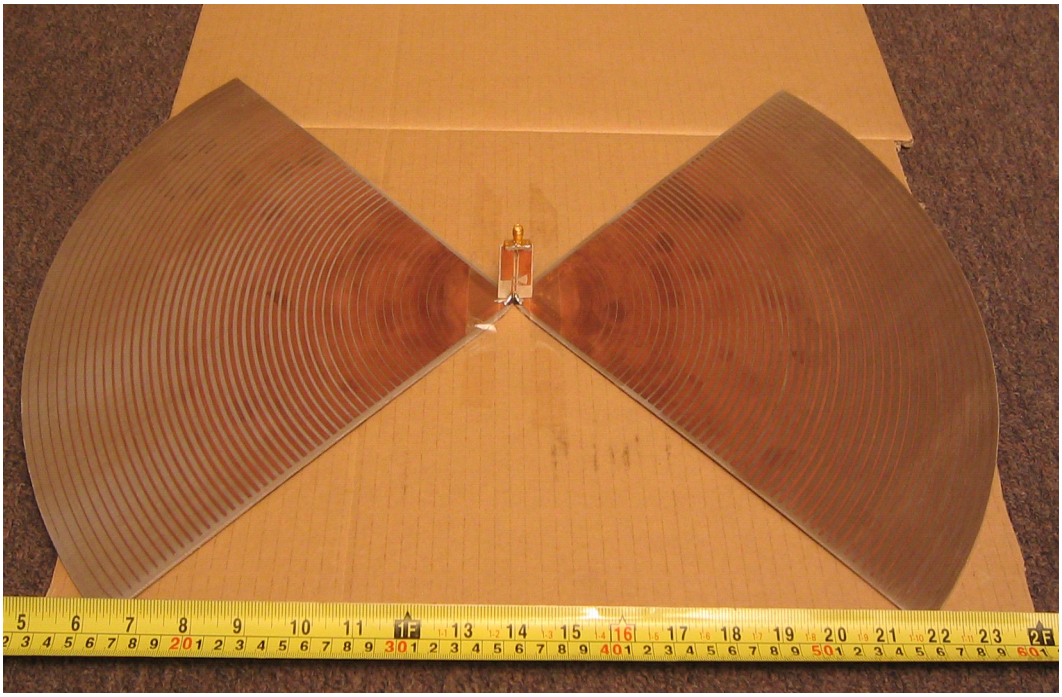

Figure 5.3 Fabricated circular bow-tie antenna soldered with a balun

Table 5.1: Antenna slot and strip size

n	l_n (*mm*)	Slot width d_n (*mm*)	Strip width w_n (*mm*)	*n*	l_n (*mm*)	Slot width d_n (*mm*)	Strip width w_n (*mm*)
0	40	-	-	*24*	160	2.5	2.5
1	45	0.2	4.8	*25*	165	2.6	2.4
2	50	0.3	4.7	*26*	170	2.7	2.3
3	55	0.4	4.6	*27*	175	2.8	2.2
4	60	0.5	4.5	*28*	180	2.9	2.1
5	65	0.6	4.4	*29*	185	3.0	2.0
6	70	0.7	4.3	*30*	190	3.1	1.9
7	75	0.8	4.2	*31*	195	3.2	1.8
8	80	0.9	4.1	*32*	200	3.3	1.7
9	85	1.0	4.0	*33*	205	3.4	1.6
10	90	1.1	3.9	*34*	210	3.5	1.5
11	95	1.2	3.8	*35*	215	3.6	1.4
12	100	1.3	3.7	*36*	220	3.7	1.3
13	105	1.4	3.6	*37*	225	3.8	1.2
14	110	1.5	3.5	*38*	230	3.9	1.1
15	115	1.6	3.4	*39*	235	4.0	1.0
16	120	1.7	3.3	*40*	240	4.1	0.9
17	125	1.8	3.2	*41*	245	4.2	0.8
18	130	1.9	3.1	*42*	250	4.3	0.7
19	135	2.0	3.0	*43*	255	4.4	0.6
20	140	2.1	2.9	*44*	260	4.5	0.5
21	145	2.2	2.8	*45*	265	4.6	0.4
22	150	2.3	2.7	*46*	270	4.7	0.3
23	155	2.4	2.6	*47*	275	4.8	0.2

5.4 Simulations

The simulation package HFSS 9.2 was used to simulate the designed antennas, as shown in Fig. 5.4. Three different cases were simulated: 1) whole-body antenna, where the whole antenna with radius of 27.5 *cm* was made of copper; 2) capacitive loaded antenna, where slots and strips were added; 3) RC-loaded antenna, where resistive load was applied to the slots. The difficulty for the simulation is that the characteristics of the microwave absorber are unknown because there is no known way to derive its characteristic parameters when it is used as resistive load, as the attenuation will be concentrated only at the absorber surface. However, the desired resistive loading is realized in HFSS by defining the slot areas as finite conductor by using a flat piece SFC-4 absorber from Cuming Corp [57]. Its electrical characteristics are approximated by relative permittivity $\varepsilon_r = 2$, bulk conductivity $\sigma = 0.073$ *mho/m* and loss tangent $\tan\delta = 0.327$ [59]. The strip material was defined as copper. A 100Ω $2mm \times 2mm$ lumped port was used for antenna excitation and this value was the balanced line impedance used in [22]. Fig. 5.5 to Fig. 5.10 show the simulation results.

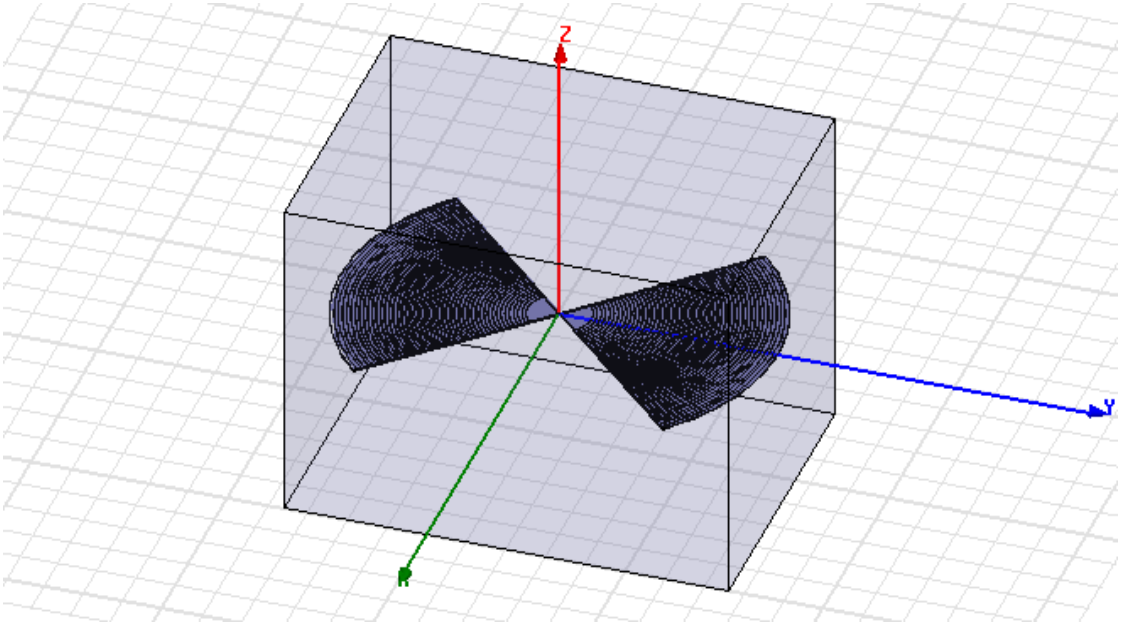

Figure 5.4 HFSS 9.2 simulation model for RC-loaded antenna

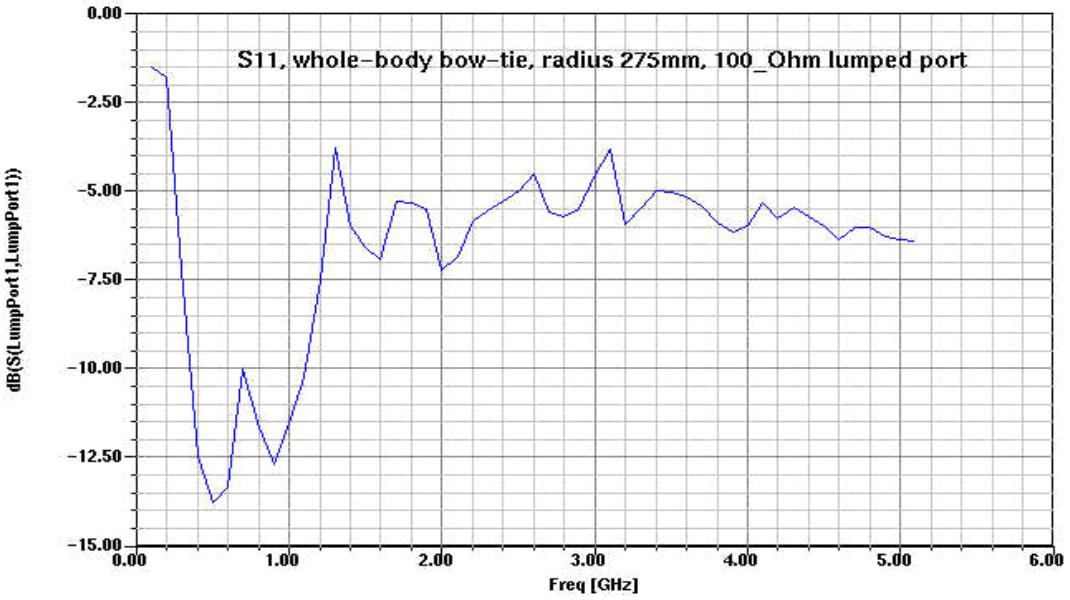

Figure 5.5 Simulation S_{11} result of whole-body bow-tie

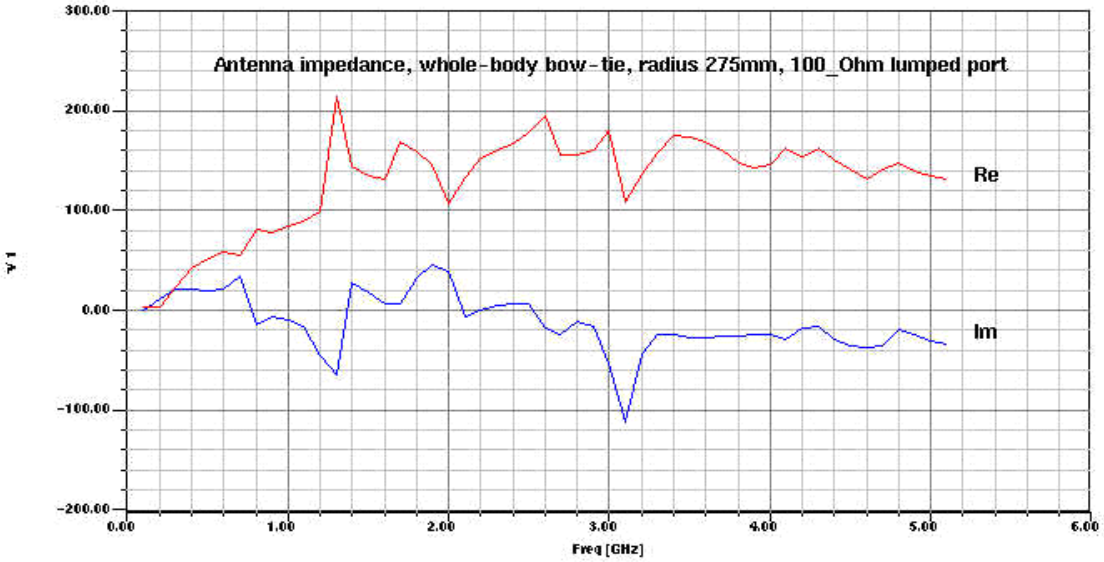

Figure 5.6 Simulation result of antenna impedance of whole-body bow-tie

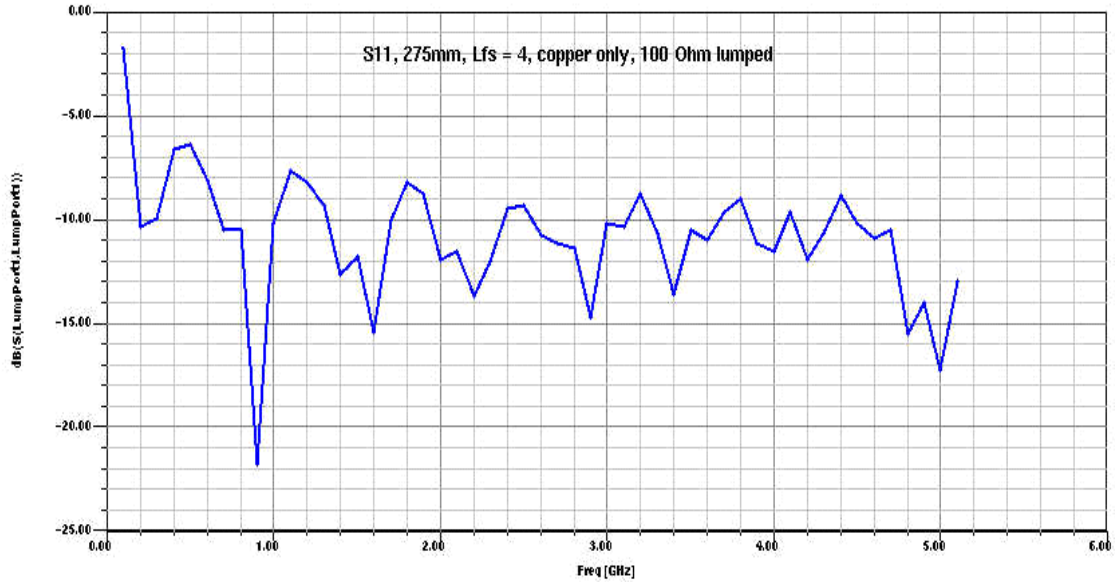

Figure 5.7 Simulation S_{11} result of capacitive-loaded bow-tie

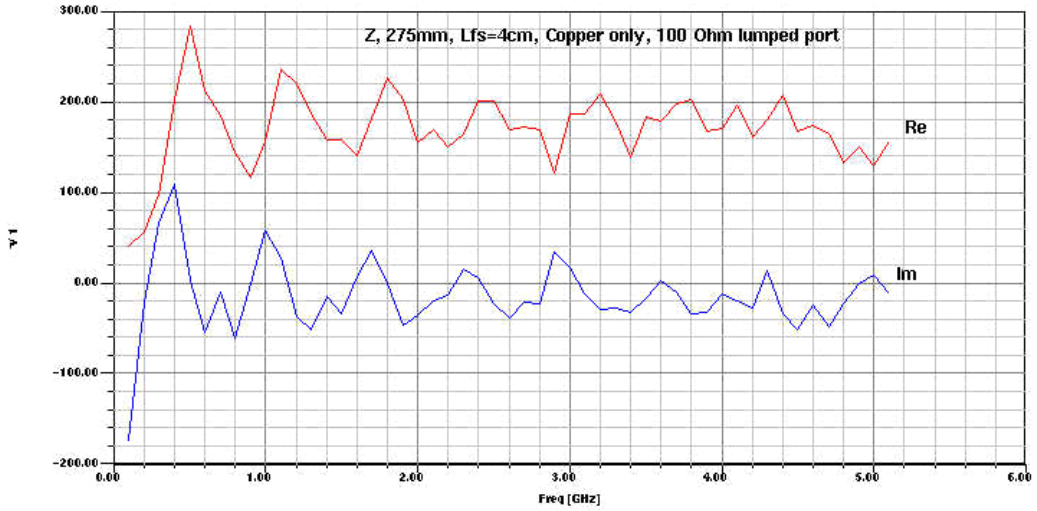

Figure 5.8 Simulation result of antenna impedance of capacitive-loaded bow-tie

Figure 5.9 Simulation S_{11} result of RC-loaded bow-tie

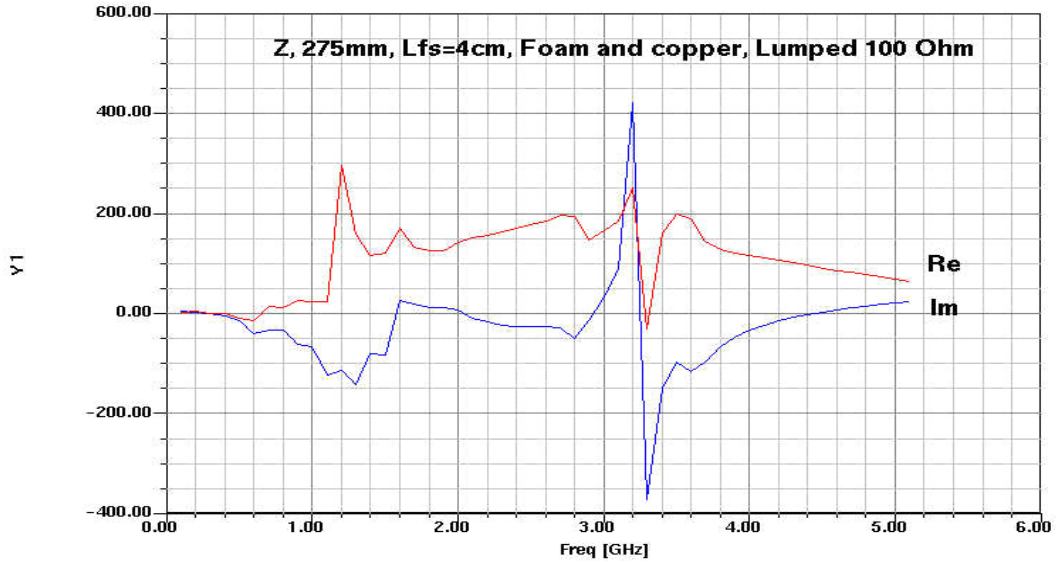

Figure 5.10 Simulation result of antenna impedance of RC-loaded bow-tie

It is seen that the whole-body antenna is good for low frequency radiation because of its large size. The wide bandwidth characteristics are verified from the capacitive-loaded bow-tie results in Fig. 5.7 and it is noticed that for the RC-loading, S_{11} parameters become larger when frequency is between 3 GHz to3.8 GHz and drop to bellow -10 dB again after 3.8 GHz. Probably because of the uncertainty of the characteristics of the microwave absorber, as stated on page 61, the simulated impedances were different from those measured in [22], where the measured resistance was reported around 100Ω from about 0.3 GHz to 5 GHz. But what kind of absorber was used in [22] is unknown. Field patterns were also obtained by simulations and it was found they are very similar at same frequencies. Fig. 5.11 and Fig. 5.12 give the simulated total field patterns for the resistive-capacitive load case.

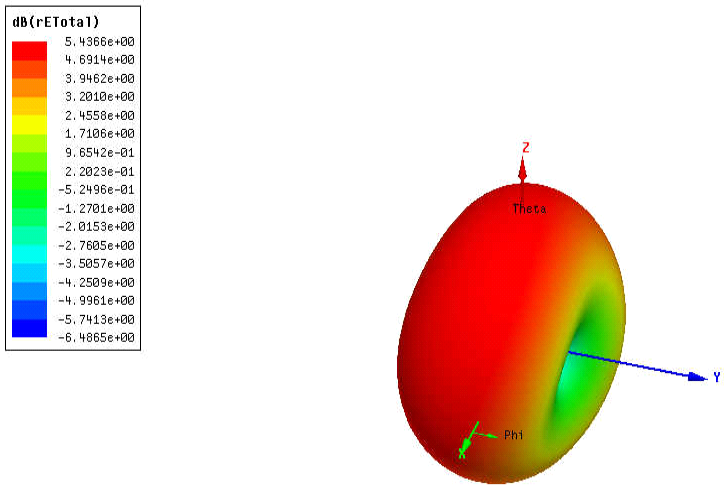

Figure 5.11 Total field pattern at 100 MHz for the RC-loaded bow-tie antenna

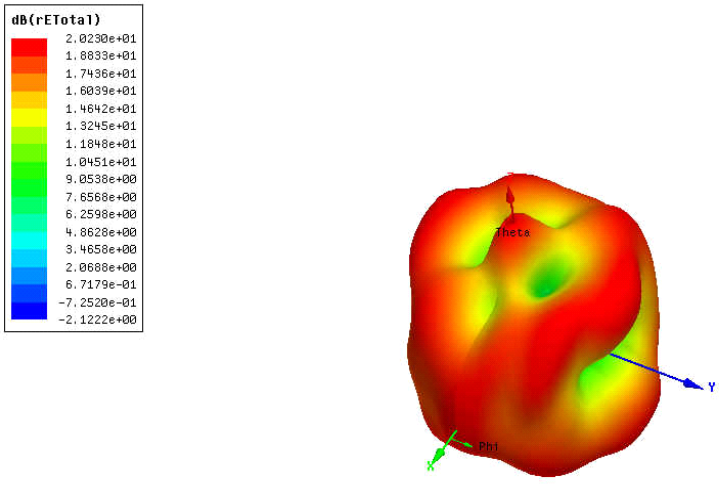

Figure 5.12 Total field pattern at 2 GHz for the RC-loaded bow-tie antenna

5.5 Antenna Impedances and Frequency-Domain Measurements

Theoretically, the antenna impedance can be calculated from measurements of S_{11}. Since the balun had to be used during measurements, its effects should be considered when computing the antenna impedance. This section shows the derivation to calculate antenna input impedance from the measured S_{11}.

One assumption made here is that each section's impedance of the balun has exactly the same value as designed. It is also assumed that there is no loss along the CPW/CPS transmission lines and the impact of soldering is neglected. The transmission line model of antenna's S_{11} parameters measurement can then be illustrated in Fig. 5.13:

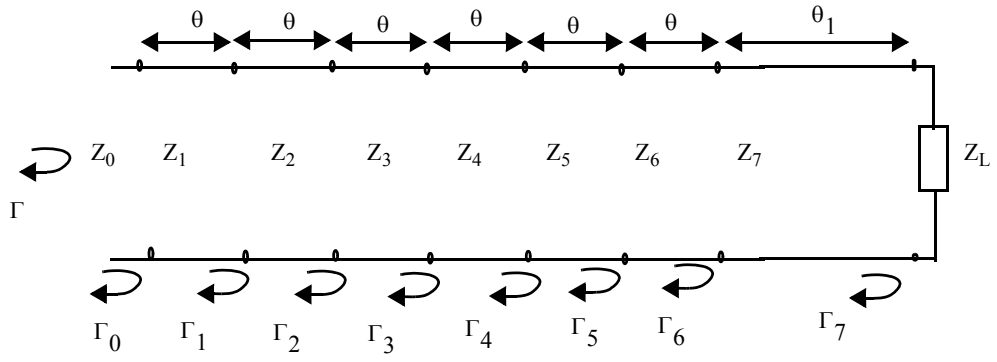

Figure 5.13 Transmission line model for antenna impedance calculation

The model includes each section of the balun and their associated lengths. As shown above, Z_0 is the coax cable characteristic impedance, Z_1 to Z_6 the characteristic impedance of each CPW section, Z_7 the characteristic impedance of the CPS section and Z_L the antenna impedance. θ is the

electrical length of each CPW section and θ_1 is the electrical length of the CPS section. From equation (4.17) and (4.18), we write the reflection coefficient at each junction and the total reflection as

$$\Gamma_n = \frac{Z_{n+1} - Z_n}{Z_{n+1} + Z_n}, \text{ for } n = 0,1,2,\ldots,6 \text{ and } \Gamma_7 = \frac{Z_L - Z_7}{Z_L + Z_7} \quad , \tag{5.5}$$

$$\Gamma = \Gamma_0 + \Gamma_1 e^{-j2\theta} + \Gamma_2 e^{-j4\theta} + \Gamma_3 e^{-j6\theta} + \Gamma_4 e^{-j8\theta} + \Gamma_5 e^{-j10\theta} + \Gamma_6 e^{-j12\theta} + \Gamma_7 e^{-j(12\theta + 2\theta_1)}. \tag{5.6}$$

The antenna input impedance Z_L can be calculated from (5.6) through

$$\Gamma_7 = -e^{j(12\theta + 2\theta_1)}[\Gamma_0 + \Gamma_1 e^{-j2\theta} + \Gamma_2 e^{-j4\theta} + \Gamma_3 e^{-j6\theta} + \Gamma_4 e^{-j8\theta} + \Gamma_5 e^{-j10\theta} + \Gamma_6 e^{-j12\theta} - \Gamma] \tag{5.7}$$

with

$$\Gamma = S_{11}. \tag{5.8}$$

S_{11} measurements were taken according to the same situations for time domain waveform measurements so that some predictions could be made from the frequency domain measurements. With the designed $l_{fs} = 40$ *mm*, it is desired that the bow-tie antenna will be able to transmit the impulse with $f_c = 1.1$ GHz most efficiently. It is beneficial to experimentally find out the best l_{fs} at the vicinity of 40 *mm*. But, because of the conflict between obtaining a lower l_{fs} value while keeping the bow-tie radius (275 *mm*) constant, only situations for $l_{fs} > 40$ *mm* were investigated by short-circuiting the adjacent slots. This procedure was accomplished in the next chapter

where there will be three short-circuited slots one after another to change l_{fs} for investigating the RC-loading effects. We take the same steps for frequency-domain measurements in this chapter.

5.5.1 Whole-body antenna

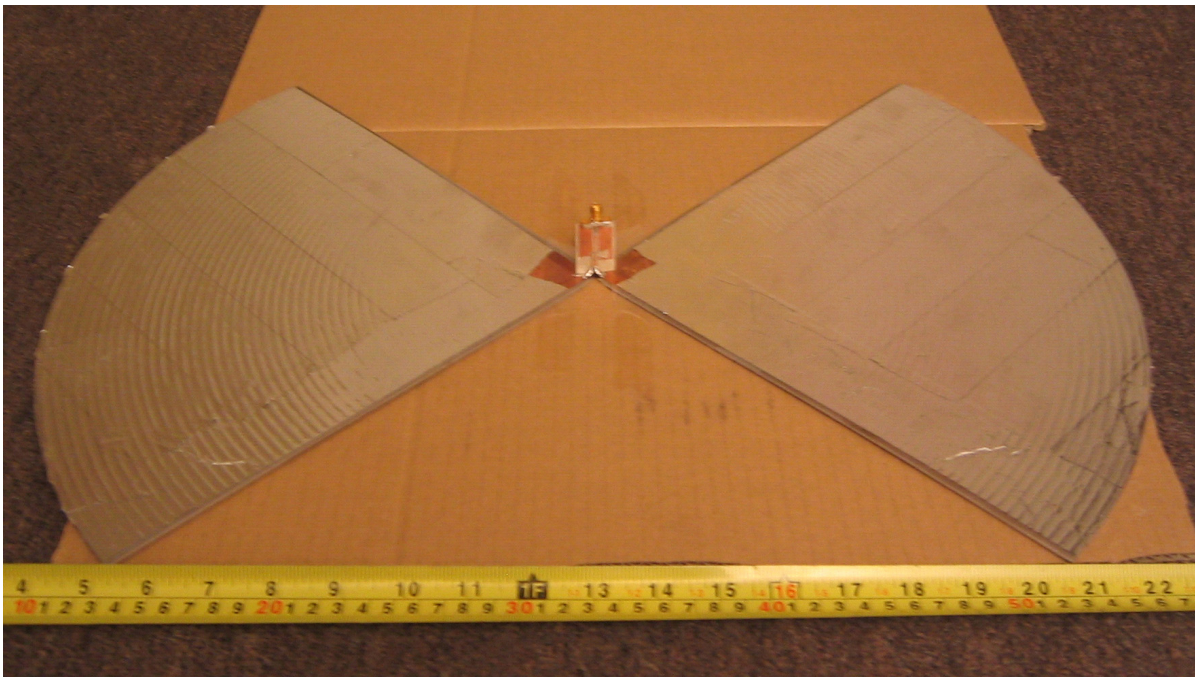

Figure 5.14 The whole-body antenna

As shown above, by short-circuiting all the slots, a 275 *mm*-radius bow-tie was constructed and tested by an Anritsu 360 network analyzer. An interesting phenomena was found that by putting microwave absorbers above the antenna, the S_{11} parameters were changed noticeably for 120Ω and 100Ω balun cases but did not change much for 80Ω balun cases. Considering the large area of the antenna surface and the similar large volume of the absorbers, the absorbers were actually acting as some kind of loads, changing S_{11} at some frequencies for 100Ω and 120Ω baluns. In next chapter, we will see that the absorbers do not affect the time-domain waveforms much for the

whole-body antenna. The reason of the different impacts of the absorbers in time-domain and frequency-domain will be discussed in Section 6.5.1 on page 84. The S_{11} measurements of the whole-body bow-tie without and with absorbers are shown in Fig. 5.15.

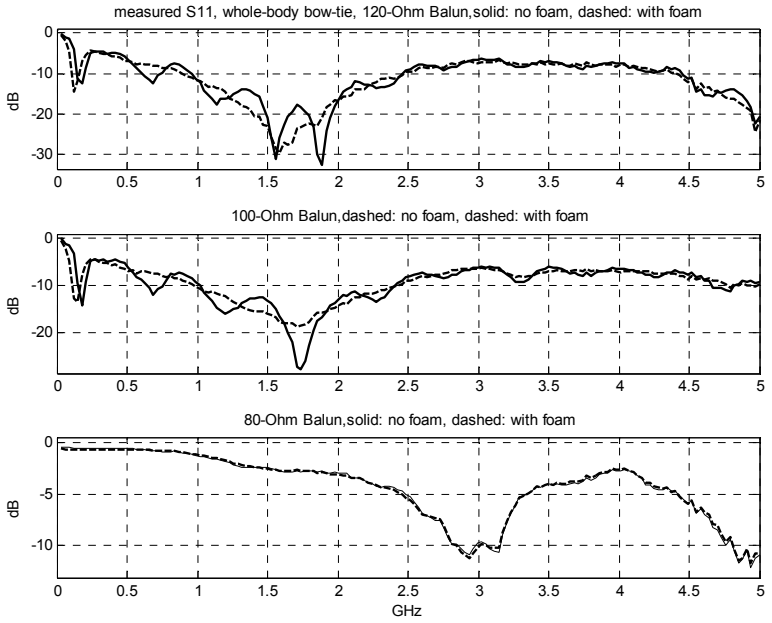

Figure 5.15 Measured S_{11} for the whole-body bow-tie

When there is no absorbers applied, it is seen that the lowest S_{11} happens for the 120Ω balun and it becomes worse for 80Ω balun case, where the S_{11} value is only -2.7 dB at 1.55 GHz, about 28 dB higher than the 120Ω case. Furthermore, it is noticed that the lowest S_{11} is -30 dB at 1.8 GHz for 120Ω balun and -28 dB at 1.7 GHz for 100Ω balun respectively, but these valleys are all located at frequencies above 1.5 GHz. Recalling that the center frequency of our monocycle is 1.1 GHz where the S_{11} values are around -10 dB for both the 120Ω and 100Ω cases, it means that the whole-body antenna is probably not suitable for the monocycle radiation. Since S_{11} measure-

ments for the 80Ω balun are not good and the absorber application does not affect S_{11} parameters, implying a severe impedance mismatch between the balun and the antenna, the results where the 80Ω balun was used are not considered for the following antenna impedance computation.

From equations (5.5) and (5.7), the whole-body antenna input impedance is calculated and shown in Fig. 5.16 and the averaged impedances for no-foam (resistive load) and foam (RC-load) cases are shown in Fig. 5.17. The resistance appears lower than the simulation results in Fig. 5.8 on page 64 and Fig. 5.10 on page 65.

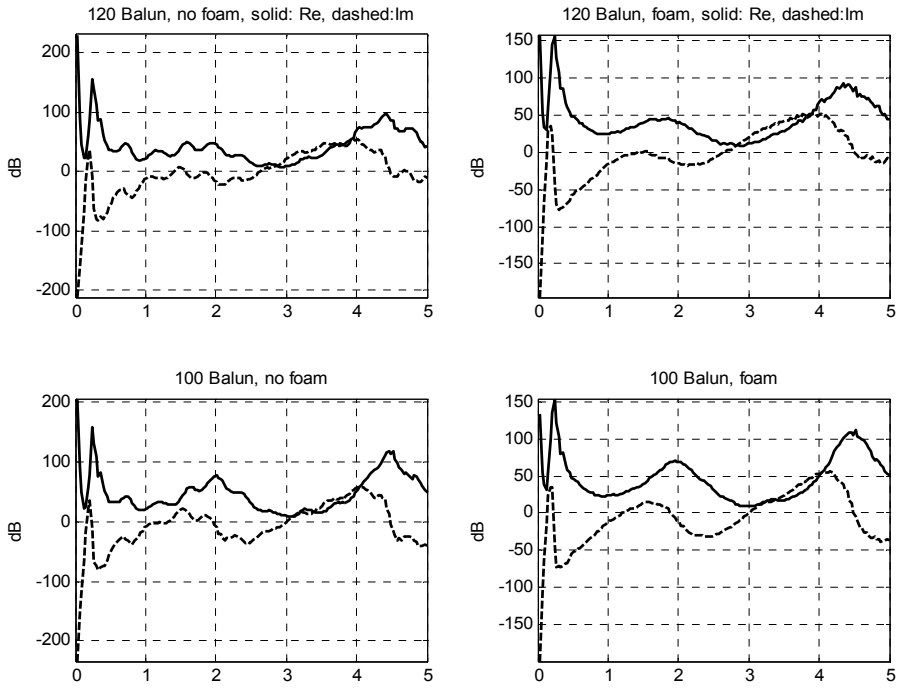

Figure 5.16 Computed whole-body antenna impedances

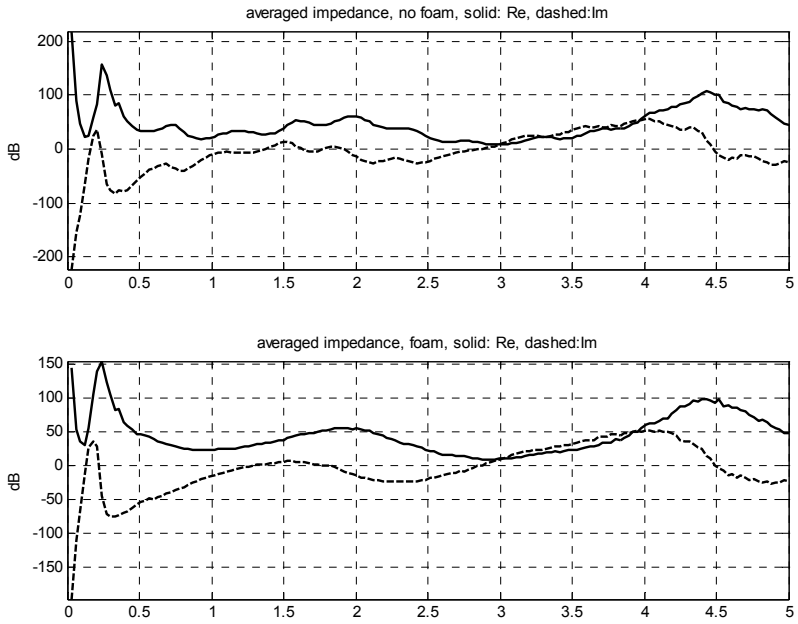

Figure 5.17 Averaged whole-body antenna input impedances

5.5.2 Measurements for Different Baluns and Shorted Slots

We now evaluate the three baluns' performances in frequency-domain. We also investigate the antennas' behaviors when the first three slots are short-circuited, as is done for the time-domain waveform collections in Chapter 6. Fig. 5.18 on page 73 to Fig. 5.20 on page 75 show the S_{11} measurements of the bow-tie antenna for the three baluns. In these plots, the left columns show the cases without RC loading, the right columns are for RC loading, "short 0" means no slot shorted, "short 1" means the 1st slot shorted and so on.

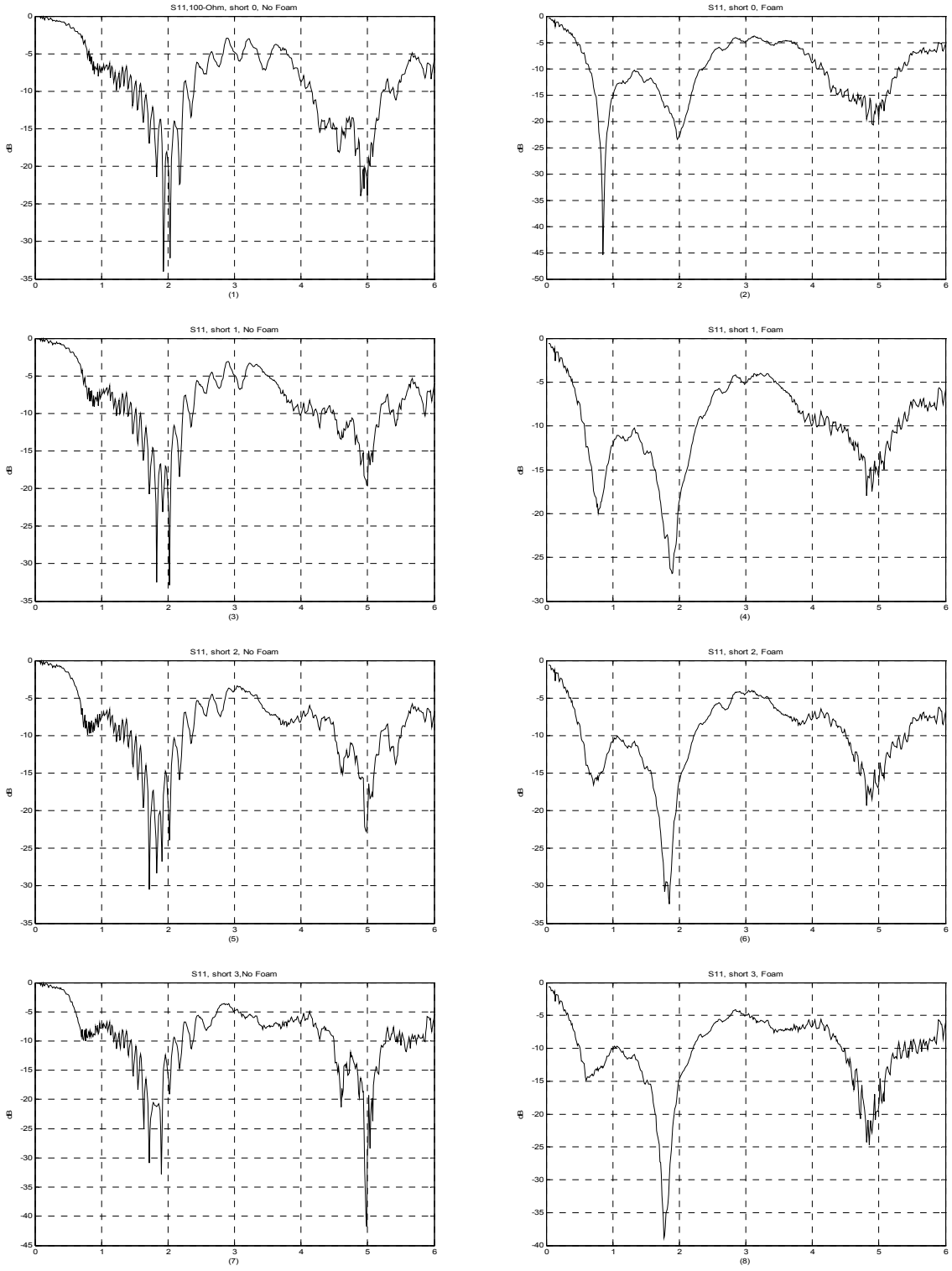

Figure 5.18 Measured S_{11} when using 120Ω balun

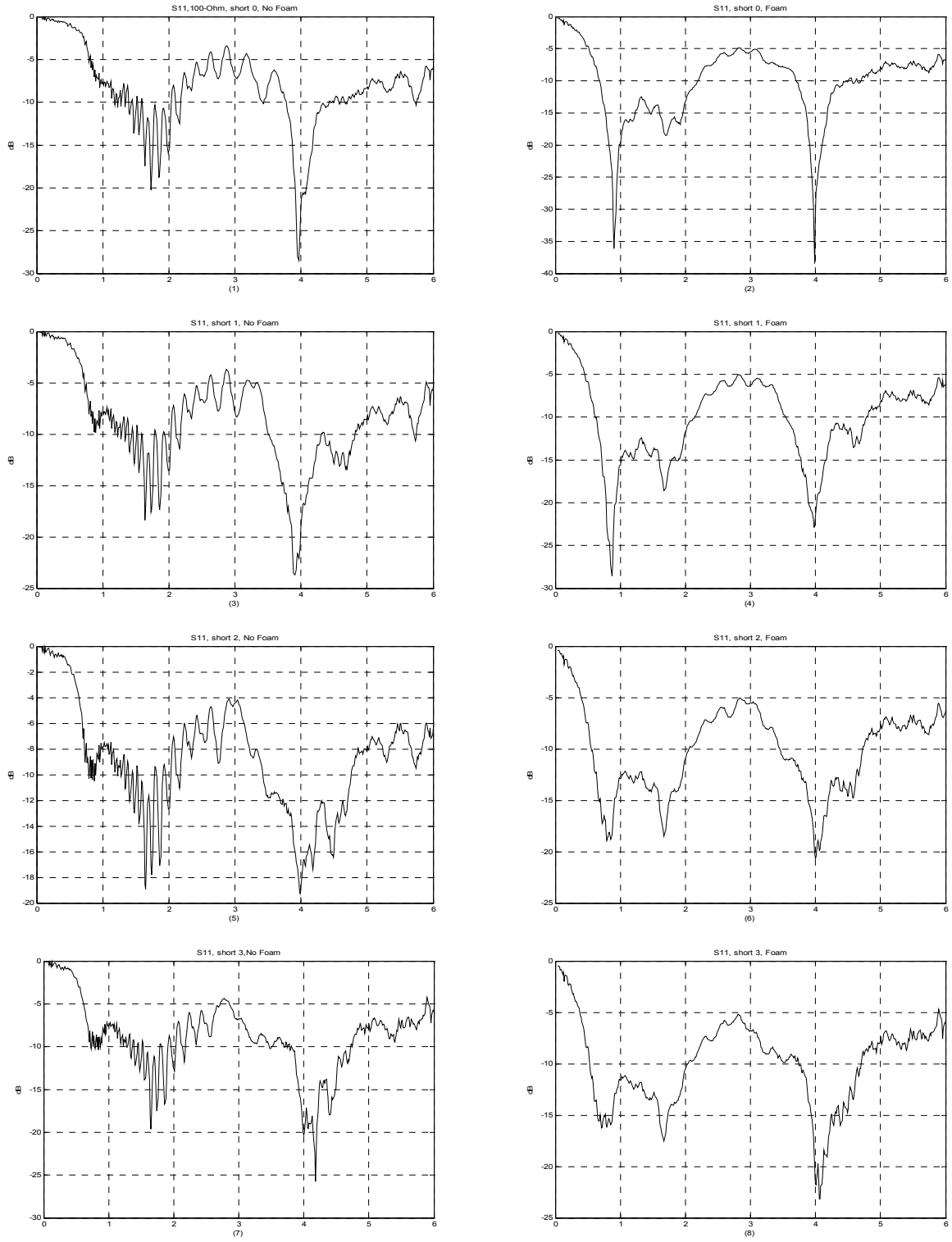

Figure 5.19 Measured S_{11} when using 100Ω balun

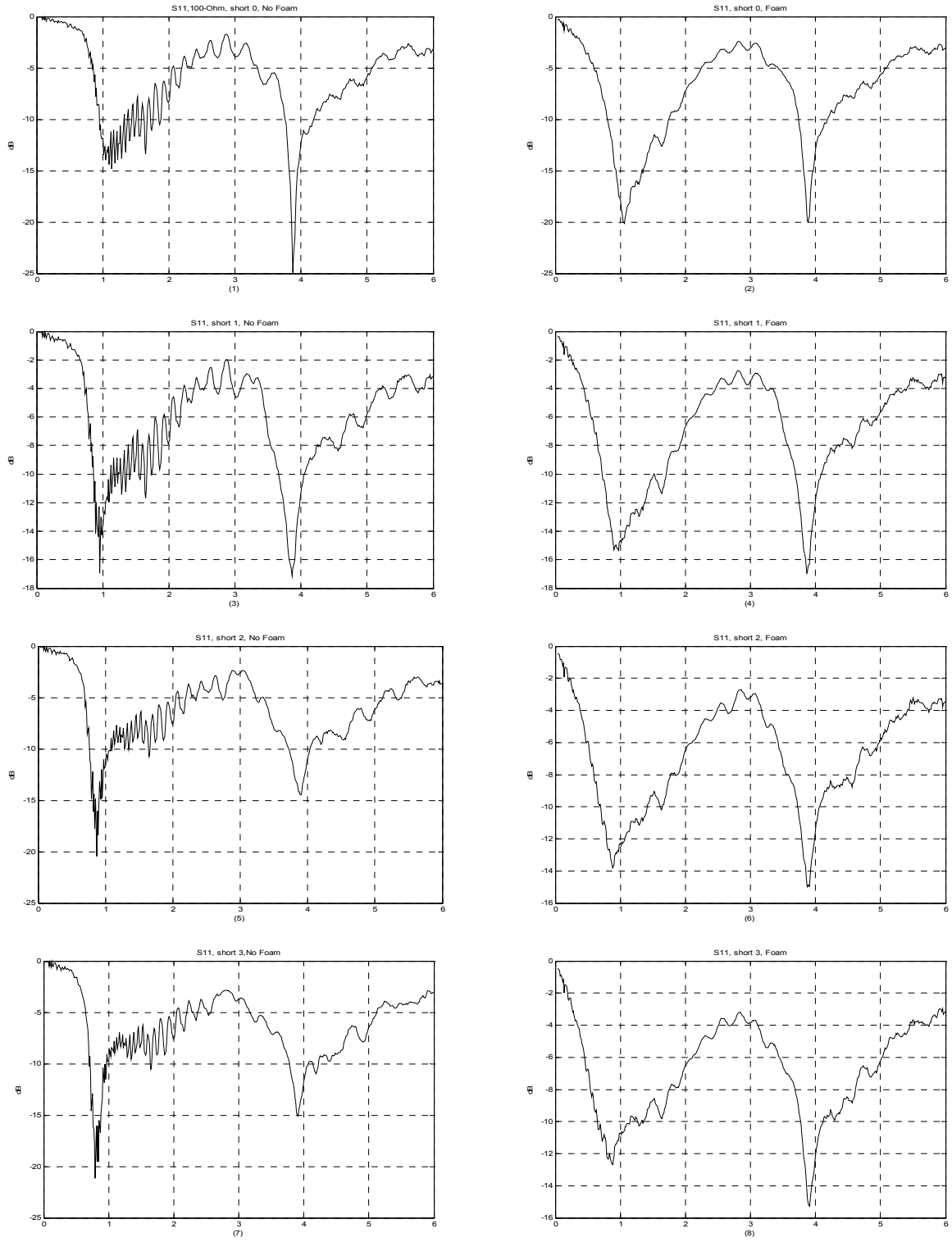

Figure 5.20 Measured S_{11} when using 80Ω balun

Comparing the cases with and without foam, it seems that S_{11} is greatly improved with valley values observed around 1 GHz by applying the resistive foam, resulting an antenna bandwidth expansion. So it is predicted that the antenna will be able to radiate the monocycle when applying the foam, though the 80Ω balun case seems not as good as the other two baluns. For this 80Ω balun case, the possible reason that its performance is inferior based on S_{11} values, is because the antenna impedance is not close to 80Ω and much of the signal is reflected at the feed point. In this case, resistive loading can not offer much improvement for expanding the bandwidth.

Observing the above measurements, it is found that the RC loading effects are small for frequencies above 3 GHz when compared with frequencies below 3 GHz cases. The reason is that the size of the antenna is designed for radiating the monocycle which has a centre frequency at 1.1 GHz, therefore it is not suitable for high frequency radiation.

From these measurements and by using equations (5.5) and (5.7), the antenna's input impedances are calculated and shown in Fig. 5.21, where the antenna input impedances have been averaged from the three baluns' results. Since the exact balun impedances are unknown, we can only conclude from this figure that the RC loading flattens the impedance near the monocycle center frequency 1.1 GHz, and does little to affect the impedances when the frequency is above 3 GHz.

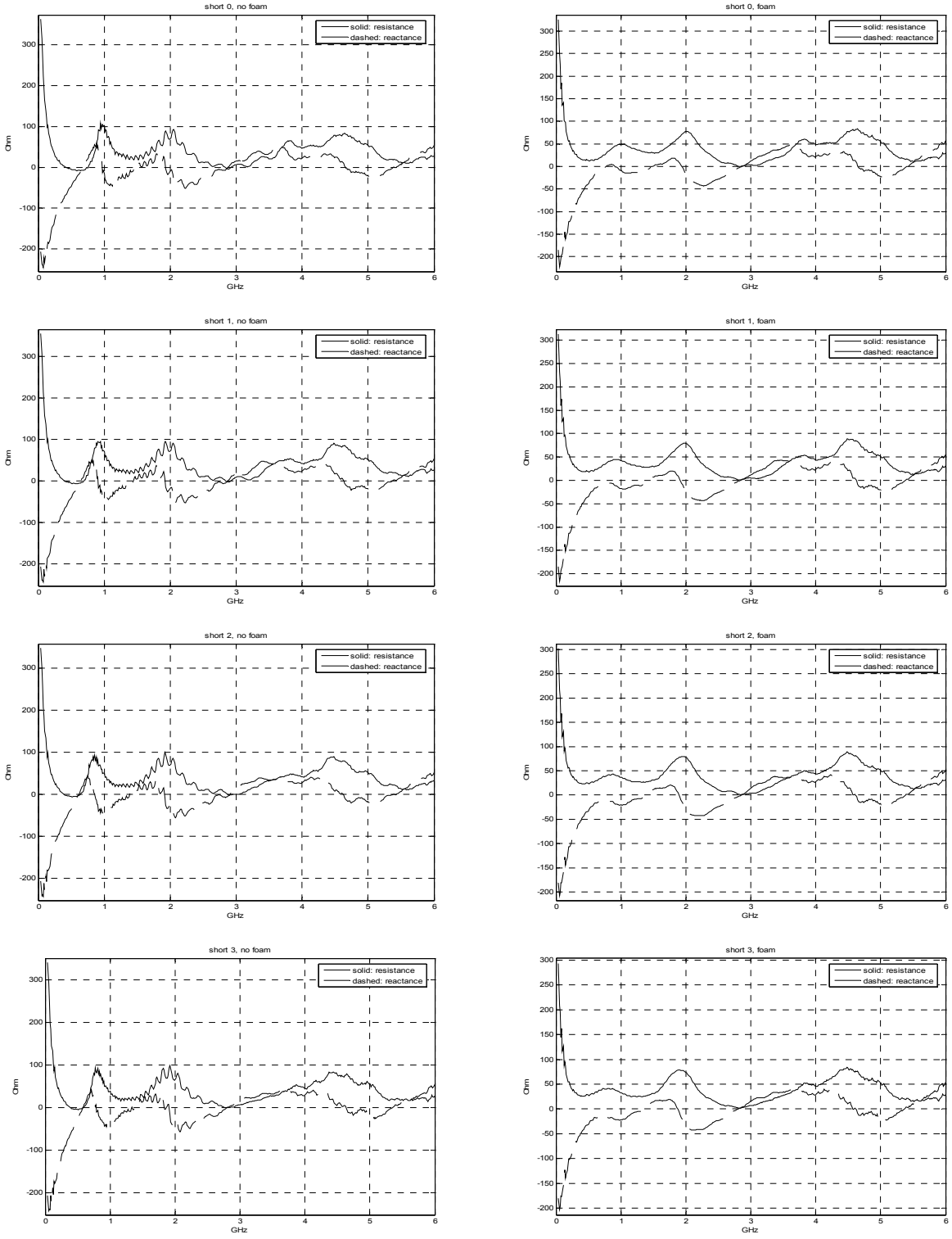

Figure 5.21 Averaged antenna input impedance. solid: resistance, dashed: reactance.

Chapter 6 Experiments and Results

This chapter discusses the experiments and results for time-domain waveform measurement. *Average radiation energy, average ringing energy*, *relative radiation efficiency* and *relative ringing efficiency* metrics are introduced for evaluating the radiation efficiency and late-time ringing. The results show that when using the RC-loaded antenna, the late-time ringing energy can be reduced to half of the capacitive loading case.

6.1 The Experimental Setup

Fig. 6.1 shows the experimental setup for the waveform measurement.

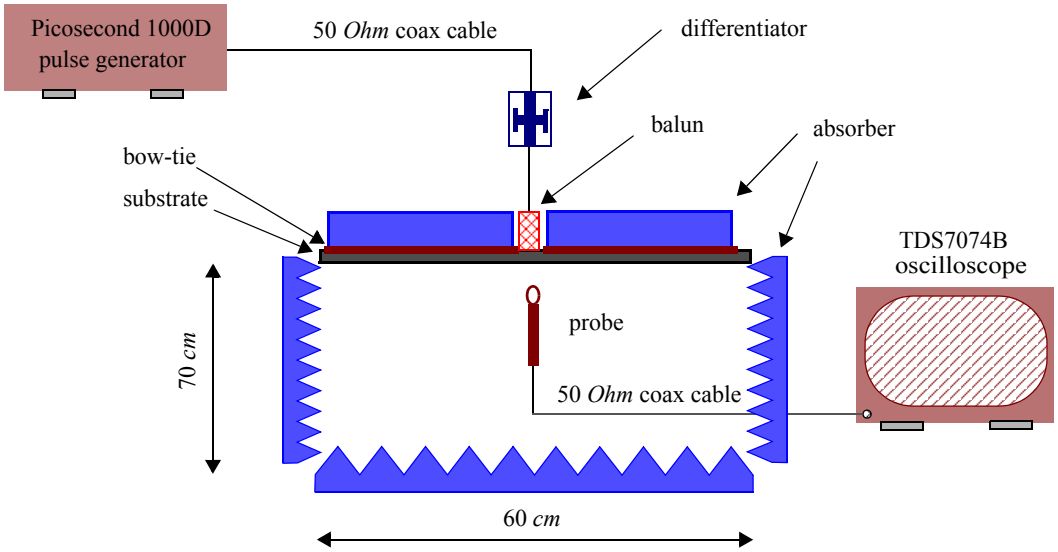

Figure 6.1 Experimental setup

As shown above, the upper side of the antennas is covered with two volumetric microwave absorbers for the resistive loading as well as for removing the unwanted electric field on the upper side of the antenna. The differentiator is inserted between the impulse generator and the balun by a 50Ω coax cable. To avoid multiple reflections from the differentiator, it was placed close to the balun so that the reflected signal is attenuated when traveling back to the impulse generator along the cable. The two CPS lines were soldered to the two antenna arms separately for antenna feeding. The probe was placed at a fixed distance of 10 *cm* under the antennas in the broadside direction and the probe needle was oriented horizontally. The collected signal was measured by a Tektronix TDS7074B Digital Phosphor Oscilloscope. Microwave absorber of size 60 *cm* by 60 *cm* at the bottom and with size of 70 *cm* by 60 *cm* at two walls of bow-tie's two end planes were used to minimize clutters from the floor and other directions. The thickness of the absorber is about 10 *cm*.

6.2 The Probe

A semi-rigid coax probe [59] was used as the sensor to measure the waveform transmitted from the antennas. Its shape and dimension are illustrated in Fig. 6.2.

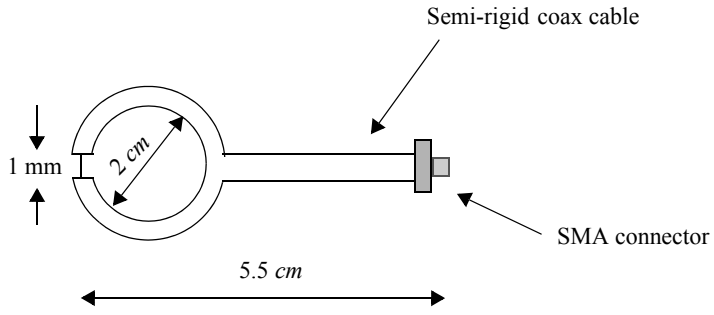

Figure 6.2 The probe used for measurement

The probe is made from 50Ω semi-rigid coax cable to measure the electric field intensity at the the broadside direction of the bow-tie antennas. This circular probe has a similar configuration as suggested in [60][61] but the length of the needle is 1 *mm*, double the length of the probe in [60][61]. This extra needle length degrades the sensitivity of the probe. For our experimental setup, the probe can only detect waveforms 10 *cm* away from the antenna while the sensor [61] used in [22] was put 25 *cm* away. Though the probe was not specifically designed and calibrated as a time domain measurement sensor as suggested in [61] and [62], it provides a practical way to detect the radiated impulse signal at the laboratory level. The problems of designing, fabricating and calibrating a more accurate and sensitive time domain probe are not considered in the thesis.

6.3 Average Ringing Energy and Radiation Efficiency

In [22], peak voltage values of the transmitted waveforms are used for evaluating the RC-loading scheme. Because of the low sensitivity of our probe, it will later be shown that this method is not practical for the system under consideration. Alternatively, from an energy point of view, we are still able to provide a performance metric by defining two parameters: *average ringing energy* and *radiation efficiency*, which can fully describe the performance of the impulse system.

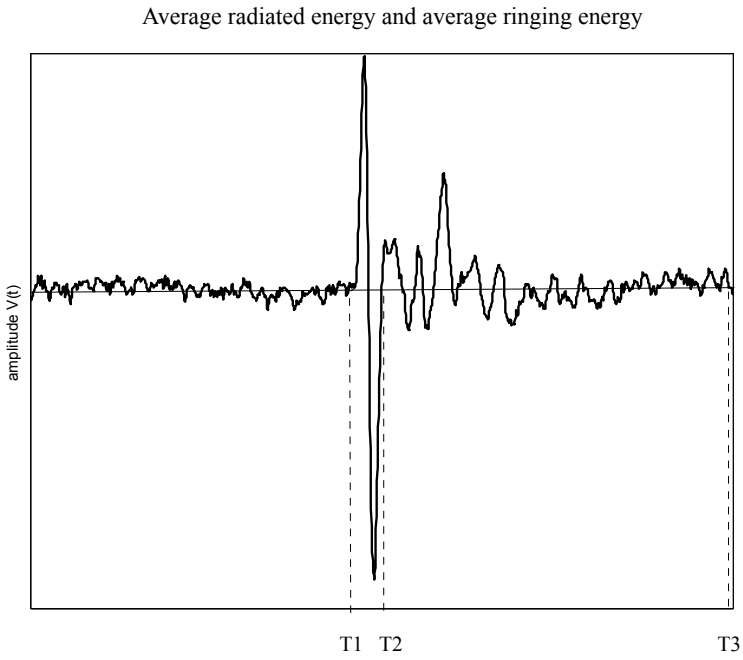

Figure 6.3 Average radiated energy and average ringing energy definitions

As an example to show the definition of average radiated energy and average ringing energy, Fig. 6.3 shows the time domain waveform response for a monocycle signal from a vavaldi antenna [6]. The radiated monocycle duration is from time T_1 to time T_2, the late-time ringing occurs from time T_2 to time T_3. Quantitatively defining *average ringing energy* as

$$E_{ringing} = \sqrt{\frac{1}{T_3 - T_2}\int_{T_2}^{T_3} |V(t)|^2 dt} \quad , \tag{6.1}$$

where T_2 is the late-time ringing starting time, T_3 is the late-time ringing stopping time and $V(t)$ is the measured signal voltage at time *t*, we are able to determine how severe the late-time ringing is during time interval T_2 to T_3. The larger $E_{ringing}$ is, the worse the ringing effect. By compar-

ing $E_{ringing}$ values for cases with and without the volumetric absober used for antenna loading, a quick conclusion can be made for the effectiveness of the RC-loading method.

Similarly, to evaluate the radiated impulse energy, the *average radiated energy* can be calculated as

$$E_r = \sqrt{\frac{1}{T_2 - T_1}\int_{T_1}^{T_2} |V(t)|^2 dt} = \sqrt{\frac{1}{T}\int_{T_1}^{T_2} |V(t)|^2 dt}\ , \tag{6.2}$$

where T_1 is the impulse starting time, T_2 is the impulse stop time, $T = T_2 - T_1$ is the impulse period and $V(t)$ is voltage amplitude, same as in (6.1). Equation (6.2) can also be used for the impulse to find out its energy E. The *radiation efficiency* η is then obtained as

$$\eta = E_r / E. \tag{6.3}$$

Since the impulse energy E is a constant, E_r can be used as a representative of η. To compare the situations without absorbers and with absorbers, we can practically define the *relative radiation efficiency* $\xi^{radiation}$ as

$$\xi^{radiation} = \frac{E_r^{RC}}{E_r^{C}}\ , \tag{6.4}$$

where E_r^{RC} is the average radiated energy for RC load and E_r^{C} is the average radiated energy for capacitive loading. The higher $\xi^{radiation}$ is, the better radiation efficiency for RC-loading. This same idea can also be used for estimating the ringing energy by defining *relative ringing efficiency* $\xi^{ringing}$ as

$$\xi^{ringing} = \frac{E_{ringing}^{RC}}{E_{ringing}^{C}} , \tag{6.5}$$

where $E_{ringing}^{RC}$ is the average ringing energy when applying RC load and $E_{ringing}^{C}$ is the average ringing energy for capacitive load.

6.4 Relative Monocycle Energy

Analysis of Fig. 3.8 on page 29 suggests that the length of the monocycle is 1.2 *ns*, starting from 4.4 *ns* and ending at 5.6 *ns*. Since all the measurements are taken under the same circumstance (same cable length, same differentiator and same probe, *etc.*), the measurement unit and the constant part of equations (6.1) and (6.2) can be neglected for our comparison purposes. For radiation efficiency η calculation, we have the *relative monocycle energy*

$$E = \sqrt{\int_{4.4ns}^{5.6ns} |V(t)|^2 dt} = 0.4846 . \tag{6.6}$$

Actually, if we expand the integral limits from 4.0 *ns* to 7.0 *ns* for this monocycle signal shown in Fig. 3.8 on page 29, *i.e.*, considering the energy on a 3 *ns* interval (quite a long time for an impulse), we obtain 0.4869, a 0.47% difference compared with 0.4846. This indirectly verifies that the main monocycle energy is within the interval of 4.4 *ns* to 5.6 *ns*, *i.e.*, the monocycle duration is 1.2 *ns*.

6.5 Results

6.5.1 Whole-body Antenna

By using metallic tape to short-circuit all the slots, a whole-body bow-tie antenna was made (Fig. 5.14 on page 69) and the radiated waveforms were measured for the three baluns by putting the probe 10 cm away from the antenna in the broadside direction. Fig. 6.4 shows the measured waveforms without and with foam.

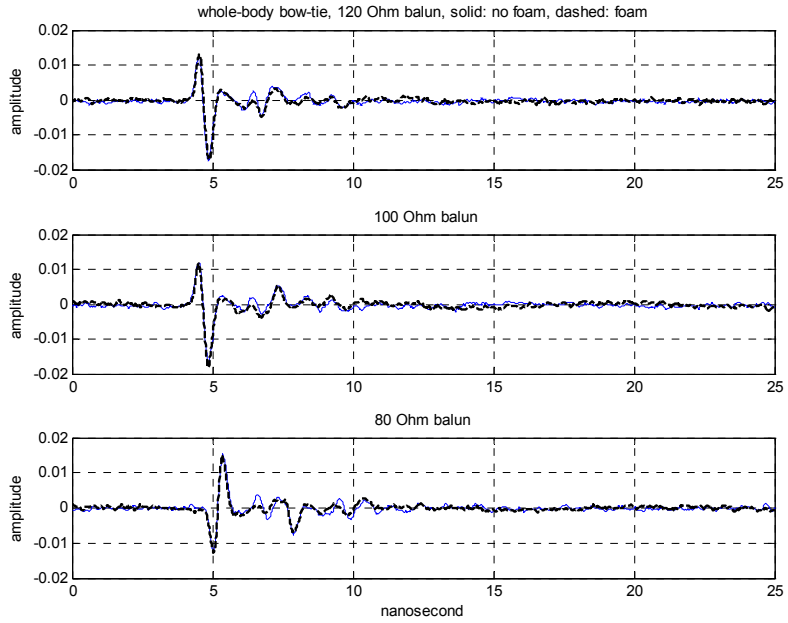

Figure 6.4 Waveforms measured for the whole-body bow-tie

It is observed that the waveform amplitudes are small, about half the amplitudes of measurements in next section. It is also seen that the amplitudes are at a same level for three different baluns, which have a large characteristic impedance difference up to 40Ω. Based on these observations, one reasonable explanation is that all the three baluns are not able to provide a good impedance match to the whole-body antenna for the monocycle (*i.e.*, monocycle's frequency components). As mentioned in the previous chapter, the time-domain waveform amplitudes do not change for both foam and no-foam cases, very different from frequency domain observations, where the application of foam apparently changes S_{11} measurements for the 120Ω and 100Ω balun cases. Referring to the measurement results in Fig. 5.15 on page 70, the foam seems to be playing a role of changing S_{11} when the frequency is above 1.7 GHz. But for our monocycle, the peak amplitude is at 1.1 GHz and the amplitudes of those frequency components higher than 1.7 GHz are

less than half of the peak amplitude (Fig. 3.8 on page 29). Thus, the foam's impact to the monocycle radiation for the whole-body antenna is not noticeable.

However, the late-time ringing from the above figures is prominent and we can investigate them quantitatively. In the following discussion for this whole-body bow-tie, the 80Ω balun results are not considered because its impedance mismatch seems too severe, as concluded on page 70 from the previous chapter.

From equations (6.1), (6.2) and (6.5), the average ringing energy, average radiated energy and the relative ringing efficiency are calculated as

$$E_{ringing}^{120} = 0.0677 \ , \ E_r^{120} = 0.0981 \ \text{ with } \ \xi_{120}^{ringing} = \frac{E_{ringing}^{120}}{E_r^{120}} = 67.99 \ \%, \qquad (6.7)$$

and

$$E_{ringing}^{100} = 0.0522 \ , \ E_r^{100} = 0.0947 \ \text{ with } \ \xi_{100}^{ringing} = \frac{E_{ringing}^{100}}{E_r^{100}} = 55.05 \ \%, \qquad (6.8)$$

where the integral range for the average ringing energy is from 6.21 *ns* to 25 *ns*, the average radiated energy integral is from 5.01 *ns* to 6.2 *ns*. The relative ringing efficiencies $\xi_{100}^{ringing}$ and $\xi_{120}^{ringing}$ are high because there is no load applied. Further, the radiation efficiencies are computed as

$$\eta_{whole}^{100} = \frac{E_r^{100}}{E} = 19.54\ \%\ \text{and}\ \ \eta_{whole}^{120} = \frac{E_r^{120}}{E} = 20.24\ \%. \tag{6.9}$$

The results show that the radiation efficiencies are quite low for the whole-body antenna. The reasons behind the low radiation efficiency are: 1) the size of the whole-body antenna is not suitable for radiating the monocycle peak amplitude located at 1.1 GHz; 2) the impact introduced by using the metallic tape over the slots is unknown because the total slot area is comparable with the strip area in this case; 3) impedance mismatches due to the unknown antenna impedances for this whole-body antenna case. However, the above measurements show that the late-time ringing is very large and the radiation efficiencies are low when there is no antenna loading.

6.5.2 Capacitively Loaded and RC-loaded Antenna

By short-circuiting the first three slots to change the first slot distance l_{fs}, the late-time ringing was investigated. Fig. 6.5 to Fig. 6.7 show the results for different baluns and different l_{fs}. In these figures, the first columns of the plots show the cases without resistive loading (*i.e.*, capacitive loading) and the second columns show the microwave absorber foam cases (RC-loading). The unit for the time axis is in nanoseconds.

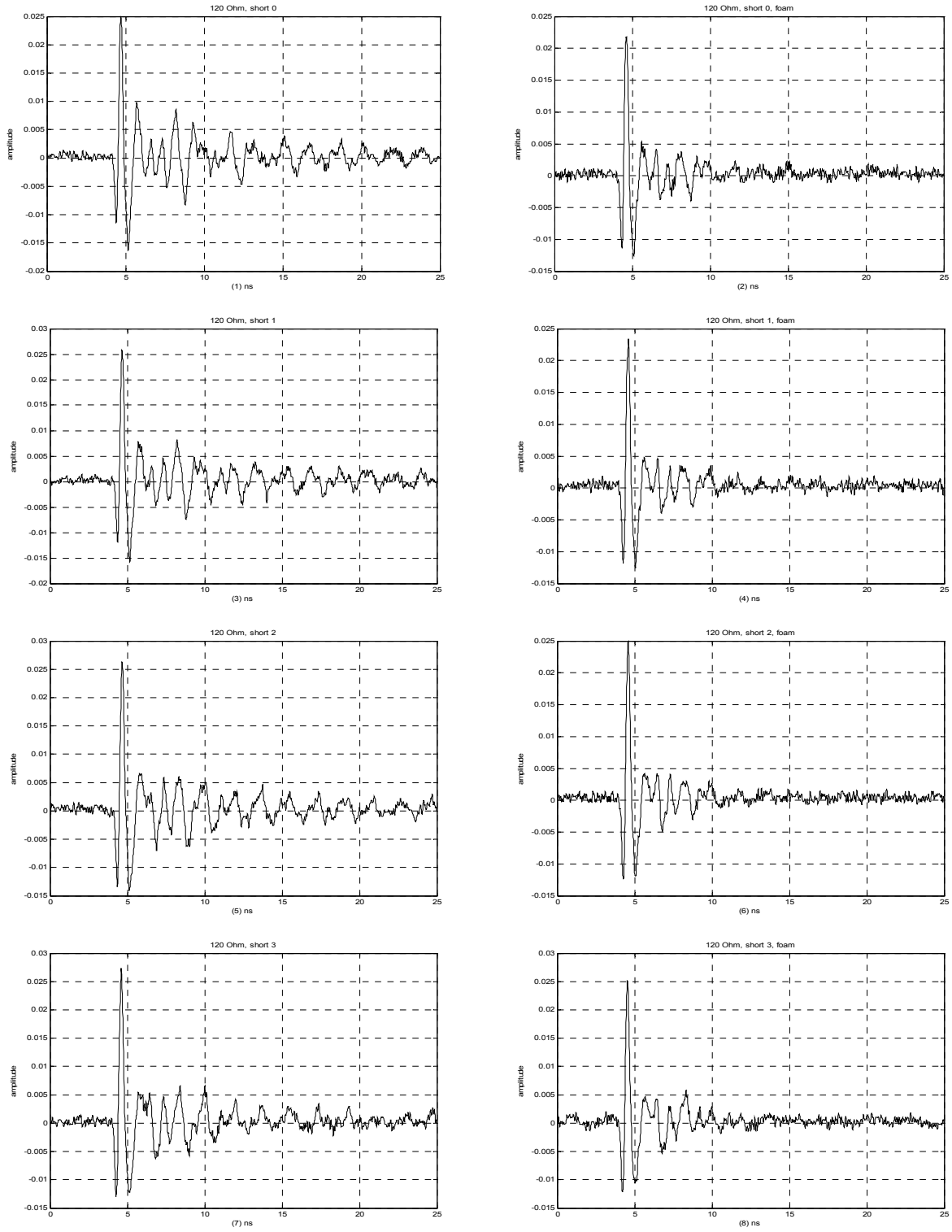

Figure 6.5 Test results for 120Ω balun

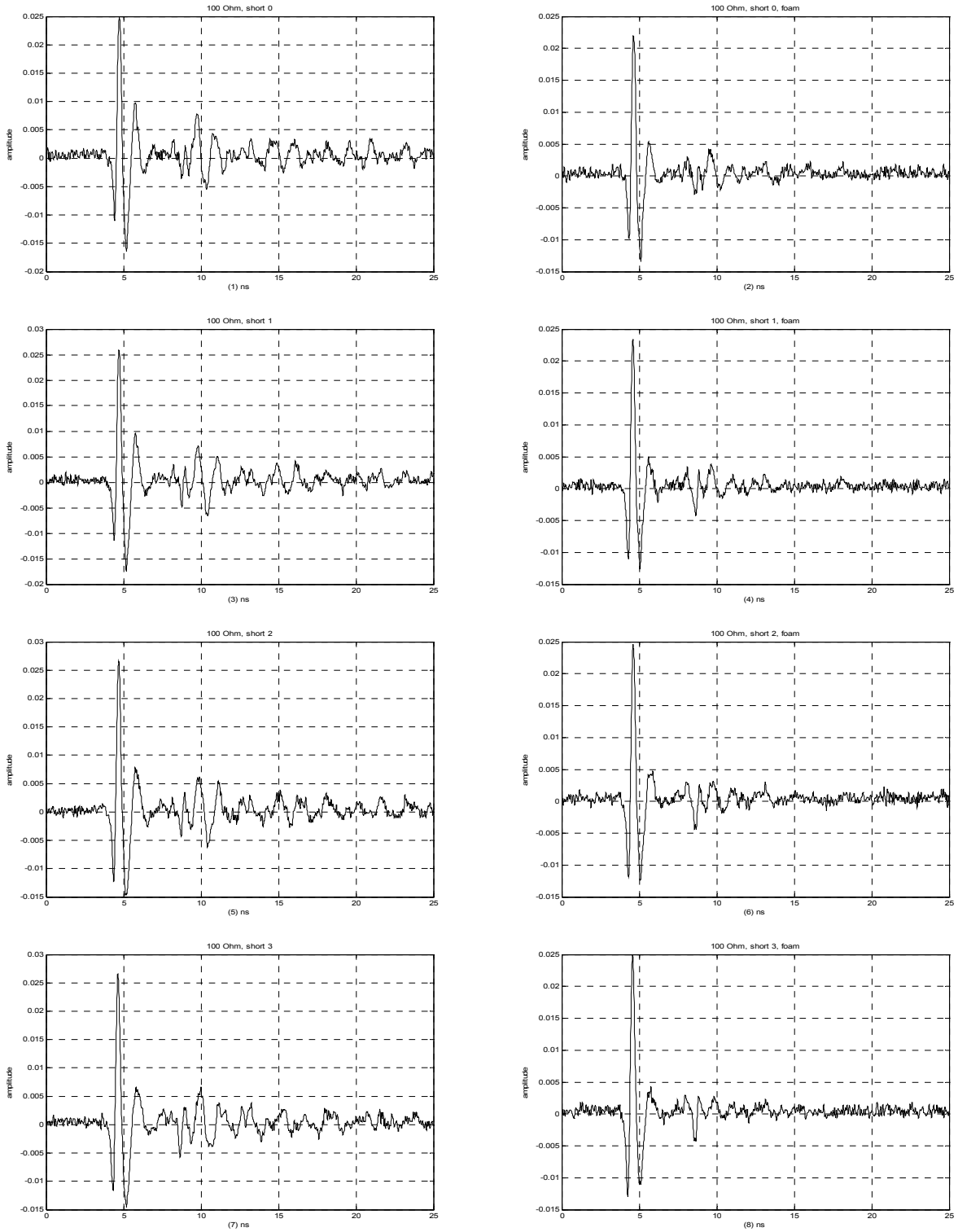

Figure 6.6 Test results for 100Ω balun

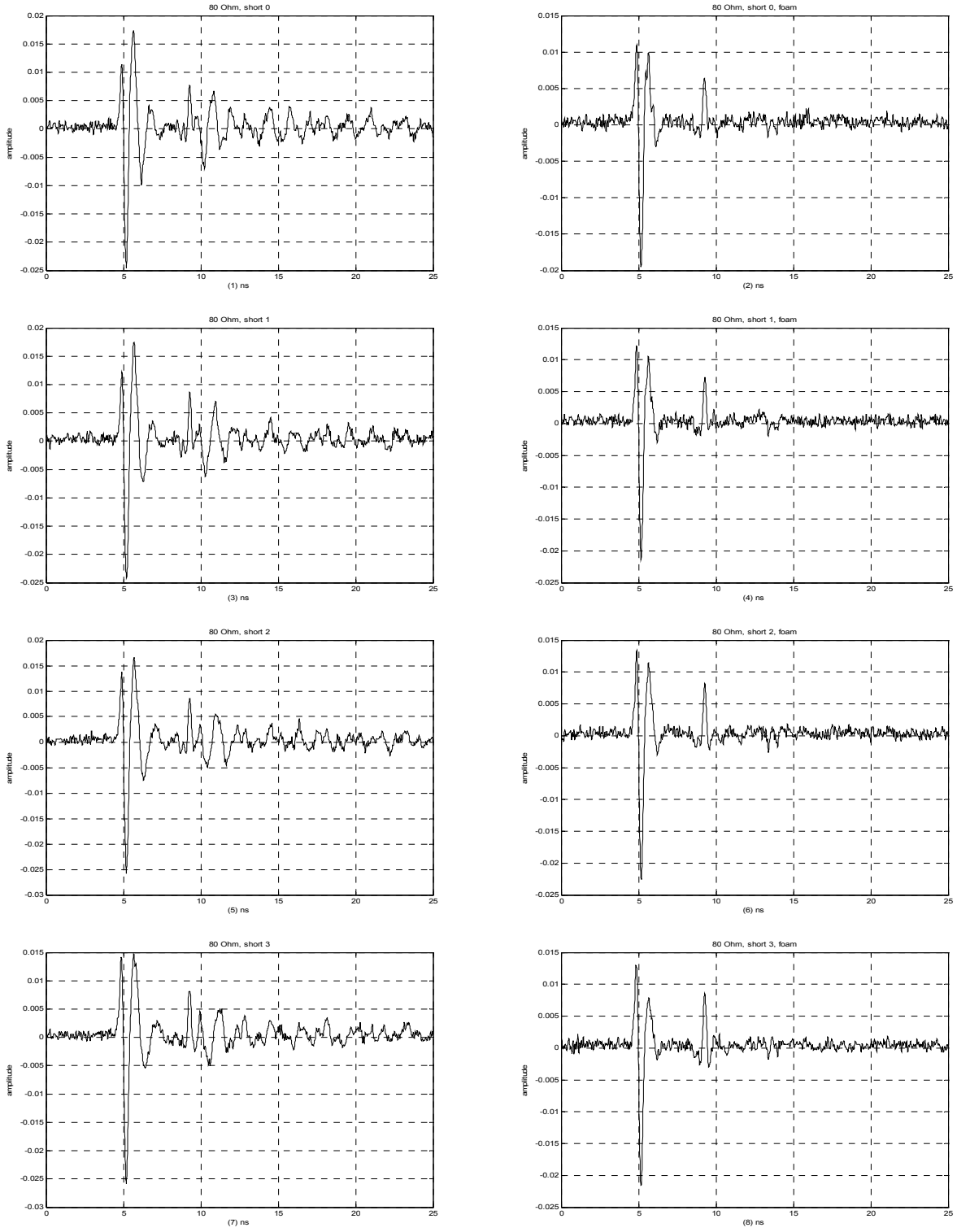

Figure 6.7 Test results for 80Ω balun

From the above results, it seems that the resistive loading does reduce the late-time ringing. But we require more quantitative calculations to find out the details.

6.5.3 Comparisons and Results

First, the maximum voltage amplitude detected by the probe is investigated, as shown in Fig. 6.8. In each subplot of this figure, there are four groups of data corresponding to four short-circuiting cases, shown on the *x*-axis as cases 1 & 2 (no short-circuiting), cases 3 & 4 (1st slot shorted), cases 5 & 6 (2nd slot shorted) and cases 7 & 8 (3rd slot shorted). The odd numbers mean no-foam cases and even numbers are for foam cases. Case 1 and 2 along the *x*-axis correspond to non-short-circuiting for no-foam and foam respectively. Case 3 and 4 indicate that the 1st slot is shorted for no-foam and foam cases, and so on. This case numbering details are shown in Table 6.1.

Table 6.1: Cases numbering

Shorted Slots	Case Number	Description
0	1	No slot shorted, no foam
	2	No slot shorted, foam
1	3	1st slot shorted, no foam
	4	1st slot shorted, foam
2	5	1st and 2nd slot shorted, no foam
	6	1st and 2nd slot shorted, foam
3	7	1st to 3rd slot shorted, no foam
	8	1st to 3rd slot shorted, foam

In Fig. 6.8, the maximum voltages are plotted against the case numbers. It is seen that the voltage variation range is very small, suggesting that the peak voltage amplitude may not be a good indicator to evaluate the resistive loading effect because of the probe's sensitivity. Based on this figure, it is concluded that peak waveform voltage is not a suitable evaluation method for us to use.

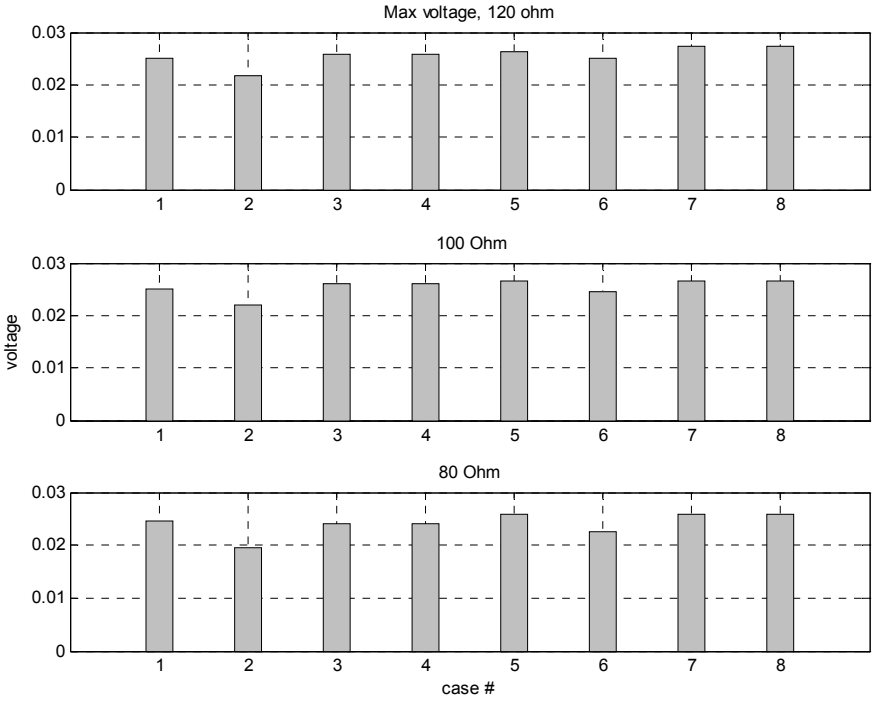

Figure 6.8 Maximum voltage of the waveforms

Average radiated energy and average ringing energy are then calculated according to equations (6.1) and (6.2) for each case and plotted in Fig. 6.9, where the same case numbering as in Fig. 6.8 is used. In the calculations, the impulse response duration is taken from 4.2 *ns* to 5.4 *ns* and the integral ranges for the late-time ringing is chosen from 5.41 *ns* to 20 *ns*. The figure clearly shows that when the absober are used, the average radiated energy and average ringing energy are, in general, decreased due to the resistive load. Recalling that we have doubt that the 80Ω balun is not able to provide a good impedance match based on the frequency-domain measurements in the

previous chapter, average radiated energy and average ringing energy for this balun are calculated but not used for comparison.

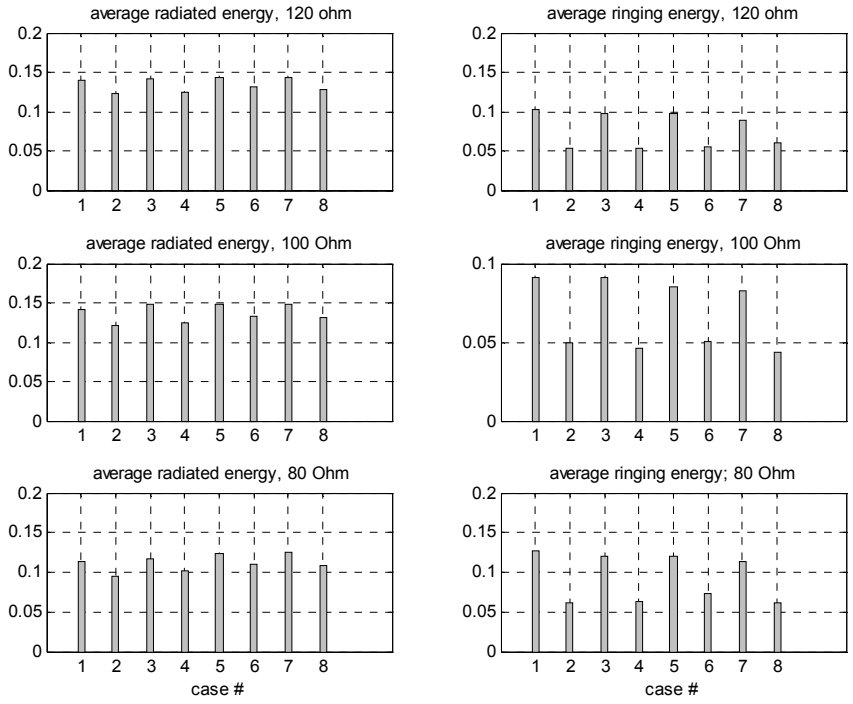

Figure 6.9 Average radiated energy and average ringing energy

Combining all the RC-loading cases from Fig. 6.9, we get Fig. 6.10 to show the average radiated energy and average ringing energy again for comparison. It is seen that though the two metrics' valuse are very close for 100Ω balun and 120Ω balun cases, it is concluded that the biggest average energy radiation case is for using 100Ω balun with two slots shorted and the minimum average ringing energy happens when using 100Ω balun with three slots shorted.

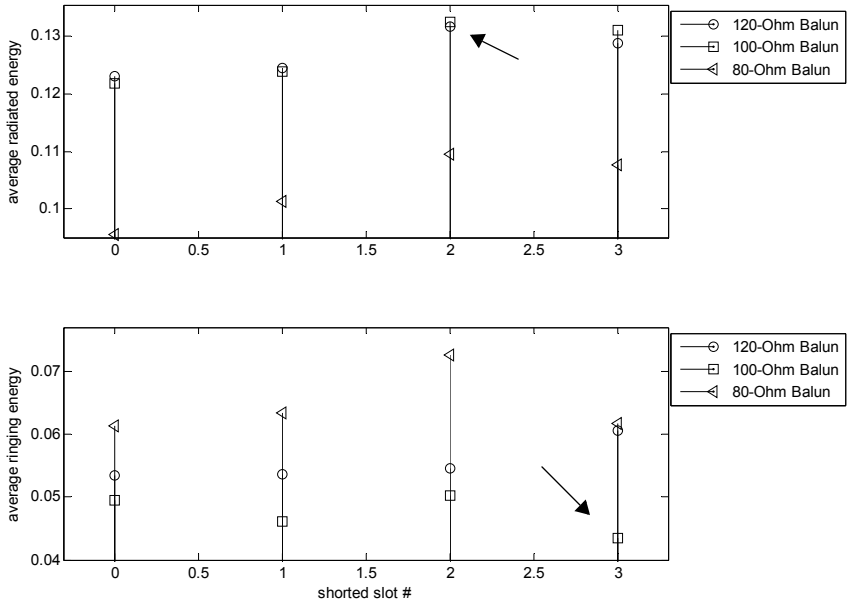

Figure 6.10 Average radiated energy and average ringing energy for foam cases

Relative radiation efficiency $\xi^{radiation}$ and relative ringing efficiency $\xi^{ringing}$ are calculated and plotted in Fig. 6.11. For $\xi^{radiation}$, the biggest value is 91.7% which corresponds to the case of 120Ω balun with two slots shorted. The minimum $\xi^{ringing} = 50.5$ % happens when using 100Ω balun with the first slot shorted, under the condition that we abandon the 80Ω balun measurements.

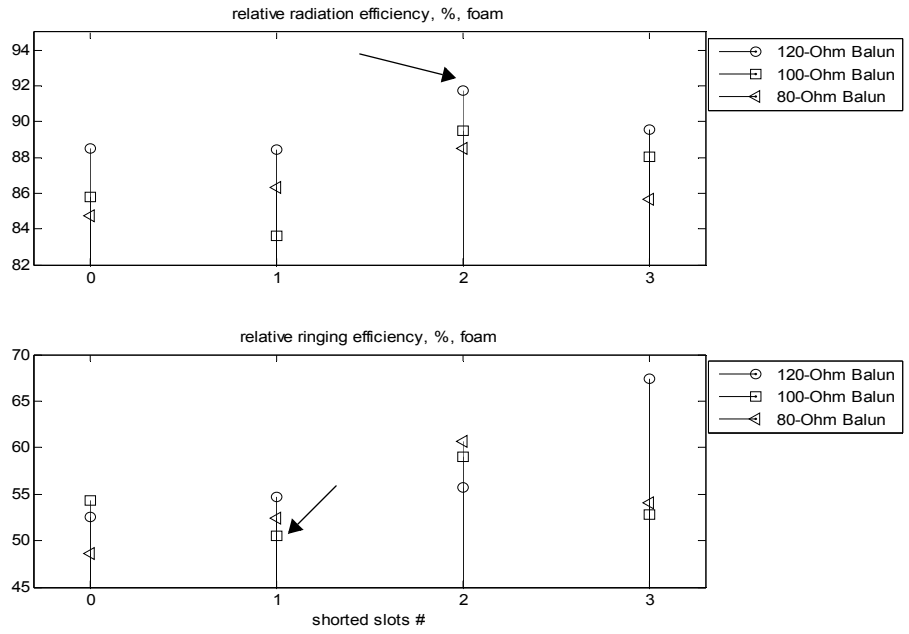

Figure 6.11 Relative radiation efficiency and relative ringing efficiency for foam cases

To summarize, all these results are tabulated in Table 6.2. In the table, the radiation efficiency η is listed by using equation (6.3) where the relative monocycle energy E is chosen as 0.4846 as shown in (6.6). From the values of η, we can see that for capacitive loading, the most efficient energy radiation $\eta_{max}^{Capacitive} = 30.7\ \%$ happens when using 100Ω balun with three slots short-circuited. It is also noticed that for RC-loading cases, the maximum value $\eta_{max}^{RC} = 27.4\,\%$ happens for using 100 balun with two slots shorted, while the energy efficiency without absorber is $\eta^{Capacitive} = 30.6\,\%$, almost the same value as $\eta_{max}^{Capacitive} = 30.7\ \%$. The decrease from $\eta^{Capacitive}$ to η_{max}^{RC} is only 3.4%, with the minimum relative ringing efficiency $\xi_{min}^{ringing} = 50.5\ \%$ and the relative radiation efficiency as high as 83.6%.

These different results are acceptable because they are based on different criteria. For example, considering very lossy soil when larger energy is needed, we may take the maximum radiated energy case. When detecting small target with weak reflections, we may have to consider the situation which corresponds to a low level of ringings. Generally, the most promising RC-loading situation from the measurements is to use 100Ω balun with the first slot distance at the vicinity of 4.5 *cm* to 5 *cm* (one to two slots shorted), where the biggest radiation efficiency η_{max}^{RC} and the lowest relative ringing efficiency $\xi_{min}^{ringing}$ can be achieved.

Table 6.2: List of results

	Shorted Slots #	120Ω Balun					100Ω Balun					80Ω Balun				
		No Foam	η (%)	Foam	η (%)	ξ (%)	No Foam	η (%)	Foam	η (%)	ξ (%)	No Foam		Foam	η (%)	ξ (%)
Radiated Energy	0	0.139	28.7	0.123	25.4	88.5	0.142	29.3	0.122	25.1	85.8	0.113	23.3	0.096	19.8	84.7
	1	0.141	29.1	0.125	25.7	88.4	0.148	30.6	0.124	25.6	83.6	0.117	24.2	0.101	20.9	86.3
	2	0.144	29.7	0.132	27.2	**91.7**	0.148	30.6	**0.133**	**27.4**	89.5	0.124	25.5	0.109	22.6	88.5
	3	0.144	29.7	0.129	26.6	88.6	0.149	**30.7**	0.131	27.0	88.1	0.126	25.9	0.108	22.2	85.4
Ringing Energy	0	0.102	-	0.053	-	52.5	0.091	-	0.049	-	54.4	0.126	-	0.061	-	48.6
	1	0.098	-	0.054	-	54.7	0.091	-	0.046	-	**50.5**	0.121	-	0.063	-	52.5
	2	0.098	-	0.055	-	55.8	0.085	-	0.050	-	59.0	0.119	-	0.073	-	60.6
	3	0.089	-	0.061	-	67.4	0.082	-	**0.043**	-	52.8	0.141		0.062	-	54.1
Max Voltage	0	0.025	-	0.022	-	-	0.025	-	0.022	-	-	0.025	-	0.019	-	-
	1	0.026	-	0.025	-	-	0.026	-	0.026	-	-	0.024	-	0.024	-	-
	2	0.026	-	0.025	-	-	0.027	-	0.025	-	-	0.026	-	0.023	-	-
	3	0.027	-	0.027	-	-	0.026	-	0.026	-	-	0.026	-	0.026	-	-

***Note 1**: Relative radiation efficiency $\xi^{radiation}$ and relative ringing efficiency $\xi^{ringing}$ are listed in the column of ξ with relative ringing efficiency $\xi^{ringing}$ underlined.

****Note 2**: The best situations according to different criteria are in bold numbers in the table.

Chapter 7 Conclusion and Future Work

An RC-loaded bow-tie antenna has been successfully designed and characterized for impulse radiation. The results of the measurements show that the selected loading scheme can greatly reduce the late-time ringing while maintaining a good radiation efficiency. From time-domain waveform results, it is concluded that this antenna has minimum late-time ringing and maximum radiation efficiency for the first slot distance l_{fs} chosen around 45 *cm* to 50 *cm* by using a 100Ω balun, *i.e*., the antenna impedance is around 100Ω for the whole bandwidth from 0.04 GHz to 3 GHz. Some systematic difficulties met while undergoing this work are listed here for future designs.

1. The balun could perform better by designing its resonant frequency at the monocycle's centre frequency by simulations. For the 80Ω balun, the measured S_{11} can reach as low as -40 dB at 1.8 GHz and it is only about -15 dB at the monocycle centre frequency 1.1 GHz. For the 100Ω balun, the lowest S_{11} is about -27 dB at 2.1 GHz and -13 dB at 1.1 GHz There is a lot space for S_{11} improvement at $f_c = 1.1\,GHz$

2. The exact balun impedance is not known. Though the balun works as expected, its exact characteristic impedance values, especially those at the transformer section, are still unknown as the balun has not been be tested separately.

3. The RC-loaded antenna input impedance *vs*. frequency has not been measured. There are two reasons for this. One is the lack of a testing procedure for a balanced feeding of the antenna for such a wide bandwidth (again, it is part of problem 1), and the other is the model of the absorber. The microwave absorber is designed to attenuate electromagnetic waves through its thickness, not at the surface. When it is used on top of the bow-tie antennas as resistant load, the currents are flowing from one strip to another through the surface of the absorber between the slots. The performance of the absorber is very important but its impact on antenna resistance can only be determined through antenna testing.

An attempt was made and then abandoned in the thesis to design a 50Ω-50Ω CPW-CPS balun without any transformer embedded so that the antenna impedance could be calculated from measured S_{11} by using this balun. The problem with this was that the conductor widths of the CPS section would be too large to fit CPS conductors within the distance between the two ground planes of CPW section, as shown in Fig. 4.5 on page 43 for the 80Ω balun case. To design a wide bandwidth balun for the purpose of measuring/computing antenna impedance is another interesting topic.

4. Although the differentiator works properly as expected, a drawback of the design is that its low S_{21} parameters. As shown in Fig. 3.5 on page 26, the measured S_{21} at 1.1 GHz is about 0.2,

which means that most of the impulse signal can not go through the differentiator. This may be a necessary consideration when developing a practical impulse GPR where the transmitted impulse power is critical.

5. A specially designed probe may be needed for more accurate waveform measurements in the future [62][63]. Calibration and the probe's influence have to be considered [61].

6. Accuracy in fabrication is important when characterizing the balun. As shown in Chapter 4, the higher CPW/CPS impedance, the more sensitive the impedances becomes to the conductor sizes. A photo-etching method could be considered when precision is critical. To the author's knowledge, this kind of CPW/CPS balun with impedance higher than 80Ω has not been reported in the literature. If antenna impedance is higher than 120Ω, some other feeding technique may be needed [22].

The list above should help when designing an impulse GPR system for practical use. In addition to the impulse system presented in this thesis, there are many more interesting factors to consider for such a system from the research point of view, such as the phase linearity of the antenna, changing the angle between the two antenna arms to obtain more intense electrical field and the corresponding antenna impedance changes, mutual coupling of the antennas, *etc*. These are left for future work.

References

[1] Scheers, B. *Ultra-Wideband Ground Penetrating Radar, with Application to the Detection of Anti Personnel Landmines*, Doctoral Thesis, Universite Catholique de Louvain Laboratoire D'Hyperfrequences Louvain-la-Neuve, Belgium, 2001.

[2] D. J. Daniels, "Ground Penetrating Radar", *Encyclopedia of RF and Microwave Engineering*, vol.2, John Wiley & Sons, Inc., Hoboken, New Jersey, United States, 2005, pp. 1833-1846.

[3] Corral Soto, Eduardo Rogelio, *Real-time Imaging System for a Ground Penetrating Radar,* Master Thesis, Dept. Electrical and Computer Engineering, University of Manitoba, Canada, 2003.

[4] *IEEE Standard Radar Definitions*, IEEE Std. 686-1990, p. 25, http://ieeexplore.ieee.org, last visited on Aug. 22, 2006.

[5] Soumekh, M., *Synthetic Aperture Radar Processing with MATLAB Algorithms,* John Wiley and Sons Inc., New York, United States, 2002.

[6] Phelan, M. C., *A Group Theoretical Symmetry Filter For Improved Subsurface Imaging,* Master Thesis, Dept. Electrical and Computer Engineering, University of Manitoba, Canada, 2003.

[7] Gilmore, C. G., *A Comparison of Imaging Methods Using GPR for Landmine Detection and A Preliminary Investigation into the SEM for Identification of Buried Objects*, Master Thesis, Dept. Electrical and Computer Engineering, University of Manitoba, Canada, 2004.

[8] Picosecond Pulse Labs, http://www.picosecond.com, last visited on August 22, 2006.

[9] Rhebergen, J. B., Zwamborn, A. P. M., Giri, D. V., "Design Of An Ultra-wideband Ground-penetrating Radar System Using Impulse Radiating Antennas", *Detection of Abandoned Land Mines, 1998. Second International Conference on the (IEE Conf. Publ. No. 458)*, Oct. 12-14 1998, pp. 45 - 49.

[10] Kolokotronis, D. A., Huang, Y**.,** and Bang, J. T. , **"**Design of TEM Horn Antennas for Impulse Radar", *1999 High Frequeucy Postgraduate Student Colloquium, 17* September *1999,* pp. 120-126.

[11] Montoya, T., Smith, G.. S., "Resistively-Loaded Vee Antennas for Short-Pulse Ground Penetrating Radar", *Antennas and Propagation Society International Symposium, AP-S. Digest,* vol.. 3, July 21-261996, pp. 2068 - 2071.

[12] T. P. Montoya and G. S. Smith, "Land mine detection using a ground penetrating radar based on resistively loaded vee dipoles," *IEEE Transactions on Antenna and Propagation*, vol. 47, Dec. 1999, pp. 1795-1806.

[13] Yarovoy, A.G., Sai, B., Hermans, G.., van Genderen, P., Ligthart, L.P., Schukin, A.D., Kaploun, I.V., "Ground Penetrating Impulse Radar for Detection of Small and Shallow-Buried Objects", *Proc. of IGARSS '99*, vol. 5, June/July, 1999, pp. 2468-2470.

[14] Turk, A. S., "Ultra-wideband TEM Horn Design for Ground Penetrating Impulse Radar Systems", *Microwave and Optical Technology Letters,* vol. 41, No. 5, June 5, 2004, pp. 333-336.

[15] Lestari, A. A., Yarovoy*, A. G.* and Ligthart*,*L. P., Adaptive Wire Bow-Tie Antenna for GPR Applications, *IEEE Transactions on Antenna and Propagation*, vol. 53, No. 5, May 2005, pp. 1745-1754.

[16] T. T.Wu and R.W. P. King, "The Cylindrical Antenna With Nonreflecting Resistive Loading", *IEEE Transactions on Antenna and Propagation*, vol. AP-13, May 1965, pp. 369–373.

[17] D.P. Nyquist, K. Chen, "The Traveling-Wave Linear Antenna with Nondisipative Loading", *IEEE Transactions on Antenna and Propagation*, vol. AP-16, no.1, Jan. 1968, pp. 21-31.

[18] B.L.J. Rao, J.E. Ferris, W.E. Zimmerman, "Broadband Characteristics of Cylindrical Antennas with Exponentially Tapered Capacitive Loading", *IEEE Transactions on Antenna and Propagation*, vol. AP-17, no.2, Mar. 1969, pp. 145-151.

[19] A.A. Lestari, A.B. Suksmono, E. Bharata, A.G. Yarovoy, L.P. Ligthart, "Small UWB antenna with improved efficiency for pulse radiation", *Proc. the 2005 IEEE International Workshop on Antenna Technology (IWAT2005)*, March 2005, Singapore, pp. 295-298.

[20] Thomas P. Montoya and Glenn S. Smith, "A Study of Pulse Radiation from Several Broad-Band Loaded Monopoles", *IEEE Transactions on Antennas And Propagation*, vol. 44, No. 8, August 1996, pp.1172-1182.

[21] Uduwawala, D.; Norgren, M.; Fuks, P.; Gunawardena, A.W.; A deep parametric study of resistor-loaded bow-tie antennas for ground-penetrating radar applications using FDTD, *IEEE Transactions on Geoscience and Remote Sensing,* vol. 42, Issue 4, April 2004, pp. 732-742.

[22] A. A. Lestari, A. G. Yarovoy and L P. Ligthart,"RC-loaded bow-tie antenna for improved pulse radiation", *IEEE Transactions on Antennas And Propagation*, vol. 52, No. 10, October 2004, pp.2555-2563.

[23] A. A. Lestari, A. G. Yarovoy and L P. Ligthart,"Capacitively-Tapered Bowtie Antenna", *Conference Proceedings on CD-ROM, Millennium Conference on Antennas & Propagation,* Davos, Switzerland, April 9-14 , 2000.

[24] Shlager, K.L.; Smith, G.S.; Maloney, J.G., "Optimization of bow-tie antennas for pulse radiation", *IEEE Transactions on Antennas And Propagation,* vol. 42, Issue 7, July 1994, pp. 975 - 982.

[25] Yasuhiro Nishioka,, Toru Uno and Takehito Iguch, "Characteristics of cavity-isolated and cavity-connected bow-tie antennas for subsurface pulse radar", *Electronics and Communications in Japan, Part 1,* vol. 85, No. 8, 2002; Translated from Denshi Joho Tsushin Gakkai Ronbunshi, vol. J83-B, No. 6, June 2000, pp. 910-917.

[26] Y. Nishioka, O. Maeshima, T. Uno, and S. Adachi, "FDTD analysis of resistor-loaded bow-tie antennas covered with ferrite-coated conducting cavity for subsurface radar," *IEEE Transactions on Antennas And Propagation*, vol. 47, June 1999, pp. 970-977.

[27] Liu, L.L.; Su, Y.; Huang, C.L.; Mao, J.J.; "Study about the radiation characteristics of bow-tie antennas with discrete resistor-loaded", *Microwave Conference Proceedings, 2005. APMC 2005. Asia-Pacific Conference Proceedings*, vol. 4, 4-7 Dec. 2005.

[28] Yarovoy, A.G.; Schukin, A.D.; Kaploun, I.V.; Ligthart, L.P.; "The dielectric wedge antenna", *IEEE Transactions on Antennas And Propagation*, vol. 50, Issue 10, Oct. 2002, pp. 1460-1472.

[29] A. A. Lestari, A. G. Yarovoy, and L. P. Ligthart, "Analysis of *RC* loading profiles for antenna bandwidth improvement," in *Proc. IEEE Antennas Propagat. Society Int. Symp. Digest*, vol. 3, Columbus, OH, Jun. 2003, pp. 632–635.

[30] Gupta, K.C., Garg, R., Bahl, I., Bhartia, P., *Microstrip Lines and Slotlines*, 2nd Edition, Artech House, Norwood, MA, 1996.

[31] Abdelnasser A. Eldek, Atef Z. Elsherbeni, and Charles E. Smith, "Wideband Microstrip-fed Printed Bow-tie Antenna For Phased Array Systems", *Microwave And Optical Technology Letters*, vol. 43, No. 2, October 20 2004, pp. 123-126.

[32] G. Bindu, V. Hamsakkutty, Anil Lonappan, Joe Jacob, Vinu Thomas, C. K. Aanandan, and K. T. Mathew, "Wideband Bow-tie Antenna With Coplanar Stripline Feed", *Microwave And Optical Technology Letters,* vol. 42, No. 3, August 5 2004, pp. 222-224.

[33] K. Tilley, X.-D. Wu and K. Chang, "Coplanar Waveguide Fed Coplanar Strip Dipole Antenna", *Electronics Letters*, February 3rd, 1994, vol. 30, No. 3.

[34] M.-Y. Li, K. Tilley, J. McCleary and K. Chang, "Broadband Coplanar Waveguide-Coplanar Strip-Fed Spiral Antenna", *Electronic Letters*, January 5th, 1995, vol. 31, no.1, pp. 4-5.

[35] Butrym, A.; Pivnenko, S.; "CPW to CPS Transition for Feeding UWB Antennas", *Aerospace and Electronic Systems Magazine, IEE,* vol. 21, Issue 2, Feb. 2006, pp. 21 - 23.

[36] Gupta, S.; Ramesh, M.; Kalghatgi, A.T.; "Design of Optimized CPW-fed Monopole Antenna for UWB Applications", *Microwave Conference Proceedings, 2005. APMC 2005. Asia-Pacific Conference Proceedings,* vol. 4, Dec. 4-7, 2005.

[37] Xian-Ling Liang; Shun-Shi Zhong; Feng-Wei Yao; "Compact UWB Tapered CPW-Fed Planar Monopole Antenna", *Microwave Conference Proceedings, 2005. APMC 2005. Asia-Pacific Conference Proceedings*, vol. 4, Dec. 4-7, 2005.

[38] Y. H. Suh, "Coplanar Stripline Components", pp. 780-82; L. Zhu, "Coplanar Waveguide", *Encyclopedia of RF and Microwave Engineering*, vol.1, John Wiley & Sons, Inc., Hoboken, New Jersey, United States, 2005, pp. 821-832.

[39] Abramowitz, M. and I.A. Stegun, *Handbook of Mathematical Functions*, Dover Publications, 1965, 17.6.

[40] D. N. Pozer, *Microwave Engineering*, Second edition, John Wiley and Sons, New York, United States, 1998.

[41] J. Thaysen, K. B. Jakobsen and J. Appel-Hansen, "A Wideband Balun - How Does it Work", *Applied Microwave & Wireless*, vol 12, 2000, pp 40-50.

[42] Thaysen, J.; Jakobsen, K.B.; Appel-Hansen, J.; "Characterisation and Optimisation of A Coplanar Waveguide Fed Logarithmic Spiral Antenna", *Antennas and Propagation for Wireless Communications, 2000 IEEE-APS Conference on*, Nov.6-8 , 2000, pp. 25 - 28.

[43] Thaysen, J.; Jakobsen, K.B.; Lenler-Eriksen, H.-R.; " Wideband Cavity Backed Spiral Antenna For Stepped Frequency Ground Penetrating Radar", *Antennas and Propagation Society International Symposium, 2005 IEEE*, vol. 1B, July 3-8, 2005, pp. 418 - 421.

[44] P. Benedek and P. Silvester, "Equivalent capacitances for microstrip gaps and steps," *IEEE Trans. Microwave Theory Tech.*, vol. MTT-20, Nov. 1972, pp. 729–733.

[45] M.A. Al-Alaoui, "Novel IIR Differentiator From The Simpson Rule", *IEEE Trans Circ Sys I* 41 (1994), pp. 186–187.

[46] C.-C. Tseng, "Design of Fractional Order Digital FIR Differentiators", *IEEE Signal Processing Lett* 8 (2001), pp. 77–79.

[47] B. Kumar and S.C. Dutta-Roy, "Design of Digital Differentiators For Low-frequencies", *Proc. IEEE* 76 (1988), pp. 287–289.

[48] S.C. Pei and J.J. Shyu, "Analytic Closed Form Matrix For Designing High Order Digital Differentiators Using Eigenapproach", *IEEE Trans Signal Processing* 44 (1996), pp. 698–701.

[49] Ching-Wen Hsue, Ming-Chih Kuan, and Chia-Mei Peng, "A Microwave Differentiator**",** *Microwave And Optical Technology Letters,* vol. 37, No. 3, May 5 2003, pp. 226-228.

[50] T. Edward, *Foundations for microstrip circuit design*, Chapter 3, Wiley Inc., New York,1991.

[51] Digi-key Corporation, http://www.digikey.com, last visited on August 22, 2006.

[52] C. A. Balanis, *Antenna Theory*, Second Edition, John Wiley and Sons Inc., New York, United States, 1997.

[53] A. A.Lestari, A. B, A. G. Yerovoy, L. P. Ligthart, "An Efficient Ultra-Wideband Bow-tie Antenna", *Proc. of the 31st European Microwave Conference*, London, UK, Sept. 25-27, 2001.

[54] A. A.Lestari, A. B, A. G. Yerovoy, L. P. Ligthart, "Improvement of Bow-tie Antennas for Pulse Radiation", *Proc. AP-S 2002, IEEE Antennas and Propagation Soc. Int. Symp.,* San Antonio, Texas, USA, June 16- 21, 2002, vol. 4, pp. 566-569.

[55] Arlon Materials for Electronics (MED), http://arlon-med.com/AD%20Series.pdf, last visited on August 22, 2006.

[56] J. G. Maloney and G. S. Smith, "A study of transient radiation from the Wu–King resistive monopole—FDTD analysis and experimental measurements", *IEEE Transactions on Antennas And Propagation*, vol. 41, May 1993, pp. 668–676.

[57] Cumming Corporation, http://www.cumingcorp.com, last visited on August 22, 2006.

[58] T. P. Montoya and G. S. Smith, "A study of pulse radiation from several broad-band loaded monopoles," *IEEE Transactions on Antennas And Propagation*, vol.44, Aug. 1996, pp. 1172–1182.

[59] M. Phelan, H. Su, J. LoVetri, "Near Field Analysis of a Wideband Logspiral Antenna for 1-2 GHz GPR", *Proceedings of the 2002 IEEE Canadian Conference on Electrical & Computer Engineering*., pp. 336-341.

[60] A. A.Lestari, A. B. Suksmono, A. Kurniawan, E. Bharata, A. G. Yerovoy, L. P. Ligthart, " A Facility for UWB Antenna Measurements in Time Domain", *Proceedings of the 2005 IEEE International Workshop on Antenna Technology (IWAT2005)*, Singapore, March 2005, pp. 109-112.

[61] A. Yarovoy, R. de Jongh and L. Ligthart, "Ultra-wideband Sensor For Electromagnetic Field Measurements in Time Domain**",** *Electronics Letters,* September 28th, 2000 Vol**.** 36 No. 20, pp. 1679-1680.

[62] H.-M. Shen, R. W. P. King, T. T. Wu, "New Sensor for Measuring Very Short Electromagnetic Pulses", *IEEE Transactions on Antennas And Propagation*, vol. 38, No. 6, June 1990, pp. 838-846.

[63] M. Kanda, "Time-domain Sensors For Radiated Impulsive Measurements", *IEEE Transactions on Antennas And Propagation*, vol. 31, Issue 3, May 1983, pp. 438 - 444.